Davies, P. J., McKenzie, J. A., Palmer-Julson, A., et al., 1991
Proceedings of the Ocean Drilling Program, Initial Reports, Vol. 133

12. SITE 819[1]

Shipboard Scientific Party[2]

HOLE 819A

Date occupied: 9 September 1990

Date departed: 12 September 1990

Time on hole: 2 days, 5 hr, 26 min

Position: 16°37.439′S, 146°19.486′E

Bottom felt (rig floor; m, drill-pipe measurement): 576.4

Distance between rig floor and sea level (m): 11.29

Water depth (drill-pipe measurement from sea level, m): 565.2

Total depth (rig floor; m): 976.5

Penetration (m): 400.0

Number of cores (including cores with no recovery): 44

Total length of cored section (m): 400.0

Total core recovered (m): 339.5

Core recovery (%): 84.9

Oldest sediment recovered:
Depth (mbsf): 400.0
Nature: bioclastic clayey chalk
Age: Pleistocene

Principal results: Site 819 is located in 565.2 m of water in Grafton Passage, on the continental slope east of Cairns. The location represents the distal and deeper-water end of a shelf-edge transect that was aimed at defining the relationships among changes in sea level, sedimentary sequences, and seismic geometries, and in particular, the response of a developing slope sequence to rapid changes in global sea level. While APC/XCB coring to 400 mbsf, we recovered 84.9% of the cored interval, which indicated an expanded Pleistocene section spanning <1.48 m.y. Preservation of nannofossils was excellent, although preservation of planktonic foraminifers is facies-specific, with light-colored intervals that contain abundant foraminifers present. Whereas benthic foraminifers indicate an upper bathyal water depth for the entire Site 819 section consistent with the present water depth at the site, sediment studies suggest substantial variations in depth, as controlled by changes in sea level and fluvial influxes. A hiatus occurs between 275 and 465 k.y. Sedimentation rates vary in relation to lithologic changes, were modest (10–11 cm/k.y.) in the late Pleistocene, were even more modest (6 cm/k.y.) from 0.93 to 0.465 k.y., and were high (42.4 cm/k.y.) during the middle Pleistocene (1.27–0.93 Ma). Between 1.27 Ma and the base of Hole 819A (<1.48 Ma), an extremely rapid sedimentation rate of about 87 cm/k.y. occurred. Calculation of sedimentation rates and definition of major sedimentary units are complicated by the recognition of slumping within the drilled section at two levels, 32.5 and 75 mbsf, and by a slump detachment surface at about 190 mbsf, observed in seismic data.

Five major sedimentary units have been identified in the section as follows:

1. *Unit I:* depth, 0–32.5 mbsf; age, late Pleistocene. Rhythmically interbedded couplets of dark green clay-rich and green gray carbonate-rich clayey pteropod ooze. The unit shows highly variable, but upward-increasing carbonate percentages (24.9%–75.3%), while aragonite dominates as the principal carbonate mineral; within each couplet, calcium carbonate increases upward. The base of the three youngest couplets is composed of pteropod-rich, bioclastic debris. The estimated duration of each couplet is 104,000 yr. A possible slump surface at a depth of 32.5 mbsf separates Unit I from Unit II.

2. *Unit II:* depth, 32.5–97.0 mbsf; age, middle to late Pleistocene. The unit comprises five rhythmic couplets made up of silty stringers toward its base that grade upward into dolomitized clayey nannofossil oozes. Carbonate varies up the unit from 19.1% to 76.2% and is dominated by aragonite, which forms between 15% and 45% of the carbonate minerals; dolomite forms up to 15% of the minerals. These couplets average 13 m thick and, using a sedimentation rate of 4.8 cm/k.y., their accumulation time was estimated as 183,000 yr each. This assumes that different parts of the couplet were deposited at the same rate, which may not have been the case.

3. *Unit III:* depth, 97.0–179.7 mbsf; age, Pleistocene. The unit consists of rhythmically interbedded bioclastic and micritic oozes. Carbonate generally decreases upward with corresponding increasing siliciclastics. Seven poorly defined, upward-coarsening rhythmic couplets were identified; these are composed of a sharp-based dark green gray clay-rich, quartz-rich lower half and an upper half of lighter green carbonate and bioclastic-rich clayey ooze to chalk. Major slumping has disturbed the base of the unit. The duration of the cycles within the unit cannot be estimated until we establish better age control. An unrecovered interval between Units III and IV occurs from 179.7 to 198.1 mbsf.

4. *Unit IV:* depth, 198.1–313.2 mbsf; age, early Pleistocene. Unit IV consists of interbedded bioclastic wackestones and nannofossil clayey oozes with quartz and silt stringers. Carbonate contents are generally low, with the sediments reflecting an origin related to mixed terrigenous/neritic to upper bathyal. Although higher percentages of quartz silt and sand characterize the unit as a whole, they are best seen near the base, where three upward-coarsening packages occur.

5. *Unit V:* depth, 313.2–400 mbsf; age, early Pleistocene. The unit is composed of a relatively homogeneous sequence of dark green gray bioclastic clayey chalk at its base, micritic clayey chalks in the middle, and clayey bioclastic nannofossil chalks in the uppermost part of the section. Carbonate contents are uniform and quartz is most dominant in the middle micritic part of the section.

Mineralogy of the Pleistocene sediments is dominated by clays (kaolinite and illite) and carbonates that vary from 10% to 90%. Aragonite occurs throughout the site as the principal carbonate mineral. Dolomite is present, but varies; a correspondence of dolomite distribution with alkalinity variation suggests that this dolomite may be authigenic, while the source of the magnesium is dissolution of high-Mg calcite and ambient pore fluids.

Interstitial water chemistry reflects diagenetic reactions, while the loss of calcium and magnesium is tied to precipitation of calcite and dolomite and the alteration of clay minerals. Increases in strontium reflect dissolution of aragonite and high-Mg calcite and precipitation of calcite and dolomite, whereas decreases may reflect clay mineral diagenesis. Variations in alkalinity track the removal of sulfate and the precipitation of carbonates, whereas we think that the considerable variations in chlorinity reflect changes in the chlorinity of seawater during glacial and interglacial periods.

[1] Davies, P. J., McKenzie, J. A., Palmer-Julson, A., et al., 1991. *Proc. ODP, Init. Repts.*, 133: College Station, TX (Ocean Drilling Program).

[2] Shipboard Scientific Party is as given in list of participants preceding the contents.

Organic carbon content of these sediments varies from 0.2% to 0.65% and is essentially of marine origin. High concentrations of methane occur, of principally biogenic origin; the C_1/C_2 ratio in headspace samples ranges from 10,000 to 2,000. Below 225 mbsf, mixing of biogenic and thermogenic gases is suggested by the analyses.

Downhole measurements at Site 819 show the control of variations in clay mineral on velocity, resistivity, density, and gamma-ray logs. All the logs are semiquantitative indicators of clay minerals. Excellent correlation exists between logging and drilling characters.

Shipboard paleomagnetic studies revealed a complicated paleomagnetic story that may be resolvable only with further detailed shore-based studies. Two possible alternative explanations are favored now. First, four normal polarity magnetozones were tentatively identified as Brunhes, Jaramillo, Cobb Mt., and, more speculatively, Olduvai; short normal polarity units between the Cobb and Olduvai(?) zones have been interpreted as excursions. Nannofossil ages and paleomagnetic interpretations do not agree totally and will need to be resolved with detailed shore-based studies. Second, in accord with paleontological data, extremely rapid sedimentation rates and faulting within the section may have extended the length of the Brunhes zone and repeated parts of the higher section. Shore-based studies should resolve these problems.

BACKGROUND AND SCIENTIFIC OBJECTIVES

The Queensland Trough transect (Sites 819 to 824; see Fig. 1, "Introduction" chapter, this volume) includes the slope of the Great Barrier Reef, the basin infill in the Queensland Trough, and the slope along the western margin of the Queensland Plateau. Therefore, in addition to specific objectives defined for each site or sets of sites, this transect was intended to help define the interaction and development of the basin and its adjacent platforms, focusing on slope and basin-infill processes. Furthermore, the basin sequences were thought to preserve a record of the corresponding oceanographic changes.

In the following section, we review the background and overall scientific objectives of drilling the upper slope of the Great Barrier Reef.

The Upper Slope of the Great Barrier Reef (Sites 819, 820, and 821)

The continental shelf off northeastern Australia is dominated by the Great Barrier Reef, one of the world's largest areas of carbonate deposition (see Fig. 1, "Introduction" chapter, this volume). These reefs form part of a modern carbonate-dominated passive margin that extends some 2000 km. Davies et al. (1987, 1989) showed that the reef was diachronous in its development (i.e., Miocene in the north and Pliocene–Pleistocene in the south; Fig. 1). In the central region between Cairns and Townsville, previous studies proposed that the reefs are only 250 to 300 m thick and are made up of a series of high-sea-level growth slices separated by unconformities that were generated during lowstands of sea level (Davies, 1983; Davies et al., 1987, 1989; Symonds et al., 1983). Thus, we expected the Great Barrier Reef to be of Pliocene–Pleistocene age. For this same area, scientists had also previously proposed that the reefs formed only a part of a much thicker, outer-shelf sequence, dominated by fluvioclastic and deltaic sediments. In this central region, therefore, a testable hypothesis was postulated: that the reef-carbonate scenario forms only part of the picture and that an equally important part has to do with clastic sedimentary processes. It follows from this that the relative importance of carbonates and clastics during the evolution of the continental shelf off northeastern Australia should relate to the history of sea level in the region.

During the last 10 year, studies of late Pleistocene sediments of the shelf of the Great Barrier Reef region have tried to relate facies to different sea-level scenarios. A series of facies have been identified that developed in response to a transgression and a stillstand, and that may be used to understand the stratigraphy of the shelf and slope. Reef, inter-reef, and coastal facies, all have been studied separately.

Reef facies reflect the high physical energy within the system, the oceanography of the transgression, and the particular transgressive/stillstand history of the Queensland margin (Marshall and Davies, 1982, 1984; Davies, 1983; Davies and Hopley, 1983; Davies et al., 1985). Holocene high-sea-level reefs have been shown to occupy the same position as their Pleistocene precursors, i.e., reefal sediments do not mantle the whole of the shelf as a consequence of high growth of sea levels, but rather, occur in discrete areas. High physical energy ensures that reef-derived sediments are transported leeward, while little is deposited in front of the reefs as fore-reef aprons. Leeside reef-sediment tails occur to a distance of 2 to 3 nmi from the reefs.

Inter-reef, high-sea-level carbonate sedimentation is limited to the mid and outer shelf and is represented by aggradational carbonate biostromes (Davies et al., 1989) and bioherms (Davies et al., 1985) above a transgressive, usually siliciclastic blanket. The inter-reef sedimentary blanket thus forms a couplet composed of a transgressive terrigenous lower part and an upper part dominated by stillstand carbonates, which form the thickest part of the section. This blanket has an average thickness of 10 to 15 m over the middle and outer shelf and was deposited in the last 10,000 year.

High-sea-level terrigenous sedimentation has been restricted to the coastal zone and inner shelf, and then only to a depth of <20 m. Most sedimentation is held in the coastal traps and presently is not getting out onto the shelf. Prodeltaic muds and muddy sands are being deposited in association with coastal deltas. Infrequent cyclones and extremely heavy cyclonic rainfall in summer months occasionally transports large volumes of terrigenous clastics to the shelf, some of which are known to reach the outer reefs (Davies et al., 1985). Some of this may even reach the upper slope during periods of high sea level.

Information about shelf sedimentation in the Great Barrier Reef region during periods of low sea level has been obtained from boomer profiles and vibrocores. Boomer profiles of the mid to outer shelf show significant fluviatile channeling, multigenerational infill, levee bank deposits, and complex progradational channel fill and deltaic sedimentation, all features of subaerial sedimentation. Thus, down to boomer penetration depths of 40 ms, the shelf is underlain by terrigenous facies that are related to fluvial and deltaic processes, clearly related to periods of low sea level. The characteristics of the section below 40 ms were revealed by sparker and water-gun profiles conducted by BMR throughout the 1980s. These data show that the history of the Pliocene and Pleistocene of the Great Barrier Reef has been dominated by low-sea-level fluvial and deltaic sedimentation. Data also suggest that the Great Barrier Reef itself grew upon prograding fluvioclastic sequences and must be a young feature in this central region.

Clearly, these carbonate and fluvioclastic sediments were deposited during different states of sea level and thus may be diagnostic of changes in sea level. Sites 819, 820, and 821 are located on the upper slope of the shelf, to the east of Grafton Passage (Fig. 1, "Introduction" chapter, this volume; Fig. 2). Shelf-edge reefs occur only 2 km west of Site 821. The seismic cross section through all three sites shown in Figure 3 defines an upper, essentially aggrading, section that overlies a lower

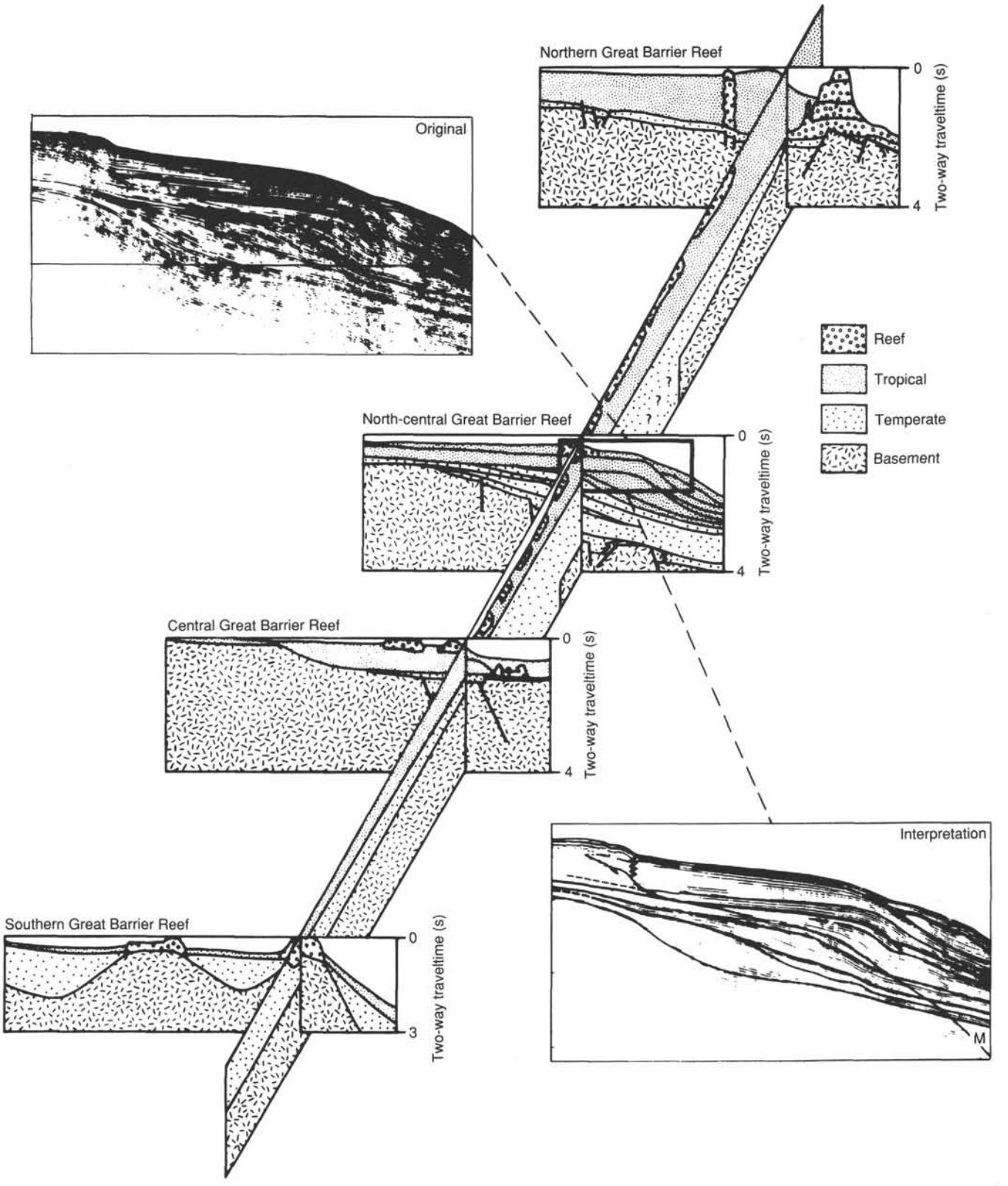

Figure 1. Schematic north-to-south section illustrating variations in thickness of temperate and tropical facies of the Great Barrier Reef shelf and slope. The northward-thickening tropical wedge implies that reef growth began earlier in the north than in the south (from Davies et al., 1987).

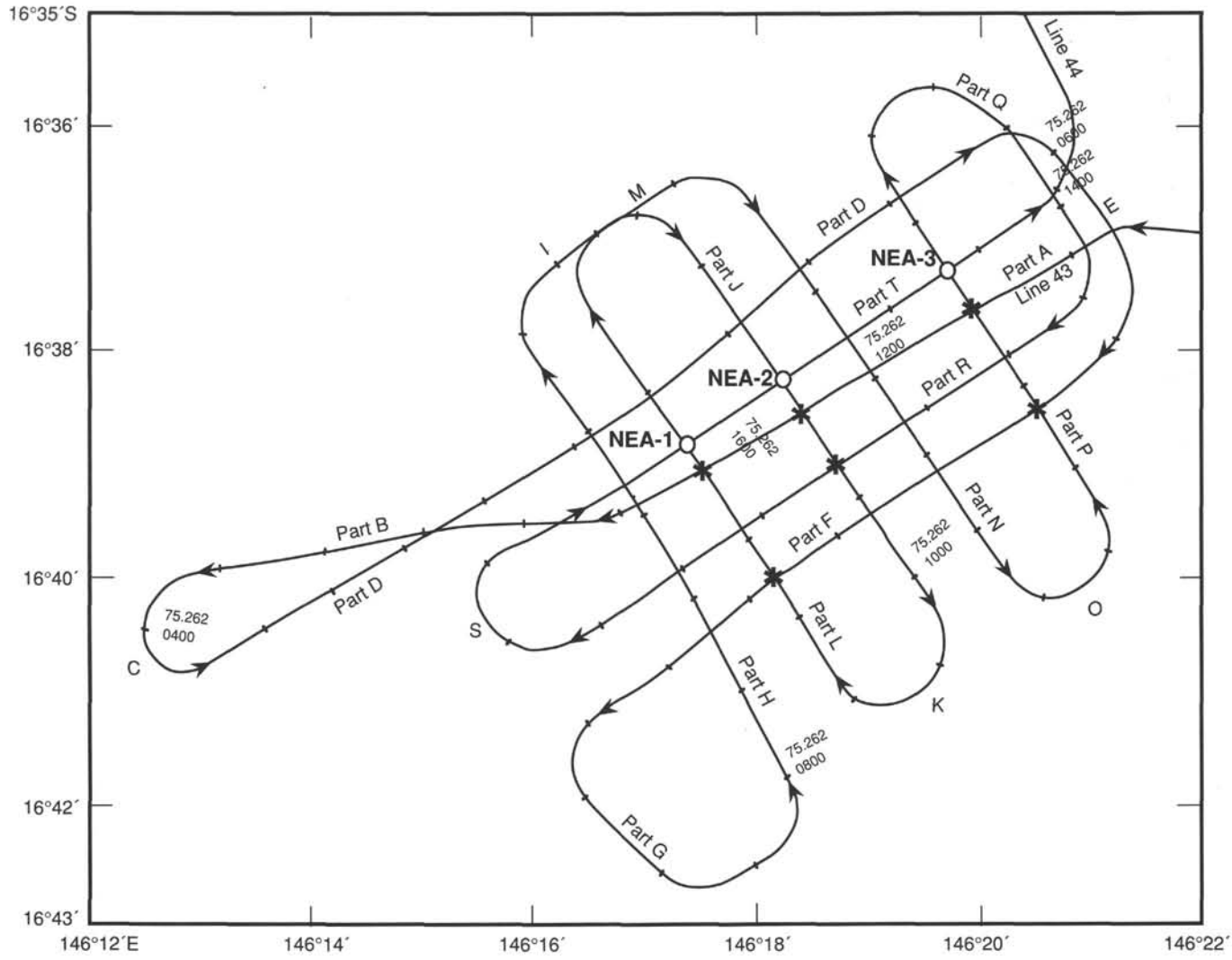

Figure 2. Track map of site survey data for proposed Sites NEA-1 through NEA-3 (Sites 821–819).

series of progrades. Prior to drilling, the age of the whole sequence was thought to be late Pliocene to Pleistocene. This section shows most of the seismic geometries described by Vail and co-workers as indicative of sequential changes in eustatic sea level. Thus, these three holes provide a high-resolution test of the relationships among seismic facies, sedimentary facies, and rapid changes in sea level. Specific objectives of Sites 820 and 821 are discussed in the respective site chapters.

Objectives at Site 819

Site 819 is located on the upper slope of the Great Barrier Reef (and in the most distal position with respect to the GBR) of the three sites drilled in Grafton Passage. A track map of the site-survey data is presented in Figure 2, the seismic dip line through the site in Figure 3, and the pre-drilling prognosis for the site in Figure 4. Objectives at this site were as follows:

1. To determine the age and facies of the most distal portions of the progradational units in front of the Great Barrier Reef.
2. To determine the relationship between sea level and depositional facies to extract the sea-level signature.
3. To determine the timing and factors controlling the initiation of reef growth on the central Great Barrier Reef.
4. To determine the nature of the deeper-water condensed section equivalent to the aggrading package deposited nearer shore.

OPERATIONS

Transit to Site 819

Transit to Site 819 (proposed Site NEA-3) began at 0300L (all times given in local time, or L) 9 September and covered 229 nmi in 18.9 hr at an average speed of 12.1 kt. A seismic survey was run over Sites 819, 820, and 821 (proposed Sites NEA-1, -2, and -3) that covered 19 nmi in 3.35 hr at an average speed of 5.7 kt. A Benthos beacon was run on a taut wire at 0124L, 10 September. To avoid the beacon problems experienced at Site 818, a spare wireline spool stand was built to hold the beacon upright and to give it added stability.

Hole 819A

The hole was located at 16°37.439′S, 146°19.486′E. The precision depth recorder (PDR) showed a water depth of 561.6 m from sea level for this location. However, the first shot attempted at Site 819 yielded a water core, indicating that the actual mud line occurred between the upper two of the three bottom reflectors visible on the 3.5- and 12-kHz profiles (see "Site Geophysics" section, this chapter). The bit was posi-

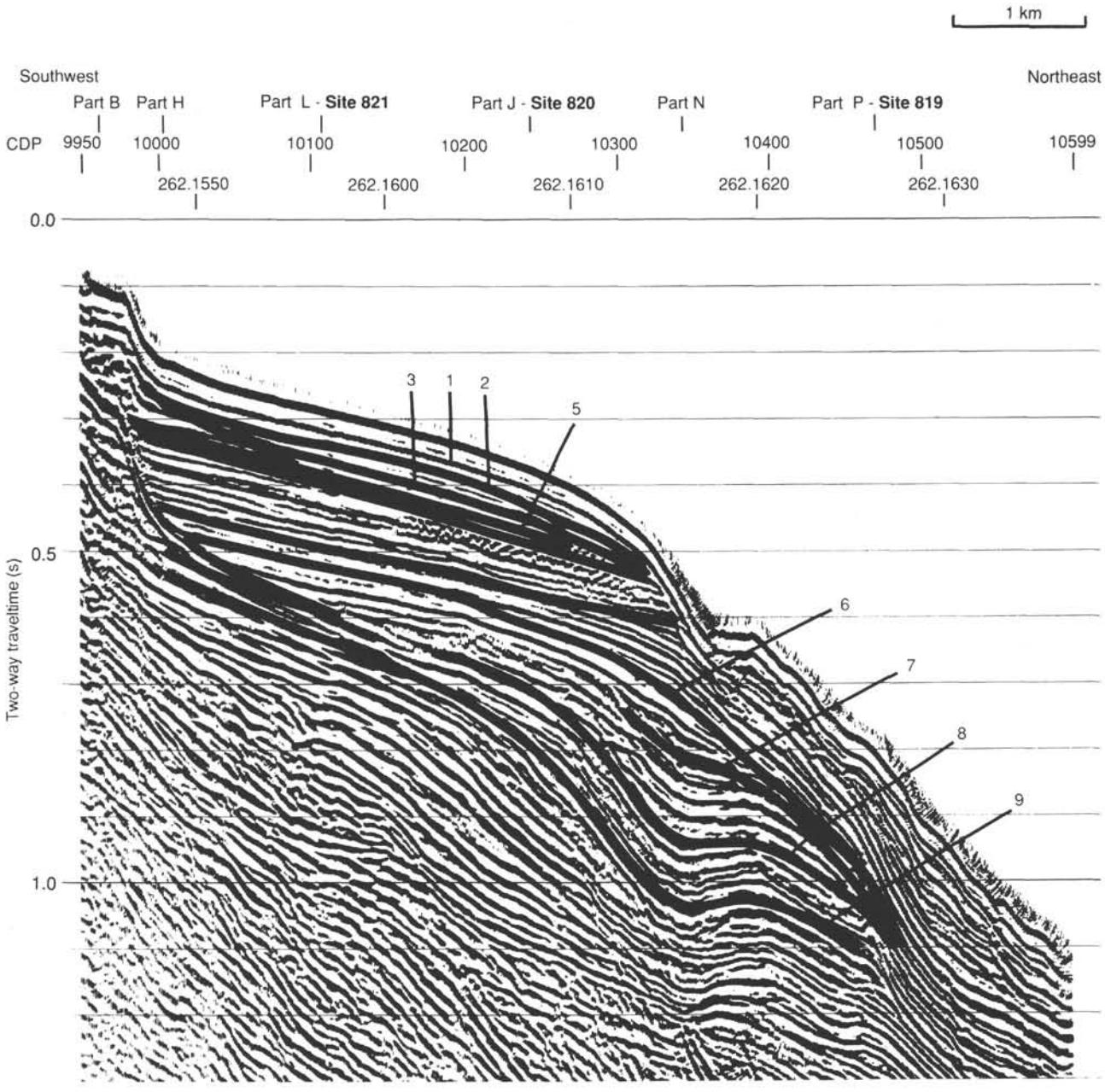

Figure 3. Seismic data through Sites 819, 820, and 821.

tioned at a water depth of 564.2 m from sea level, and the hole was spudded at 0435L, 10 September 1990. A total of 8.55 m of sediment was recovered, placing the mud line at a water depth of 565.2 m from sea level. Continuous APC cores (Cores 133-819A-1H through -14H were taken from 0 to 123.0 mbsf), with 123.0 m cored and 133.5 m recovered for a recovery of 108.6%. The excessively high rate of recovery is a result of gas expansion in the sediment.

Operations were slowed after problems with the APC core barrel and liners that were apparently caused by the high gas contents of the sediments. Headspace analysis indicated that gas concentrations were an average 10,000 ppm C_1, 4 ppm C_2, and 4 ppm C_3. The C_1/C_2 ratio indicated no safety problem because hydrocarbons evidently were generated *in situ* and had not migrated into the sediment.

Cores 133-819A-15X through -44X (123.0–400.0 mbsf) were taken, with 277.0 m cored and 205.5 m recovered (74.3% recovery). The age of the sediments was consistently 1.5 Ma throughout this interval, leading us to consider the possibility that the hole had been deflected along a steeply dipping hard layer. Multishot orientation surveys were conducted at 50-m intervals while Core 133-819A-44X was retrieved. These demonstrated that the hole was essentially vertical, with a maximum angle of deviation of 3.2° at 380 mbsf. The global positioning system (GPS) window for the next site did not give us time to run a conditioning trip for logging. Therefore, a 30-bbl-mud sweep was circulated, a go-devil was dropped to open the lockable flapper valve, and the bit was pulled to 98.6 mbsf for logging.

The only logging tool string run at Site 819 was the induction/density/sonic/caliper/gamma-ray (DITE/HLDT/SDT/

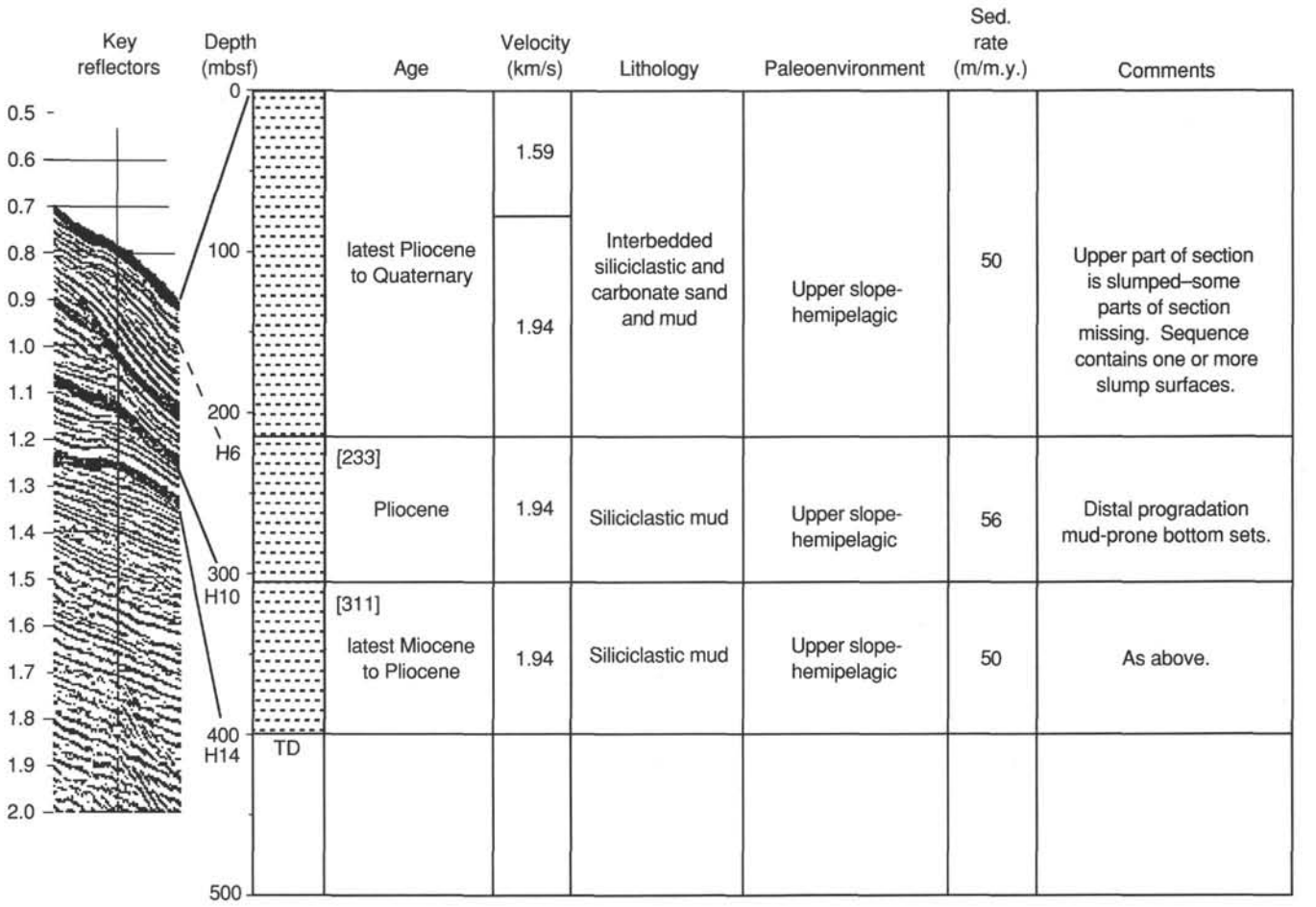

Figure 4. Pre-drilling prognosis for Site 819.

MCDG/NGT) string. The logging tool was placed into the hole at 0205L, 7 September, and found bottom about 17 m above total depth. The tool was back on deck at 0440L, 12 September.

The BHA was run into the hole at 384.8 mbsf, and the hole was filled with heavy mud, according to JOIDES Pollution Prevention and Safety Panel guidelines. The BHA was pulled out of the hole and cleared the seafloor at 0650L, 12 September. The beacon was pulled up to a water depth of 244 m on a taut wire for a short transit to the next site. The ship was under way in dynamic positioning mode at 0718L, 12 September, with optimal GPS positioning.

Table 1 contains the coring summary for Site 819.

SITE GEOPHYSICS

JOIDES Resolution separated from the beacon at Hole 818B at 0134L (JD 251/1534UTC), 9 September 1990 and began the 19-hr transit to Sites 819, 820, and 821 (proposed Sites NEA-3, NEA-2, and NEA-1, respectively) at 0900L (JD 238/2300UTC). A magnetometer was towed immediately after our departure, and continuous bathymetric and magnetic data were recorded during the Line 6 transit, while heading about 300° across southeastern Queensland Plateau and Queensland Trough toward the Australian coastal town of Cairns. The ship arrived at a position of 16°35.400′S and 146°22.673′E, about 3.6 nmi northeast of Site 819, at 2154L (JD 252/1154UTC), ready to start a site-location survey.

Sites 819, 820, and 821 lie in 206 to 565 m of water on the upper continental slope adjacent to the Great Barrier Reef, just east of the entrance to Grafton Passage, a shipping passage through the reef east of Cairns (Fig. 5). Sites 819, 820, and 821 lie about 11, 8, and 6 km, respectively, from the nearest reef (Euston Reef). These sites form the western end of a drilling transect that extends east from the Great Barrier Reef, across Queensland Trough to western Queensland Plateau, in the vicinity of Holmes Reef. The sites were selected to examine a mixed siliciclastic/carbonate shelf-margin depositional system that has largely been controlled by fluctuations in sea level. The system is represented by progradational packages, most of which were deposited before reef growth, and an upper aggradational package. Prior to drilling, we thought that these packages were of latest Miocene–Pleistocene age. Sites 819, 820, and 821 are situated in distal (bottom-set), intermediate (fore-set) and proximal (top-set) positions within this depositional system.

The area was first recognized as a potential ODP drilling target during a 1982 BMR sparker line through Grafton Passage (Line 41/063; Fig. 7, "Site 815" chapter, this volume), and more sparker seismic lines were recorded along the slope in this area by BMR in 1985 (Lines 50/014 and 50/015). In 1987, the BMR vessel *Rig Seismic* was used to conduct a site survey at this location (Symonds and Davies, 1988; Feary et al., 1990) and about 131 km of 24-channel, 80-in.^{3} water-gun, magnetic, and bathymetric data were collected on a grid of northeast-southwest and northwest-southeast lines (Figs. 7 and 8, "Site 815" chapter, this volume). All three sites lie on strike-line intersections with the only dip line (Line 75/043, Part A) within this grid, and they were located using the GPS.

Table 1. Coring summary, Site 819

Core no.	Date (Sept. 1990)	Time (UTC)	Depth (mbsf)	Length cored (m)	Length recovered (m)	Recovery (%)
Hole 819A						
1H	9	1840	0.0–8.5	8.5	8.55	100.0
2H	9	1850	8.5–18.0	9.5	9.78	103.0
3H	9	1905	18.0–27.5	9.5	9.56	100.0
4H	9	1935	27.5–37.0	9.5	9.92	104.0
5H	9	2000	37.0–46.5	9.5	10.12	106.5
6H	9	2025	46.5–56.0	9.5	9.17	96.5
7H	9	2050	56.0–65.5	9.5	10.13	106.6
8H	9	2110	65.5–75.0	9.5	10.83	114.0
9H	9	2135	75.0–84.5	9.5	10.56	111.1
10H	9	2150	84.5–94.0	9.5	10.53	110.8
11H	9	2215	94.0–103.5	9.5	10.55	111.0
12H	9	2240	103.5–111.0	7.5	7.52	100.0
13H	9	2310	111.0–120.5	9.5	11.03	116.1
14H	9	2335	120.5–123.0	2.5	5.77	231.0
15X	10	0035	123.0–130.4	7.4	7.11	96.1
16X	10	0200	130.4–140.1	9.7	10.75	110.8
17X	10	0315	140.1–149.7	9.6	2.44	25.4
18X	10	0435	149.7–159.4	9.7	6.83	70.4
19X	10	0540	159.4–169.1	9.7	4.46	46.0
20X	10	0635	169.1–178.8	9.7	9.62	99.2
21X	10	0730	178.8–188.4	9.6	0.11	1.1
22X	10	0830	188.4–198.1	9.7	0.00	0.0
23X	10	0930	198.1–207.4	9.3	9.20	98.9
24X	10	1035	207.4–217.0	9.6	8.19	85.3
25X	10	1215	217.0–221.7	4.7	3.97	84.4
26X	10	1335	221.7–226.3	4.6	2.69	58.5
27X	10	1430	226.3–236.0	9.7	6.12	63.1
28X	10	1535	236.0–245.6	9.6	2.57	26.8
29X	10	1650	245.6–255.3	9.7	6.16	63.5
30X	10	1840	255.3–264.9	9.6	3.18	33.1
31X	10	1910	264.9–274.5	9.6	4.17	43.4
32X	10	2010	274.5–284.2	9.7	7.17	73.9
33X	10	2130	284.2–293.9	9.7	4.80	49.5
34X	10	2255	293.9–303.5	9.6	5.06	52.7
35X	10	2355	303.5–313.2	9.7	9.78	101.0
36X	11	0115	313.2–322.9	9.7	10.11	104.2
37X	11	0240	322.9–332.5	9.6	9.70	101.0
38X	11	0355	332.5–342.2	9.7	10.27	105.9
39X	11	0525	342.2–351.5	9.3	10.16	109.2
40X	11	0655	351.5–361.1	9.6	10.02	104.4
41X	11	0820	361.1–370.8	9.7	10.56	108.8
42X	11	0940	370.8–380.4	9.6	10.02	104.4
43X	11	1100	380.4–390.0	9.6	10.24	106.6
44X	11	1250	390.0–400.0	10.0	10.04	100.4
		Coring totals		400.0	339.52	84.9

Note that times are given in Universal Time Coordinated or UTC, which is 10 hr later than local time or L.

An important requirement of Leg 133 site-location surveys was that seismic records obtained on board the *JOIDES Resolution* be as near as possible in appearance to those collected during the 1987 site surveys conducted from the *Rig Seismic*, thus reducing ambiguity when defining sites and when comparing seismic stratigraphy of the two data sets. Accordingly, some modifications were made to the *JOIDES Resolution* seismic deployment systems.

Because Sites 819, 820, and 821 lie within the same site-survey grid and are all less than 8 km apart, site-location surveys were conducted at the same time (Fig. 6). These surveys were designed (1) to confirm proposed positions in *JOIDES Resolution* seismic data that had been collected along the *Rig Seismic* track connecting the sites and (2) to obtain a parallel seismic line on the northern edge of the site-survey grid for better definition of the site area. Following the survey, the sites were to be relocated using confirmed GPS coordinates and a beacon dropped while maneuvering onto the location using the *Resolution's* GPD. We expected that this method would allow us to position the vessel's moonpool accurately over the sites. Accurate site positioning was particularly important in the case of Site 819 because it lies less than 200 m west of a major erosional or slump scarp (Fig. 7). Should drilling take place east of this scarp, we felt that the age and nature of the sediments intersected would be different from that anticipated and that site objectives would not be fulfilled. As recommended by the JOIDES Pollution Prevention and Safety Panel (PPSP), we decided to drill the three sites in the order from deepest to shallowest water depth (i.e., proposed Sites NEA-3 to NEA-1).

Distribution of regional seismic data in the area around these sites is shown in Figure 7, "Site 815" chapter (this volume), and tracks of the original *Rig Seismic* site survey and the *JOIDES Resolution* site-location survey are shown in Figure 8, "Site 815" chapter (this volume). Following a reduction in the ship's speed to 5 kt, the *JOIDES Resolution*'s single-channel seismic profiling system was deployed, and seismic recording commenced at JD 252/1210UTC, 9 September 1990, in rough seas (Beaufort Scale force 4–5) having swells of 2 to 3 m. The *JOIDES Resolution* initially sailed

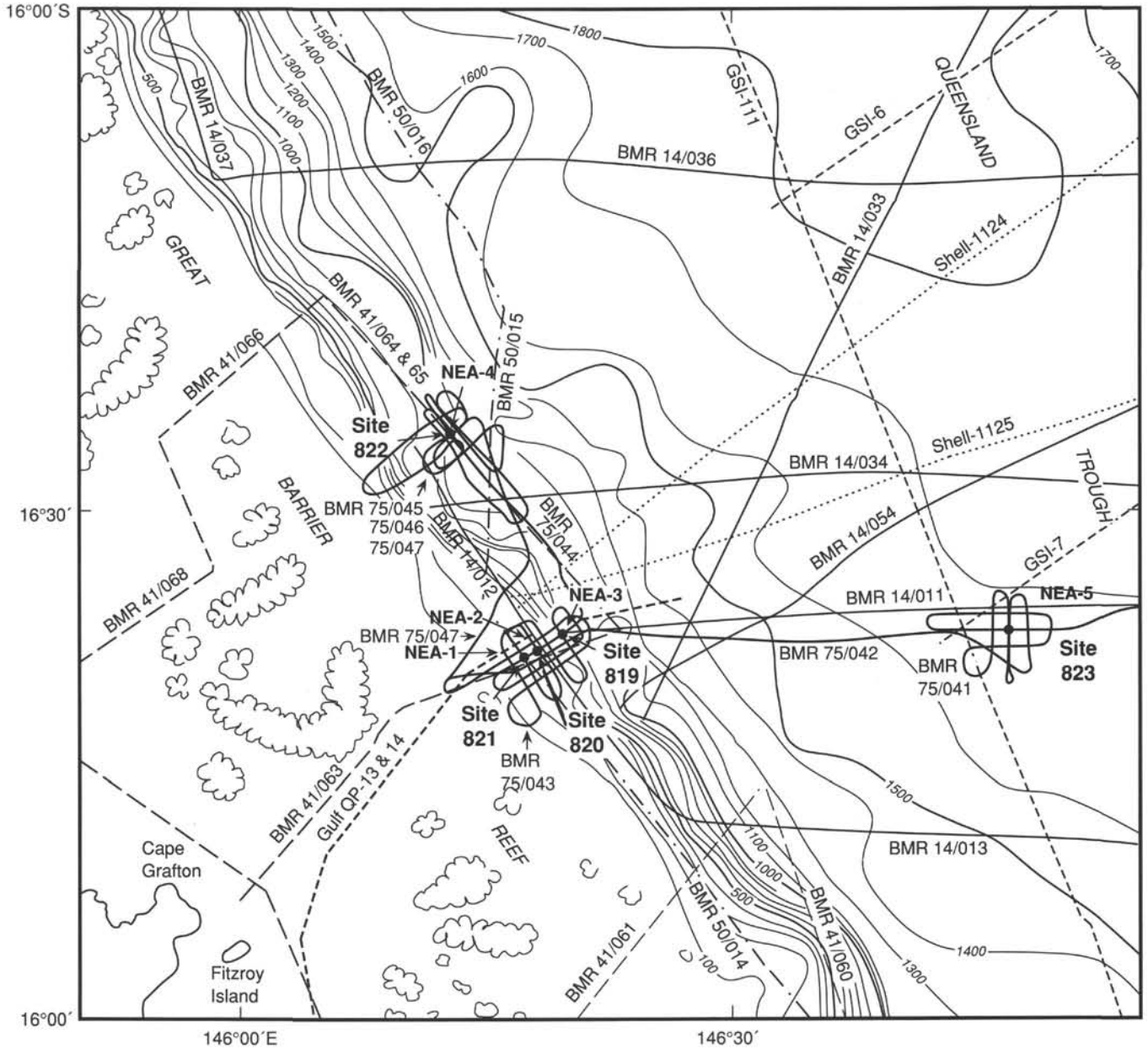

Figure 5. Track chart showing distribution of regional seismic data in the area around Sites 819, 820, and 821. Also shows locations of Sites 822 and 823 and simplified bathymetry of region in meters.

southwest (heading about 240°) across Sites 819, 820, and 821 to confirm their GPS positions, then turned northwest, parallel to the Great Barrier Reef, and finally headed northeast (about 54°), tying the northern end of the site-survey grid strike lines. Seismic acquisition was stopped, and equipment retrieved at JD 252/1446UTC, 9 September 1990. About 25 km of seismic and magnetic data were collected during this survey. Signals from four GPS satellites were received throughout the survey, and we consider the ship's track to be accurately positioned. Seismic equipment operated well during the survey, and fair quality analog monitor records were obtained (Fig. 7), although these are somewhat noisy because of the rough seas. Reasonable correlation on a broad scale was found at all the sites between *Rig Seismic* and *JOIDES Resolution* seismic profiles (Fig. 8; Fig. 4, "Site 820" chapter; Fig. 4, "Site 821" chapter, this volume), as well as the vessels' respective GPS positions. However, because of the compressed nature of *JOIDES Resolution* analog seismic records, we found it difficult to discern detailed seismic characteristics of each site.

Site 819

Following the site-location survey, *JOIDES Resolution* returned to the confirmed GPS position of Site 819 at JD 252/1515UTC, 9 September 1990. Thrusters were lowered, and final positioning of the ship over the site was achieved using dynamic positioning. A taut-wire beacon was deployed at JD 252/1524UTC; final coordinates of Hole 819A are 16°37.439′S and 146°19.486′E, with a water depth of 565.2 m (drill-pipe measurement from sea level).

Site 819 is the most easterly of the three sites (Sites 819, 820, and 821) on the upper-slope terrace adjacent to the Great Barrier Reef and was positioned to examine the most distal

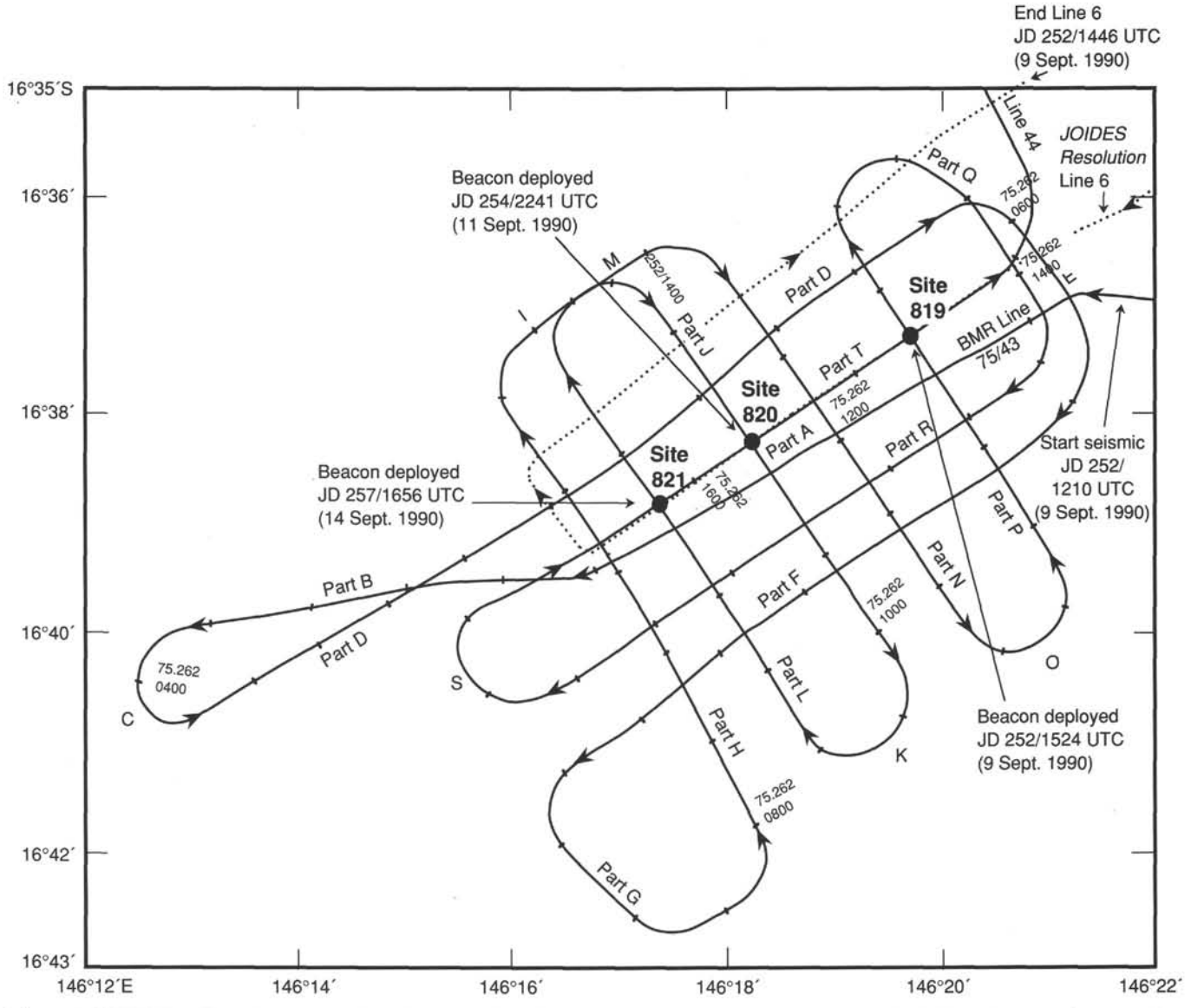

Figure 6. *JOIDES Resolution* Leg 133 site-location tracks (dotted line) and *Rig Seismic* 1987 site-survey tracks (solid line) around Sites 819, 820, and 821.

portions of the progradational and aggradational units that underlie the area (Fig. 7). Reasonable correlation at the site existed between *JOIDES Resolution* single-channel seismic profiles and *Rig Seismic* multichannel seismic profiles (Fig. 8), but details of the site were difficult to see in the *Resolution* profile. Basement is not visible in water-gun data sets across the site; however, normal-resolution Gulf aquapulse seismic data in the area (Fig. 5) indicate that it is probably about 4 s TWT below the seafloor (Symonds et al., 1983). The site is underlain by an upper, 0.21-s-TWT (169 m) thick, easterly dipping unit that contains slumps and onlaps a low-angle slump or erosional scarp at its base. The basal unit, which extends beyond TD, is about 0.27-s-TWT (280 m) thick and consists of bands of subparallel, high-amplitude reflectors that are separated by lower-amplitude zones. These reflectors are much more gently dipping than those in the overlying unit. Based on its stratigraphic position within the upper-slope depositional system, the sediments at the base of Site 819 should be older than those drilled at more landward sites.

To provide some predictive capability while drilling at Site 819, we estimated the TWT/depth relationship below the seafloor using stacking-derived interval velocities from the BMR site-survey seismic lines across the site. Figure 9 compares this relationship with similarly derived TWT/depth relationships for the adjacent Sites 820 and 821; the Great Barrier Reef lower slope, Site 822; and with those for pure carbonate slope sites on the margins of Queensland Plateau (Sites 817 and 818).

LITHOSTRATIGRAPHY

At Site 819 we recovered an expanded Pleistocene section of rhythmically bedded, hemipelagic carbonate mud that represents less than 1.48 m.y. Sediments recovered at this site reflect processes that are occurring on both the shelf and slope and thus are critical to our understanding of the development of the central northeastern Australian margin during Quaternary time. While benthic foraminifers (see "Biostratigraphy" section, this chapter) indicate upper bathyal water depths

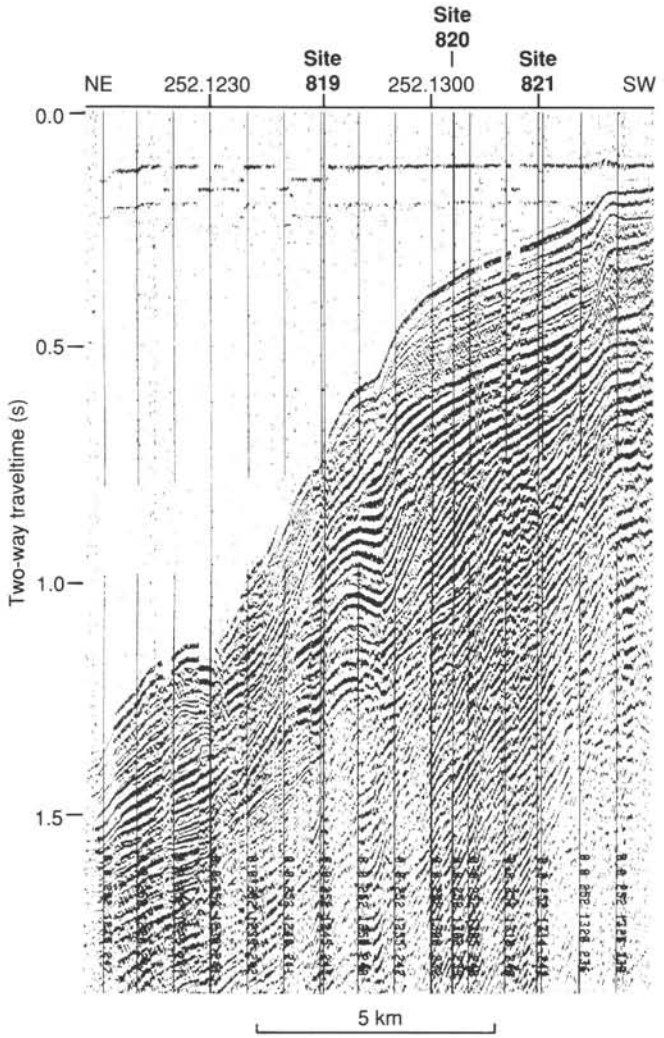

Figure 7. *JOIDES Resolution* shipboard analog single-channel seismic profile collected during site-location survey for Sites 819 through 821, using two 80-in.^{3} water guns. Seismic tie between the three sites is shown.

(200–600 m) for the entire cored interval, substantial variations in contents of carbonate and clay suggest deposition dominated by changes in Pleistocene sea level and fluctuating fluvial influx.

Lithologic Units

Five major lithologic units were identified (Fig. 10) and variously subdivided on the basis of their lithologic composition, calcium carbonate content, and by comparison with downhole logs. These are (1) rhythmically interbedded dark green, clay-rich and light green, carbonate-rich nannofossil clayey ooze with pteropods (Unit I), (2) clayey nannofossil oozes with numerous mixed carbonate/siliciclastic silt intercalations (Unit II), (3) rhythmically bedded bioclastic and micritic oozes (Unit III), (4) interbedded bioclastic wackestones and nannofossil clayey oozes with quartz and mixed carbonate/siliciclastic silt stringers (Unit IV), and (5) chalks to chalky claystones (Unit V). Stratigraphic position and gross lithologic subdivision of these units is shown in Figure 10, together with associated carbonate content values, downhole gamma-ray and resistivity logs, nannofossil age dates, and estimated rates of sedimentation. Three probable slump-related hiatuses occur within the section: (1) near the middle of Core 133-819A-4H and separating Units I and II; (2) at the base of Core 133-819A-8H (about 75 mbsf), and (3) at the base of Core 133-819A-20X and separating Units II and III. Subtle rhythmic couplets of strata are identifiable throughout the recovered section, but with decreasing resolution with increasing age. With some exceptions, these couplets were identified by a general upward-coarsening from clay-rich, dark greenish-gray oozes through relatively carbonate-rich, commonly bioclastic, greenish-gray oozes to wackestones. Carbonate contents, magnetic susceptibilities (see "Paleomagnetism" section, this chapter), and wireline logs generally track the cyclicity of these sedimentation couplets, and all were used to help refine the downhole positions and transitions of these cycles. A summary of stratigraphic occurrences of discernable couplets is given in Table 2 and illustrated in Figure 10.

Unit I (Core 133-819A-1H to Section 133-819A-4H-3; depth, 0 to 32.5 mbsf; age, late Pleistocene)

Unit I consists of rhythmically bedded couplets of dark greenish-gray, clay-rich and greenish-gray, carbonate-rich, clayey pteropod ooze. Each couplet averages about 9.6 m long. Percentages of calcium carbonate increase from a dark green base up through a lighter green top portion of each couplet. Both half-couplets of each cycle are moderately bioturbated and contain fine bioclastic debris. On the basis of only 3.5 couplets in the section and available age data, each couplet exhibits an average age duration of about 104,700 year, near that of the astronomical period of eccentricity (cf. Berger, 1978). Gritty, pteropod-rich layers about 5 to 80 cm thick occur near the base of the three youngest couplets that may correspond to the three most recent interglacial/glacial transitions. A hiatus separates Unit I from Unit II and is identified by steeply inclined bedding, a paleontological hiatus (cf. "Biostratigraphy" section, this chapter), and a rapid change in contents of calcium carbonate.

Unit II (Sections 133-819A-4H-3, 32.5 cm, to -11H-2; depth, 32.5–97.0 mbsf; age, Pleistocene)

Unit II consists of predominantly dolomitic clayey nannofossil oozes and is distinguished chiefly by the presence of abundant intercalations of silt. These silts occur as thin (<1 cm) nongraded layers and as burrow fills that contain silt-sized bioclastic and siliciclastic grains. Silt layers are dominant at the base of the unit (approximately Sections 133-819A-11H-2 through -8H-3), where they are estimated to range between 5% and 30% of the core volume by section. Above this silty basal interval, silt fractions have dispersed throughout the sediment from Sections 133-819A-7H-7 to -6H-3, and above this, the silts are absent throughout the remainder of the unit. Interestingly, percentages of nannofossils, estimated from smear slides, tend to follow a similar abundance trend as that of silt intercalations and decrease from the base of the unit upward. Clayey nannofossil oozes to chalks occur at the top of the unit and are similar to the lithologic assemblages of Unit I. A probable slump discontinuity is visible in seismic profiles (see "Seismic Stratigraphy" section, this chapter) and is recognizable as inclined strata at the base of Core 133-819A-8H (133-819A-8H-8 to -8H-CC).

A package of five rhythmic couplets of upward-coarsening strata were differentiated in Unit II (Cycles IIB to IIF; Fig. 10 and Table 2). These couplets average about 13 m thick and are similar to those in Unit I, except that the couplets of Unit II are thicker and contain appreciably higher quantities of silici-

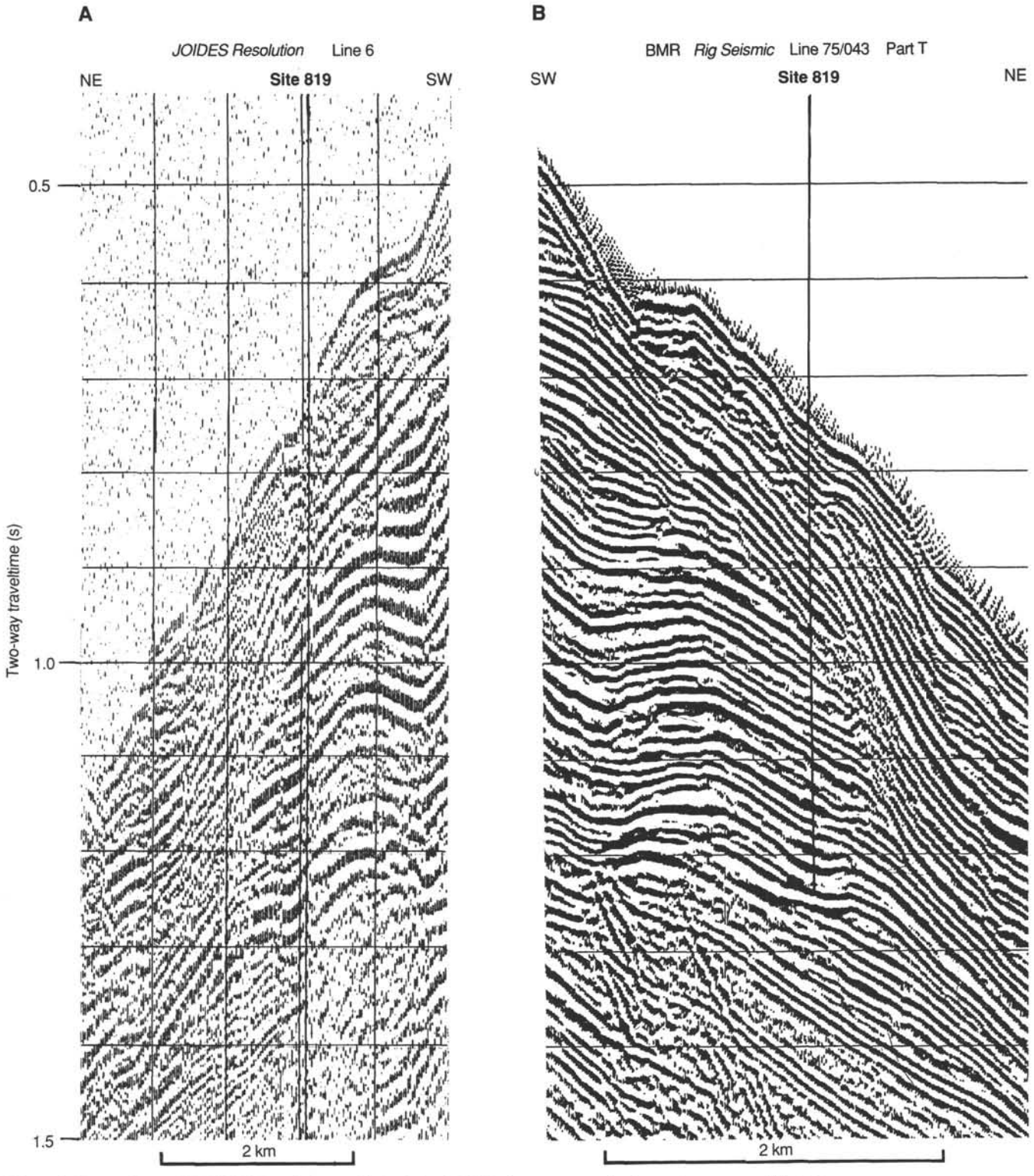

Figure 8. Comparison of *JOIDES Resolution* and *Rig Seismic* 80-in.^{3} water-gun seismic profiles across Site 819.

clastic sand and silt. Using a sedimentation rate of 4.8 cm/1000 year (Fig. 10), we calculated an average duration of about 183,000 year per couplet. Upward-fining sediments enclose both the top and bottom of the upward-coarsening package (Table 2) and respectively mark the transitions between Units I and II and between Units II and III.

Unit III (Sections 133-819A-11H-2, 0 cm, to -21X-1, 9 cm; depth, 97.0 to 179.7 mbsf; age, Pleistocene)

Unit III consists of rhythmically interbedded bioclastic and micritic oozes (Fig. 10). Carbonate contents are similar to those in Unit II (Fig. 10), but generally decrease upward in

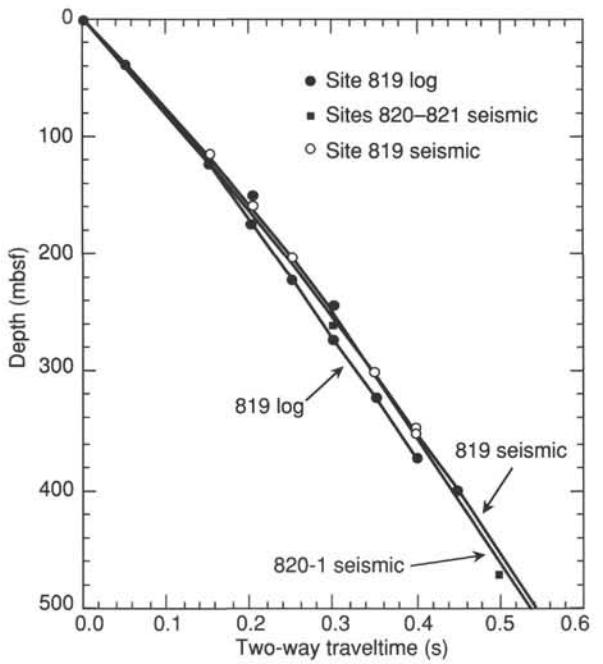

Figure 9. Comparison of TWT/depth curve estimated for Site 819 with those for Sites 820 and 821.

response to an increasing proportion of siliciclastic mud. Bioclastic silt-sized grains tend to increase toward the base of the unit, where calcium carbonate contents reach their acme for the site.

With minor variations (i.e., the basal portion of couplets IIIC and possibly IIIE), at least six somewhat poorly defined, coarsening-upward rhythmic couplets were identified in this unit (Fig. 10; Table 2). These consist of an often sharp-based, dark greenish-gray, clay- and quartz-rich and carbonate-poor basal half that passes gradationally upward through a lighter green carbonate and bioclastic-rich clayey ooze to chalk. The frequency of the cycles in this unit is uncertain owing to limited age control and major slumping at the base of the unit. A diagram of one of these couplets is shown in Figure 11. A gap exists between Units III and IV that represents the unrecovered interval from 179.7 to 198.1 mbsf.

Unit IV (Cores 133-819A-23X to -35X; depth, 198.1 to 313.2 mbsf; age, Pleistocene)

Unit IV consists of interbedded bioclastic wackestones and nannofossil clayey oozes with quartz and silt stringers. The top of the unit lies at the top of Core 133-819A-23X, where a seismically defined major slump occurs. The base of the unit is defined as the top of the underlying chalks of Unit V. Relative to Units I through III above, carbonate contents are low in Unit IV and sediments are of a mixed terrigenous/neritic to upper bathyal carbonate origin. Further, the sediments of this unit contain not only a higher proportion of terrigenous clay, but also a higher proportion of quartz silt and sand relative to the units above, especially near the base of the unit, where three upward-coarsening cyclic sedimentation packages have been defined (couplets IV-E to IV-C, Cores 133-819A-35X to -31X; Fig. 10; Table 2).

Six upward-coarsening couplets having two intervening upward-fining couplets were identified in Unit IV (Fig. 10, Table 2). In Cores 133-819A-29X to -30X, the sediments fine upward and consist of wackestones and clayey nannofossil oozes with bioclasts and thin discontinuous silt intercalations (couplet IVC-1), before again coarsening upward in bioclastic debris and increasing carbonate content from Section 133-819A-29X-1, 100 cm, to -26X-1, 25 cm, where a hard dolomitic limestone occurs (couplet IVB). Above this limestone, sediments pass upward from light greenish-gray, silty, nannofossil ooze to wackestone with sporadic silt layers, into darker green clayey nannofossil oozes that contain abundant silty packstone intercalations.

Unit V (Cores 133-819A-36X to -44X; depth, 313.2 to 400 mbsf; age, Pleistocene)

Unit V is the lowermost unit at Site 819 and consists of a relatively homogeneous sequence of dark greenish-gray, bioclastic clayey chalks at the base, micritic clayey chalks in the middle, and clayey bioclastic nannofossil chalks in the uppermost part (Fig. 10). Carbonate contents are relatively uniform, and few variations in grain size in this unit are relative to Units I through IV. Analysis of smear slides indicates that quartz increases in abundance up through the middle micritic portion of the section.

Summary and Interpretation

Sediments at Site 819 represent an upper bathyal, mixed carbonate/terrigenous assemblage of largely rhythmically bedded facies that have developed in response to Pleistocene fluctuations in sea level as well as to variations in terrigenous source influx. The general depositional setting for all five units has been interpreted as being an upper-slope environment, perhaps distally tapping fluviodeltaic terrigenous sources. The more than 25 upward-coarsening couplets identified from the upper 320 m of section at this site attest to the general persistence of mechanisms that dominate the overall depositional regime. However, the dramatic upward decrease in sedimentation rates for this site and the overall increase in nannofossil percentages from Units V through II suggest that water depths have progressively increased throughout the deposition of the section. At present, it is difficult to determine how much of this general deepening over the last ca. 1.5 Ma results from control of eustatic sea level (i.e., second- to third-order changes in sea level) vs. tectonic subsidence (e.g., Falvey and Taylor, 1974; Davies et al., 1989), and further study will be needed to differentiate these effects.

The upward-coarsening sequences of dark green through lighter green oozes to wackestones at Hole 819A reflect upward-decreasing proportions of siliciclastic mud and increasing proportions of shallow-water bioclastic detritus, and the ca. 100,000-year period of the couplets in Unit I clearly emphasizes the importance of variations in eustatic sea level as an important control in their development. Although our shipboard interpretations of these sedimentary rhythms remain tentative, we speculate that the basal clay-rich half-couplets of each cycle may relate to enhanced terrigenous influx during declines in relative sea level and that their coarser upper portions correspond to relative rises of sea level when neritic carbonate production is at a maximum and carbonate detritus is shed toward the basin. This interpretation is in accord with recent studies that relate increases in carbonate production and basin filling to interglacial episodes (cf. Droxler and Schlager, 1985; Boardman et al., 1986), but is unlike that for upward-coarsening sequences that typify many shoaling terrigenous-dominated settings (e.g., prograding wave-dominated clastic shore lines or interregional fluviodeltaic systems). Testing this model and differentiating other possible effects (such as carbonate progradation during lowstands of relative sea level episodes) awaits further shore-based sedimentological and isotope studies and detailed correlations with Sites 820, 821, and 822.

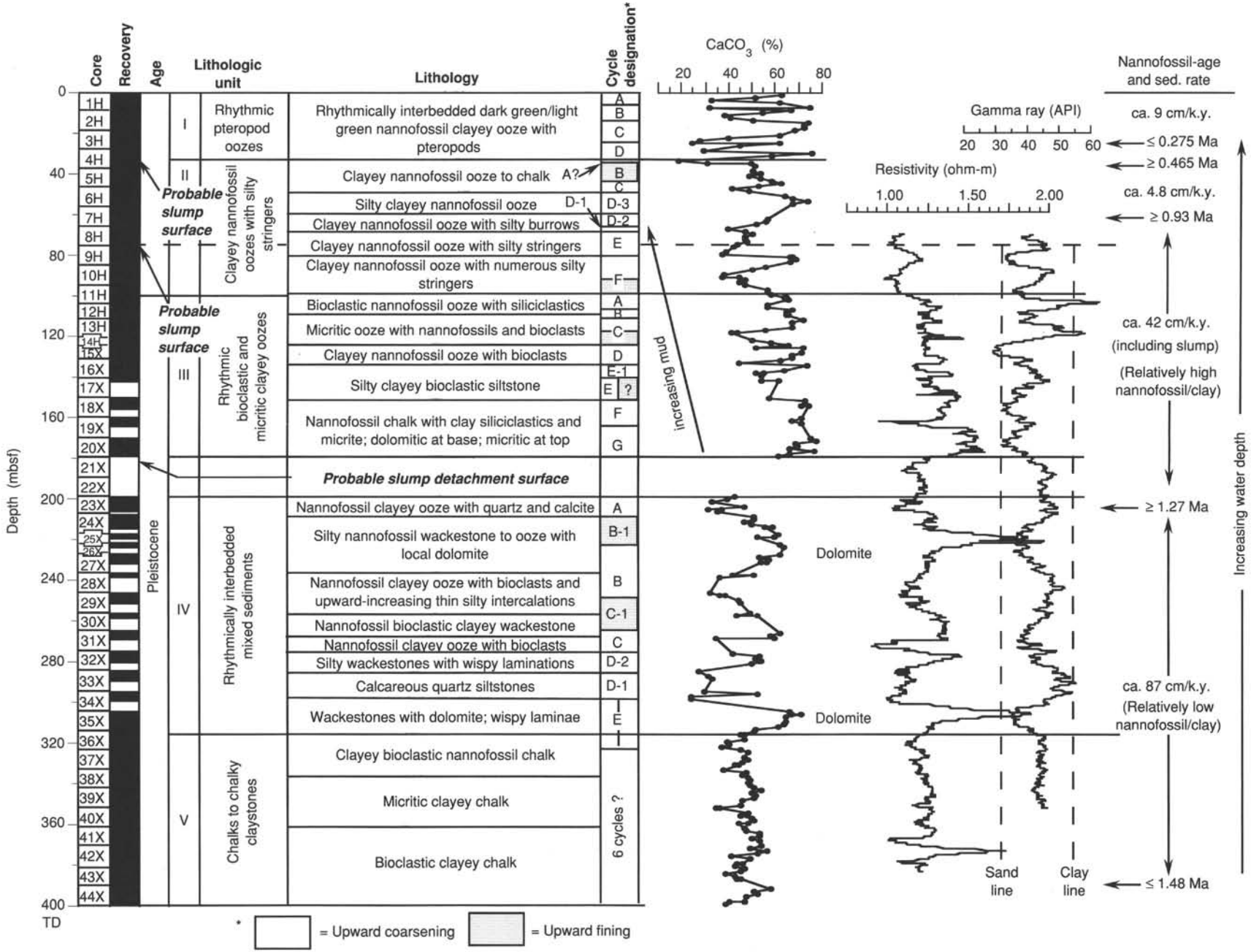

Figure 10. Lithology of Hole 819A, illustrating Units I–V, rhythmic upward-coarsening and upward-fining lithologic cycles (couplets), and corresponding variations in downhole carbonate content and gamma-ray and resistivity logs. Overall large upsection decrease in sedimentation rates is interpreted to reflect a progressive deepening of the site with time.

Table 2. Rhythmic couplets at Hole 819A.

Unit	Couplet	Interval (cm)	Comment
I	A	1H-1, 0 to 1H-5, 20	CU
	B	1H-5, 0 to 2H-4, 150	CU
	C	2H-4, 250 to 3H-5, 65	CU
	D	3H-5, 65 to 4H-4, 65	Top half of couplet only.
II	A	4H-4, 90 to 4H-5, 120	CU; bottom <1/4 of couplet.
	B	4H-5, 120 to 5H-5, 120	FU
	C	5H-5, 120 to 6H-3-10	CU; lower contact gradational.
	D-3	6H-3, 10 to 7H-3, 0	CU; base very silty.
	D-2	7H-3, 0 to 8H-1, 0	CU; silt-filled burrows in lower half-couplet.
	D-1	8H-1, 0 to 8H-3, 55	CU
	E	8H-3-55 to 9H-4-135	CU; passes through slump at base of Core 133-819A-8H
	F	9H-4, 135 to 11H-2-150	CU/FU; fines up in lowest part. Upper and lower contacts gradational. Numerous silt stringers throughout.
III	A	11H-2, 150 to 12-2, 150	CU; basal contact gradational; large bivalves.
	B	12H-2-150 to 12H-CC, 20	CU; base defined by carbonate; no lower dark green half couplet; large bivalves throughout.
	C	12H-CC, 20 to 15X-1, 90	FU/CU; basal portion fines from bioclasts up through siliciclastic oozes; large articulated bivalves at FU/CU transition.
	D	15X-1, 90 to 16X-3, 60	CU; basal contact gradational and bioturbated. Short lower half-couplet.
	E-1	16X-3, 60 to 17X-1, 0	CU; very poor recovery in Core 133-819A-17X. Silty intercalations in lower half-couplet.
	E	17X-1, 0 to 18X-1-60	CU/FU; gamma ray suggests FU cycle.
	F	18X-1-60 to 19X-3, 169	CU; abrupt contact between half-couplets. Quartz increases up section.
	G	19X-3, 169 to 21X-1-9	CU; dolomitic upper couplet; only 10 cm of base present.
IV	A	23X-1, 0 to 23X-3-50	CU; multiple silt stringers at top.
	B-1	23X-3, 50 to 26X-1, 25	FU; base of couplet contains corals and bryozoans.
	B	26X-1, 25 to 29X-1, 100	CU; chalky and hard dolomitic layer at top.
	C-1	29X, 100 to 31X-1, 0	FU; large shells at base.
	C	31X-1, 0 to 32X-105, 0	CU; sharp contact between couplets.
	D-2	32X-1, 105 to 33X-1, 150	CU
	D-1	33X-1, 150 to 34X-3, 85	CU; dolomitic Quartz and calcite + Calc siltstones at base.
	E	34X-3, 85 to 36X-CC, 45	CU; base in Unit V chalks.

CU = upward-coarsening. FU = upward-fining.

BIOSTRATIGRAPHY

Introduction

Only Pleistocene sediments were penetrated in Hole 819A (Fig. 12). In general, planktonic nannofossils and foraminifers are very well preserved, except for Cores 133-819A-15H through -21H. The bottom of the hole represents the lower Pleistocene (1.27–1.48 Ma), as indicated by nannofossil markers. Benthic foraminifers are abundant, and species assemblages indicate an upper bathyal environment throughout the hole.

Calcareous Nannofossils

An expanded Pleistocene section (400 m in <1.48 m.y.) was recovered from Hole 819A. These sediments are rich in calcareous nannofossils; preservation of nannofossils is generally excellent, except in Cores 133-819A-15X through -21H, where it is moderate to poor.

Sample 133-819A-1H-5, 150 cm, yielded abundant *Emiliania huxleyi* and *Gephyrocapsa oceanica*; its age is younger than 0.275 Ma. As *E. huxleyi* dominates the assemblage, the sample can be correlated to the *Emiliania huxleyi* Acme Zone and may be younger than 85 k.y. Relative abundance of *E. huxleyi* is greatly reduced in Samples 133-819A-2H-CC and -3H-5, 150 cm, where the relative abundance of *Gephyrocapsa oceanica* increases and small-size *Gephyrocapsa* dominate the assemblages. Thus, these two samples were assigned to Zone CN15 (0–0.275 Ma). Samples 133-819A-4H-5, 150 cm, through -6H-CC were placed in Subzone CN14a (0.465–0.93 Ma) on the basis of the occurrence of *Pseudoemiliania lacunosa* from this level downward, along with common large species of *Gephyrocapsa* (*G. oceanica* and *G. caribbeanica*), as well as common to abundant small *Gephyrocapsa*.

In Sample 133-819A-7H-CC and for some distance downward to Sample 133-819A-23H-CC, large species of *Gephyrocapsa* are rare, and small specimens of *Gephyrocapsa* dominate the assemblage. This interval of small *Gephyrocapsa* belongs to the upper part of Subzone CN13b and has an age of 0.93 to 1.27 Ma.

The highest occurrence of *Helicosphaera sellii* was found in Sample 133-819A-23X-CC. Rare-to-few specimens of this species also were found in Samples 133-819A-24X-CC, -26X-CC, -27X-CC, -33X-CC, -42X-CC, -43X-CC, and -44X-CC. None of these samples contains *Calcidiscus macintyrei*, and hence, the entire interval from Sample 133-819A-23X-CC downward was assigned to the lower part of Subzone CN13b, which has a narrow age range of 1.27 to 1.48 Ma.

Planktonic Foraminifers

Generally, planktonic foraminifers are well preserved in the sediments recovered from Hole 819A. The abundance of specimens shows a high variability, which may relate to the cyclic color changes in the upper part of the record; the light intervals contain abundant, while the dark layers yield rare, planktonic foraminifers. Poor preservation was found in Samples 133-819A-15H-CC through -21H-CC. The entire hole can be assigned to Zone N22-N23 because *Globorotalia truncatulinoides* occurs throughout. Late Pleistocene planktonic foraminifers are *Globi-*

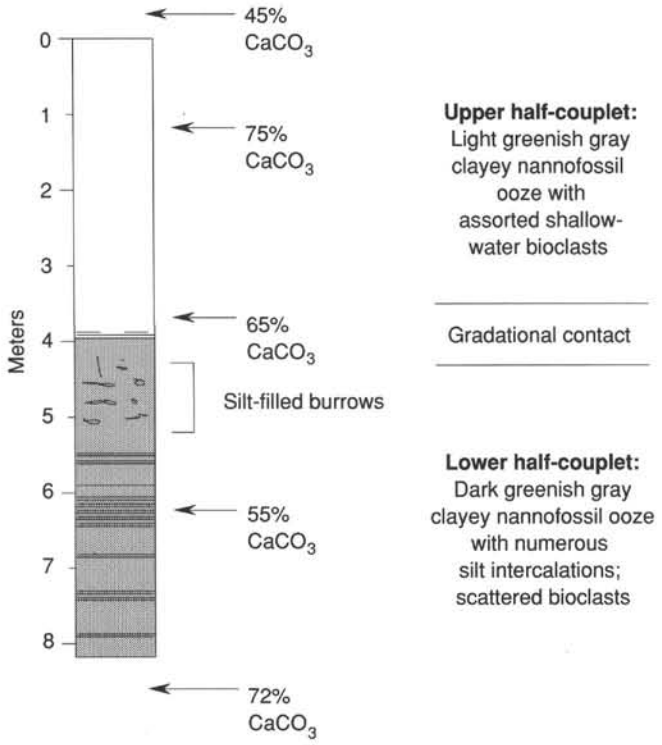

Figure 11. Schematic illustration of a typical upward-coarsening sedimentary couplet at Site 819 (couplet III-E-1; see Fig. 10).

gerina rubescens pink (only in Sample 133-819A-1H-CC), *Globigerinoides ruber* pink (only in Sample 133-819A-3H-CC) and *Globigerina rubescens* white in Cores 133-819A-1H through -13H. Also in the latter interval, sparse specimens of *Globigerinella calida calida* can be found.

Benthic Foraminifers

Core-catcher samples examined from Hole 819A contain well-preserved benthic foraminifers. These benthic foraminiferal assemblages indicate an upper bathyal paleodepth (200–600 m) for Hole 819A.

Most of the core-catcher samples examined contain the upper bathyal species associations that include the depth indicators *Bulimina marginata, Bulimina mexicana, Cibicidoides bradyi, C. cicatricosus, C. mundulus, Hanzawaia mantaensis, Hoeglundina elegans, Hyalinea balthica, Lenticulina peregrina, Nuttallides umbonifera, Sigmoilopsis schlumbergeri, Sphaeroidina bulloides, Uvigerina peregrina, U. pigmaea,* and *U. proboscidea* (van Morkhoven et al., 1986). In addition to these taxa, Sample 133-819B-1H-CC contains *Bulimina exilis,* which has a depth range of 500 to 1000 m. The presence of this species with *Bulimina marginata* indicates a paleodepth of 500 to 600 m for this sample. Sample 133-819B-1H-CC also contains abundant *Bulimina aculeata.* This same sample yields abundant *Globigerina bulloides,* which is an indicator of high productivity. *Bulimina aculeata* has been found to prefer nutrient abundance and to have great tolerance for high salinities and oxygen deficiency. In addition, it has been correlated to high carbon values in certain areas (van Morkhoven et al., 1986).

Most of the samples that we examined included at least a small component of transported specimens, such as *Amphistegina* spp., *Discorbis* spp., *Elphidium* spp., and *Planorbulina* spp. However, we were unable to distinguish benthic foraminifers that may have been transported downslope within the upper bathyal zone.

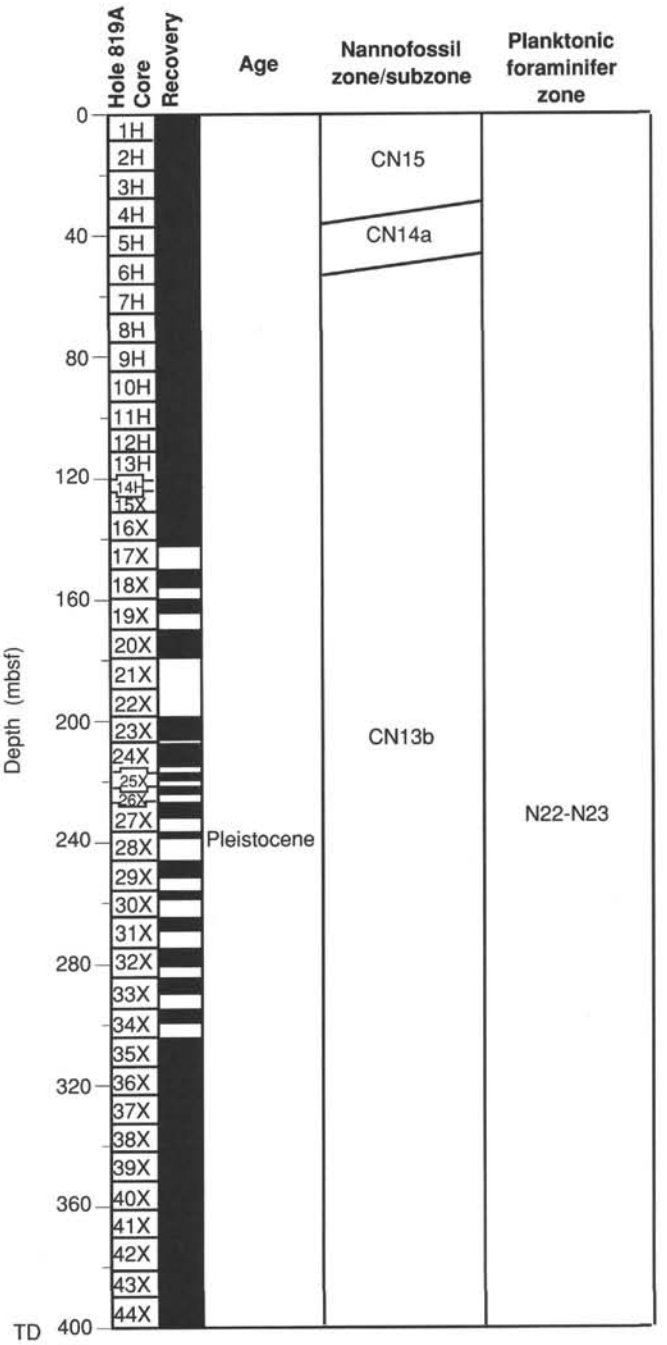

Figure 12. Overview of preliminary biostratigraphy of Site 819.

PALEOMAGNETISM

Good recovery and a stable remanent magnetization, recorded in the mixed carbonate-siliciclastic sediments cored to a depth of 400 mbsf in Hole 819A, allowed us to identify several magnetic polarity reversal zones, some of which can be correlated with the geomagnetic polarity time scale. However, this correlation was complicated by the possibility of both overprinting and remagnetization. Preliminary correlation, which has been constrained by the available shipboard

biostratigraphic data, indicates that the cored section is of Pleistocene age.

Cores 133-819A-4H through -14H were collected using the APC system, coupled to the shipboard multishot core-orientation tool. Cores 133-819A-15X to -44X were collected using the XCB system; thus, azimuthal orientation was not maintained. For this reason, only inclination data obtained from these cores were used to interpret polarity.

Paleomagnetic analyses of sediments recovered from Hole 819A included determination and measurement of whole-core magnetic susceptibilities, performed at 10-cm intervals, and of natural remanent magnetization (NRM) for archive-halves of the cores, both before and after alternating field (AF) demagnetization at 15 mT. In the majority of cores, demagnetization at 15 mT was adequate to remove most of the soft overprint(s), thereby allowing us to interpret preliminary depositional or early post-depositional remanence. However, polarity zones clearly conflict with the biostratigraphic age markers and may represent an overprinted or remagnetization signal.

Variation of inclinations after 15 mT AF demagnetization, NRM intensity, and volume susceptibility with depth is shown in Figure 13. NRM intensity of the cored sediments typically ranges from 0.1 to 10 mA/m, with most values around 1 mA/m. These values are well above the minimum sensitivity of our shipboard magnetometer and approximately one order of magnitude greater than the NRM intensities observed in pelagic carbonate sequences. After 15 mT demagnetization, the average remanence intensity declines to about 0.5 mA/m, thus providing a rough estimate of the median destructive field (MDF) and coercivity of the remanence carrier. A MDF at approximately 15 mT suggests that the remanence in these sediments perhaps is held by multidomain magnetite.

As depicted in Figure 13, a complete record of variations in volume magnetic susceptibility with depth was obtained at 10-cm intervals for the hole. Susceptibility of the recovered sediments is positive and ranges from approximately 2×10^{-6} to 40×10^{-6} cgs units, while most values range between 5×10^{-6} to 6×10^{-6} cgs units. A striking feature of a plot of downhole volume susceptibility is the occurrence of a number of large spikes in the uppermost 20 m of the cored section, which corresponds to higher NRM intensity (Fig. 13).

The sequence of magnetic polarity zones (magnetozones) identified in Hole 819A is shown in Figure 14. We recognized six normal and six reversed magnetozones for the cored section. Available biostratigraphic data (see "Biostratigraphy" section, this chapter) indicate a Pleistocene age (<1.48 Ma) for the cored section. A long interval of normal polarity is present in the upper part of the section (0–73.5 mbsf) that contains evidence of at least one short polarity change at 40.6 mbsf. We interpreted this uppermost normal zone to represent the Brunhes chron, while the Brunhes/Matuyama boundary was tentatively placed at about 66 mbsf. Below this (from about 66 to 80 mbsf), we measured a predominantly reversed polarity that is separated by a thin normal polarity section. From 80 to about 150 mbsf, zones of normal and uncertain polarity dominate. In the depth interval from 150 to 400.0 mbsf, mainly reversed and uncertain polarity zones occur that perhaps correlate with the Matuyama reversed chron. Within the Matuyama, at least five intervals of predominantly normal polarity can be seen. Of the normal polarity zones, the longest occurs between about 80.0 and 140 mbsf and has been interpreted to represent a strong normal overprint/remagnetization or perhaps an extremely expanded Jaramillo subchron (0.73–0.92 Ma). Three thin, normal polarity zones at about 217, 276, and 305 mbsf may represent short excursions in the magnetic field, if indeed they are real. In addition, a predominantly normal polarity zone was measured from 369 to 371 mbsf. Correlation of this zone with the geomagnetic polarity time scale is uncertain. Biostratigraphically, the sediments at this depth are less than 1.48 Ma in age and should be located above the Olduvai subchron at 1.66 Ma.

Collection of 424 oriented discrete paleomagnetic samples for post-cruise study should help to resolve and refine our preliminary interpretation and age assignment.

SEDIMENTATION RATES–SITES 819, 820, 821

Sites 819, 820, and 821 have been combined for discussion of sedimentation rates because these sites are along a slope transect and because the history of the three sites is similar for the cored interval. At all three sites, we recovered only Pleistocene sediments, and in each case, the 400 m of penetration ended in the lower Pleistocene. The highest occurrence datum, *Helicosphaera sellii,* (1.27 Ma) was penetrated in all three holes, but the next lower datum, the highest occurrence of *Calcidiscus tropicus* (1.48 Ma) was not reached in any of the three. Plots of depth vs. age for the three sites are given in Figure 15. At each site, we recognized four biohorizons, which have been tabulated in Table 3. The first biohorizon is the lowest occurrence of *Emiliania huxleyi,* which (within the limits of sample spacing) is at approximately the same depth at each site (26–35.5 mbsf at Site 819; 26.2–35.7 mbsf at Site 820; and 23.4–32.9 mbsf at Site 821). Consequently, the sedimentation rate to this point at the three sites essentially remains the same—about 10 to 11 cm/k.y. The next lower datum is the highest occurrence of *Pseudoemiliania lacunosa* (0.465 Ma), which is between 26 and 35.5 mbsf at Site 819, the same depth as the lowest occurrence of *Emiliania huxleyi.* Clearly, the interval for 27 to 35.5 mbsf contains a significant hiatus. At Site 820, this datum is between 92.7 and 102.2 mbsf and at Site 821, it is between 118.4 and 127.9 mbsf. The sedimentation rate from the *Emiliania huxleyi* lowest occurrence datum to the *Pseudoemiliania lacunosa* highest occurrence datum at these last two sites is 35 and 49.2 cm/k.y., respectively, which is well above those of the interval immediately above.

The next recognizable datum is the top of the interval of dominance of small *Gephyrocapsa* (0.93 Ma), which at the three sites is between 54.5 and 62.5 mbsf (Site 819), 130.7 and 140.2 mbsf (Site 820), and 174.9 and 184.6 mbsf (Site 821). Corresponding sedimentation rates for the interval immediately preceding this datum at the three sites are 6, 8.2, and 12.2 cm/k.y, respectively. The remaining datum, the highest occurrence of *Helicosphaera sellii,* is between 198.1 and 207.4 mbsf (Site 819), 270.4 and 280.1 mbsf (Site 820), and 270.8 and 280.4 mbsf (Site 821), while the sedimentation rates between this and the next higher datum are 42.4, 41.1, and 28.2 cm/k.y., respectively. Disregarding the hiatus at Site 819, the sedimentation rate (although it changes much within the Pleistocene) follows a nearly identical pattern at all three sites: a relatively high rate of 28 to 42 cm/k.y. during the mid-Pleistocene (1.27–0.93 Ma); a more modest rate of 6.0 to 12.2 cm/k.y. from 0.93 to 0.465 Ma; a sharply higher rate of 35.0 and 49.2, again from 0.465 to 0.275 Ma; and again, a more modest rate of 10.3 to 11.3 cm/k.y. during the latest Pleistocene (0.275–0 Ma).

These notable changes in sedimentation rate obviously bear some relationship to lithologic changes in the sediment; however, the scale of lithologic changes is such that a sampling interval of approximately 9.5 m would not consistently sample the most characteristic or dominant lithology for that interval.

INORGANIC GEOCHEMISTRY

Interstitial Waters

Interstitial fluids were taken from the first 10 cores of Hole 819A and from Cores 133-819A-13H, -16H, -19X, -23H, -25X,

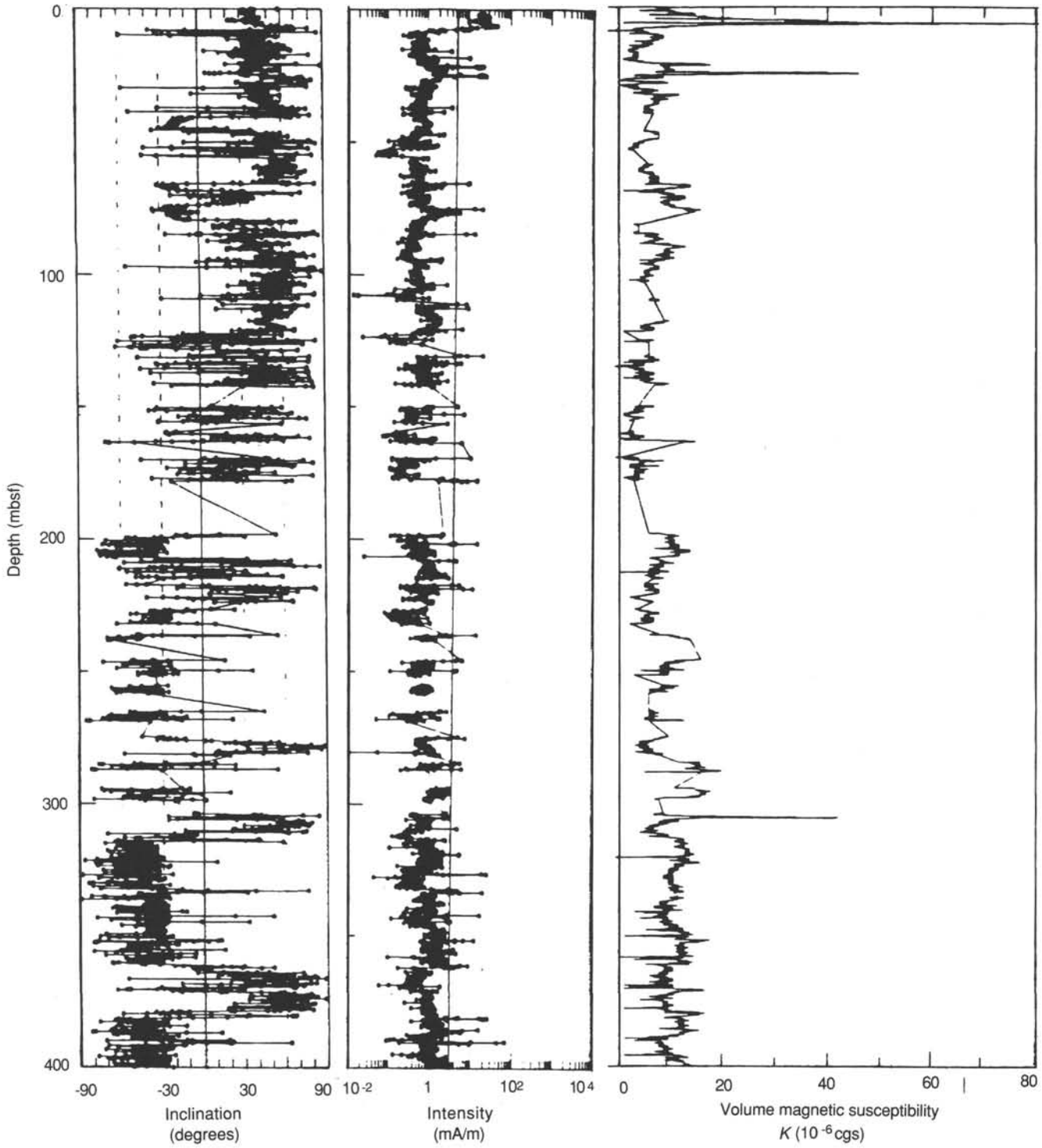

Figure 13. Inclination after 15 mT AF demagnetization, NRM intensity, and volume magnetic susceptibility plotted vs. depth for Hole 819A.

-28X, -31X, -34X, -37X, -40X, and -43X. Samples from Hole 819A were analyzed according to the procedures outlined in the "Explanatory Notes" chapter (this volume). These data are listed in Table 4 and Figures 16, 17, and 18.

Calcium, Magnesium, Potassium, and Strontium

Concentrations of Ca^{2+} decrease below values of surface seawater (10.36 mM) in Core 133-819A-1H (5.95 mbsf) to a minimum of 2.86 mM at 91.90 mbsf (Fig. 16). Magnesium also decreases in concentration from 48.54 mM at 5.95 mbsf to 13.89 mM at 91.9 mbsf. Concentrations of potassium decrease from 12.3 to 5.64 mM over the same interval (Fig. 16). When normalized to Cl^-, a net loss of 8 mM of Ca^{2+} and 36 mM of Mg^{2+} was observed (Fig. 17). This loss occurs mainly as precipitation of authigenic calcite and dolomite, although Mg^{2+} and K^+ also are consumed during alteration of clay minerals.

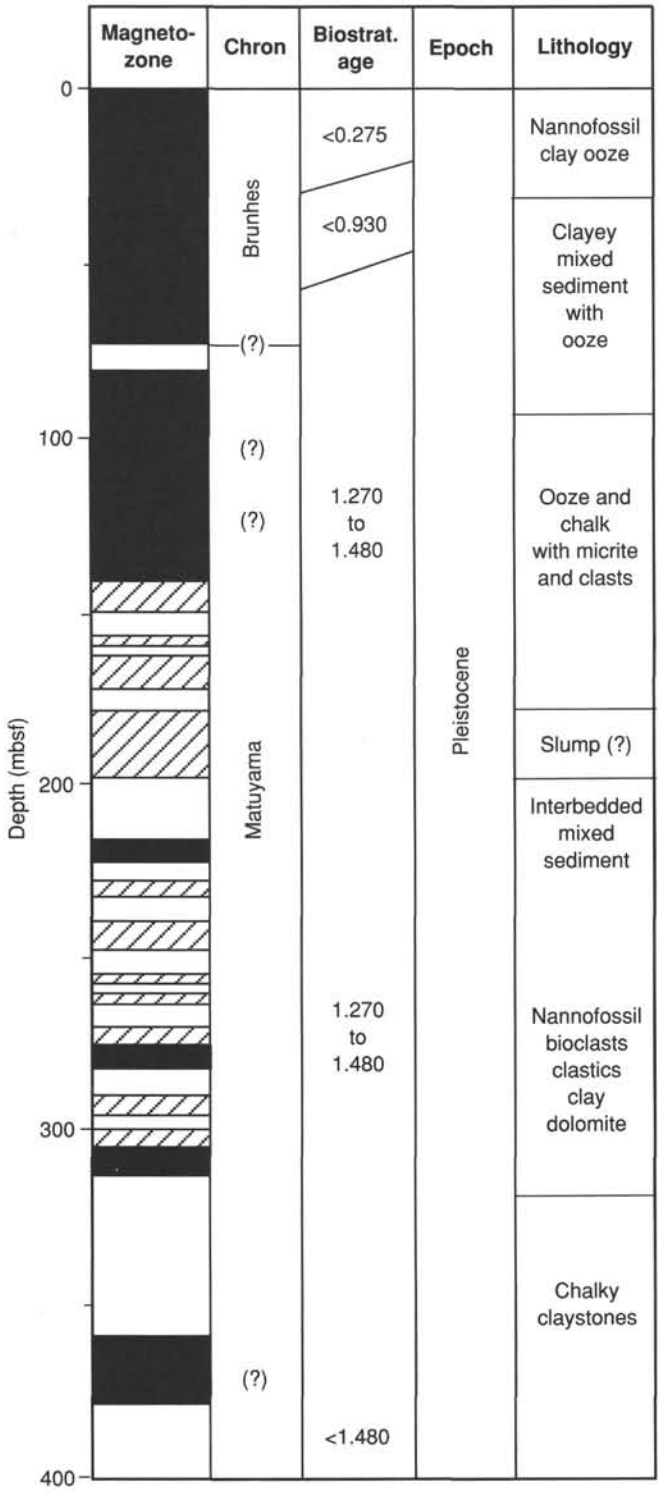

Figure 14. Magnetozones for Hole 819A, based on 15 mT AF demagnetization. Gaps in data resulting from poor recovery or uncertain polarity are shown by hatched patterns.

Concentrations of Sr^{2+} increase rapidly with sub-bottom depth and attain a maximum of 483 μM at 168.80 mbsf (Fig. 16). Below this depth, the content of Sr^{2+} slowly decreases to concentrations between 170 and 200 μM between 243.4 and 387.8 mbsf. The initial increase in the concentration of Sr^{2+} is primarily a result of the precipitation of LMC and dolomite. Decreases in the lower portion of Hole 819A may be a result of the removal of Sr^{2+} during diagenesis of clay minerals and a lower rate of recrystallization of the carbonate portion of the sediment.

Alkalinity, Sulfate, and Phosphate

Alkalinity increases in Hole 819A to 11.6 mM at 25.45 mbsf. This increase in alkalinity is accompanied by a removal of sulfate, which decreases to zero at 25.45 mbsf.

According to the normal stoichiometry of sulfate reduction, 2 mM of alkalinity should be produced for every 1 mM of sulfate used during oxidation of organic material. Hence, in the absence of carbonate precipitation, an increase in alkalinity of 56 mM should occur. The absence of such an increase and the large decreases in Ca^{2+} and Mg^{2+} necessitate the removal of alkalinity, either through clay mineral reaction and/or precipitation of carbonate phases.

Salinity and Chlorinity

Chlorinity at Site 819 shows considerable variation (Fig. 18). These changes are probably related to changes in chlorinity of seawater during glacial and interglacial periods. As a result of the removal of Ca^{2+}, Mg^{2+}, HCO_3^-, and SO_4^{2-} during diagenetic reactions, the relationship between salinity and chloride is not conservative. As may be seen in Figure 18, samples that exhibit a conservative relationship should plot on a line of normal salinity vs. Cl^-. All samples from Hole 819A exhibit an excess of Cl^- with respect to their measured salinities.

Carbonate Content and X-Ray Mineralogy

Percentages of aragonite, LMC, HMC, quartz, and dolomite were determined for interstitial-water sediment samples. The HMC/LMC ratio was calculated using relative peak heights. As a result of the highly complex nature of these sediments, peak heights, rather than areas, were used to determine mineral percentages. In addition, to determine the type of clay minerals present, we prepared oriented samples using the clay fraction. These samples were scanned between 2° and 40° 2θ. The samples then were heated for 60 min at 550°C and X-rayed again.

Carbonate Content

The carbonate content of sediments at Site 819 varies between 10% and 90% (Fig. 19 and Table 5). Although the precise age of these sediments remains uncertain and will need to be resolved using oxygen isotope stratigraphy, numerous alternations between sediments having high (70% to 80%) and low (30% to 40%) carbonate might relate to glacial and interglacial periods.

Mineralogy

The mineralogy of the sediments at Site 819 comprises aragonite, LMC, HMC, quartz, kaolinite, albite, and illite (Table 6, Figs. 20 and 21). Variable amounts of dolomite also occur, particularly between 35 and 65 mbsf. Although we do not know whether this dolomite is authigenic or detrital, it may be significant that the distribution of the dolomite corresponds with a maximum in alkalinity. Such conditions have been suggested to promote dolomite formation. In this case,

the source of this Mg^{2+} may be both the ambient pore fluid and the dissolution of HMC.

ORGANIC GEOCHEMISTRY

In addition to safety monitoring for hydrocarbons, the main purpose of our shipboard organic geochemistry studies at Site 819 was to assess the amount and origin of organic matter preserved in Pleistocene sediments deposited in front of the present-day Great Barrier Reef. A second purpose was the characterization of proportions of different light hydrocarbons that were generated in the sediments through biogenic or thermogenic decay of organic matter.

Samples

A total of 40 samples were collected from Site 819 at 10-m intervals over a depth that ranged from 7 to 398 mbsf. All sediments were analyzed (1) for their composition of light hydrocarbons (C_1–C_6) using headspace analyses and (2) for total nitrogen, sulfur, and carbon using an NA 1500 Carlo Erba NCS analyzer.

Volatile Hydrocarbons

Hydrocarbon gases (C_1–C_6) in sediments were analyzed as part of ODP's safety and pollution-prevention monitoring program, using the headspace technique, the vacutainer technique (when gas pockets were observed in the core liner), the Carle gas chromatograph (for determination of C_1-C_3 concentrations), and the NGA gas chromatograph (mainly for determination of C_4-C_6 concentrations). The results of 40 headspace analyses and of 16 vacutainer analyses from Site 819 are presented in Table 7. Figure 22 shows the WSTP-temperature data from Site 817 and the geothermal gradient used at Site 819 for interpreting the depth-related evolution of the C_1/C_2 ratio.

Sediments at Site 819 contained high concentrations of methane, which represented no safety and/or pollution hazards. With the exception of anomalous data from three samples at 90, 247, and 300 mbsf (Figs. 23 and 24), the evolution of the C_1/C_2 ratio with increasing depth and temperature did not show any anomalous trend. The C_1/C_2 values from headspace analyses ranged between 10,000 and 2,000.

Headspace gas concentrations of methane were low (3 ppm, in Sample 133-819A-1H-5, 145-146 cm) in the sulfate reduction zone, but increased rapidly below 25 mbsf (57,000 ppm at 35 mbsf, in Sample 133-819A-4H-5, 145–146 cm). Methane was the main component below this depth. Ethane concentrations did not exceed 10 ppm. Propane appeared at 223 mbsf. Below 250 mbsf, the propane concentrations exceeded ethane (C_2/C_3 ratio < 1) and increased to 22 ppm at 398 mbsf (Sample 133-819A-44X-7, 0–2 cm). Significant total pentane concentrations (17 ppm) were recognized at 378 mbsf (Sample 133-819A-42X-5, 148–150 cm).

The observed coincidence between low sulfate concentrations and high amounts of methane (> 1000 ppm) and a trace amount of ethane in the sediments suggests a bacterial origin of methane (and ethane?) in the sulfate-free section (between 25 and 225 mbsf) of the sediments at Site 819 (Fig. 25). Below 250 mbsf, two factors indicate the beginning of a mixing with thermogenic free-hydrocarbons, although the source may be deeper in the section:

1. The appearance of propane, the progressive increase of propane content, and the decrease of both the C_2/C_3 and $C_1/(C_2+C_3)$ ratios at very shallow depths and low temperature values (Figs. 24 and 25).

2. The strong decrease of both C_1 content, C_1/C_2 and $C_1/(C_2+C_3)$ ratios at a depth of 295 to 300 mbsf together with a strong decrease in porosity (see "Physical Properties" section, this chapter) of the lithified dolomitic wackestones observed at the bottom of Unit III (see also "Lithostratigraphy" section, Fig. 10, this chapter). Below this cap of reduced porosity sediments, the contents of methane, ethane, and propane increased (Fig. 24), and both isopentanes and normal pentanes were detected.

Organic Carbon Contents

Total organic carbon (TOC) and total inorganic carbon (TIC) contents together with total nitrogen and sulfur concentrations recorded in Site 819 are presented in Table 8. The amount of organic carbon at Site 819 was low and did not exceed 0.7% TOC (Fig. 26). We observed a decrease of TOC values (between 0.65% and 0.35%) in the first 13 m (clayey ooze of Unit I) that corresponded to the sulfate reduction zone. Below this depth, we observed a progressive and cyclical increase of TOC values (average values between 0.3% in the clayey bioclastic and silty oozes of Unit II, 0.4%–0.45% in the wackestones and oozes of Unit III, and 0.45–0.5% in the chalks of Unit IV).

Total sulfur concentrations in sediments were below detection limits of the NCS analyzer, except in Sample 133-819-38X-6, 0–2 cm.

Total nitrogen concentrations in sediments increased progressively with depth (Fig. 26) and followed the trend of organic carbon. Values ranged between 0.10% in Unit I and 0.20% in Units III and IV.

On the basis of TOC/nitrogen ratios (Fig. 26), marine organic matter is abundant in all lithologies encountered at Site 819: no terrestrial influxes of organic material were observed. As a consequence of low organic contents, we were unable to conduct detailed geochemical characterization of kerogen types using the Rock-Eval pyearolysis method as originally planned. More detailed shore-based studies (elemental analysis and optical investigations of extracted kerogens) will permit characterization of short-term fluctuations in vertical distribution and preservation of different components of organic matter in sediments encountered at Site 819.

PHYSICAL PROPERTIES

Physical properties analyzed in cores from this site include bulk density, *P*-wave velocity, and magnetic susceptibility on unsplit cores and *P*-wave velocity, electrical-resistivity formation factor, shear strength, and index properties (including bulk density, grain density, water content, porosity, and void ratio) of split cores. The methods used are described in detail in the "Explanatory Notes" chapter (this volume).

Bulk Density

Bulk densities for Site 819 were determined from volume and mass measurements of discrete core samples and from absorption of gamma rays by whole-round cores (Figs. 27 and 28; Table 9). Figures 27A through 27C illustrates the similarity of bulk density determinations using different methods. Values determined from measurements of split core samples have a mean value approximately that of the wireline log bulk densities (2.0 g/cm^3), whereas values determined from GRAPE measurements of whole-round cores are lower (1.9 g/cm^3) because of the presence of gas in these cores. Much of the fine structure of the density profiles determined by different methods can be correlated across various profiles, although this correlation is not perfect. The level of correlation is limited by a number of factors, including (1) low spatial sampling of split cores, (2) hole irregularities that dramatically affect wireline measurements, and (3) presence of gas that

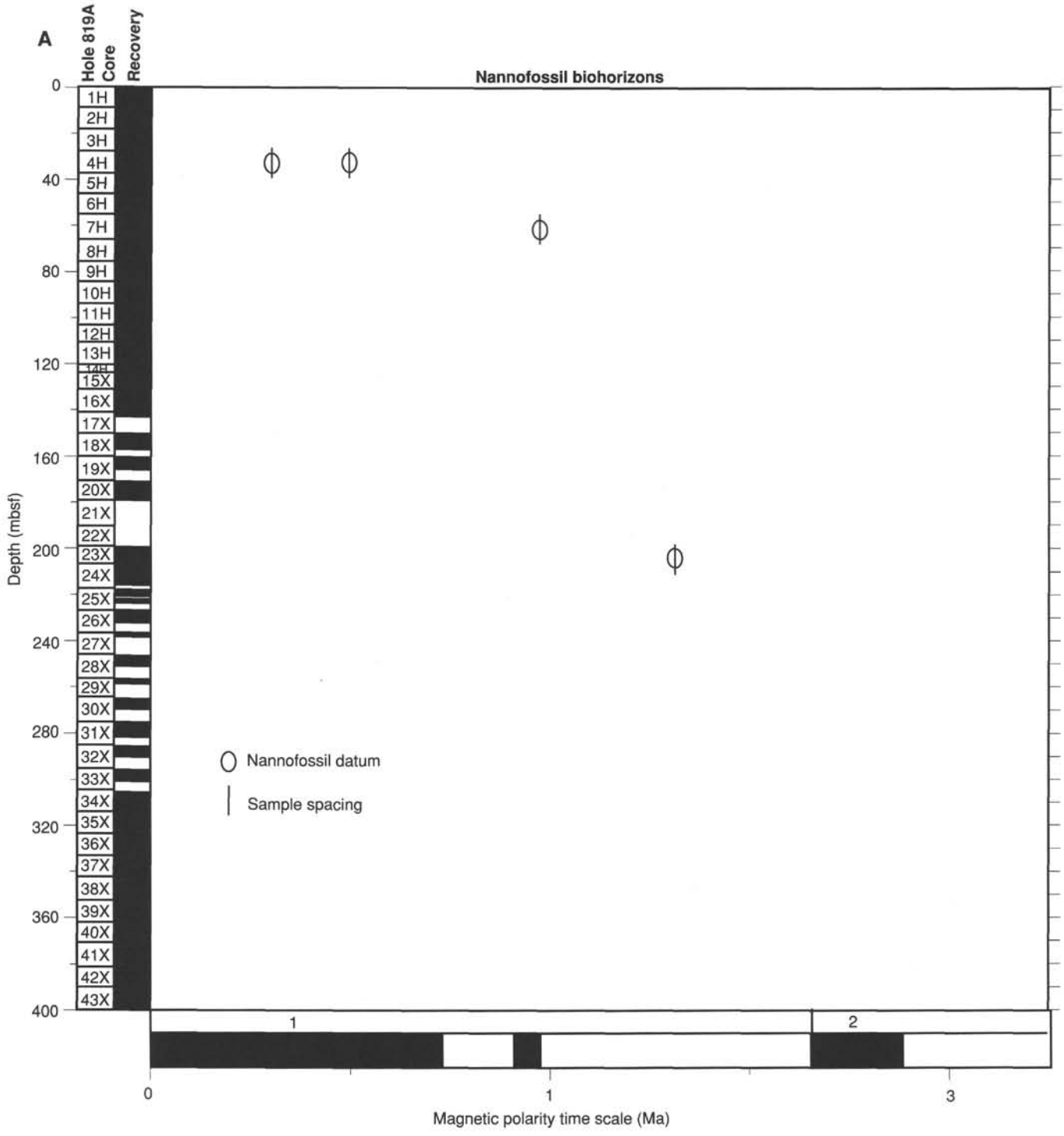

Figure 15. Plots of age vs. depth. **A.** Site 819. **B.** Site 820. **C.** Site 821.

affects the GRAPE and split core measurements. In Figure 29A, we compare density to water content data.

P-Wave Velocity

P-wave velocities were measured in whole-round cores using the MST and in discrete core samples using the Hamilton Frame (Table 10 and Fig. 28). The presence of gas limited our ability to measure velocities with either the Hamilton frame or the MST below 40 mbsf. The section is characterized by a decrease in both velocity and density in the uppermost 5 mbsf, followed by a sharp increase between 5 and 8 mbsf. In the upper 40 m of the hole, bulk density varies with carbonate content. It is not immediately clear why velocity should vary with density because one would expect an inverse relationship of the form $V = SQRT(K/BD)$, where V is velocity, K is modulus of compressibility, and BD is bulk density. Apparently, the material that substitutes for carbonate as the proportion of carbonate decreases has a much lower K value than carbonate so that a decrease in density is offset by a decrease in K.

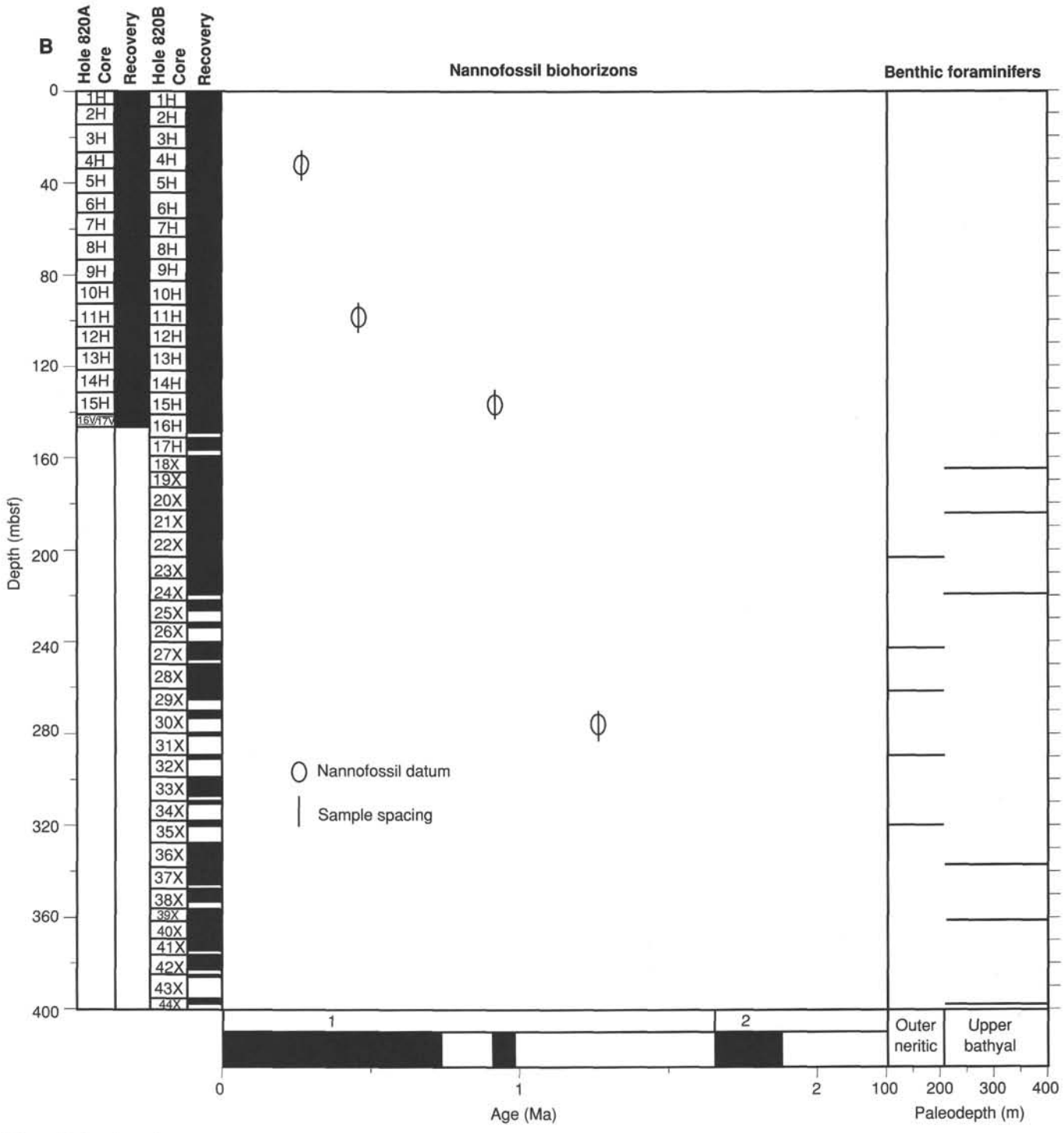

Figure 15 (continued).

Porosity and Water Content

Porosity was one of the index properties determined from discrete core samples using mass balance and the pycnometer (Table 9) as well as from wireline logs. Variations of porosity with depth and with carbonate content are shown in Figures 27, 29B, 30, 31, and 32. Similarly, dry-water content (derived from the same set of index property measurements) is plotted in Figure 27. We also show in Fig. 29A water content plotted vs. density and a curve that shows the relationship between dry-water content and bulk density for a two-component system having varying water content and a grain density of 2.76 g/cm^3, while water density is 1.0 g/cm^3. Our observed data parallel this expected relationship, but are offset slightly, probably because we neglected the salt content of water when calculating this curve. Figure 29A does show that most variation in bulk density of the sediments at Site 819 can be explained by variations in a

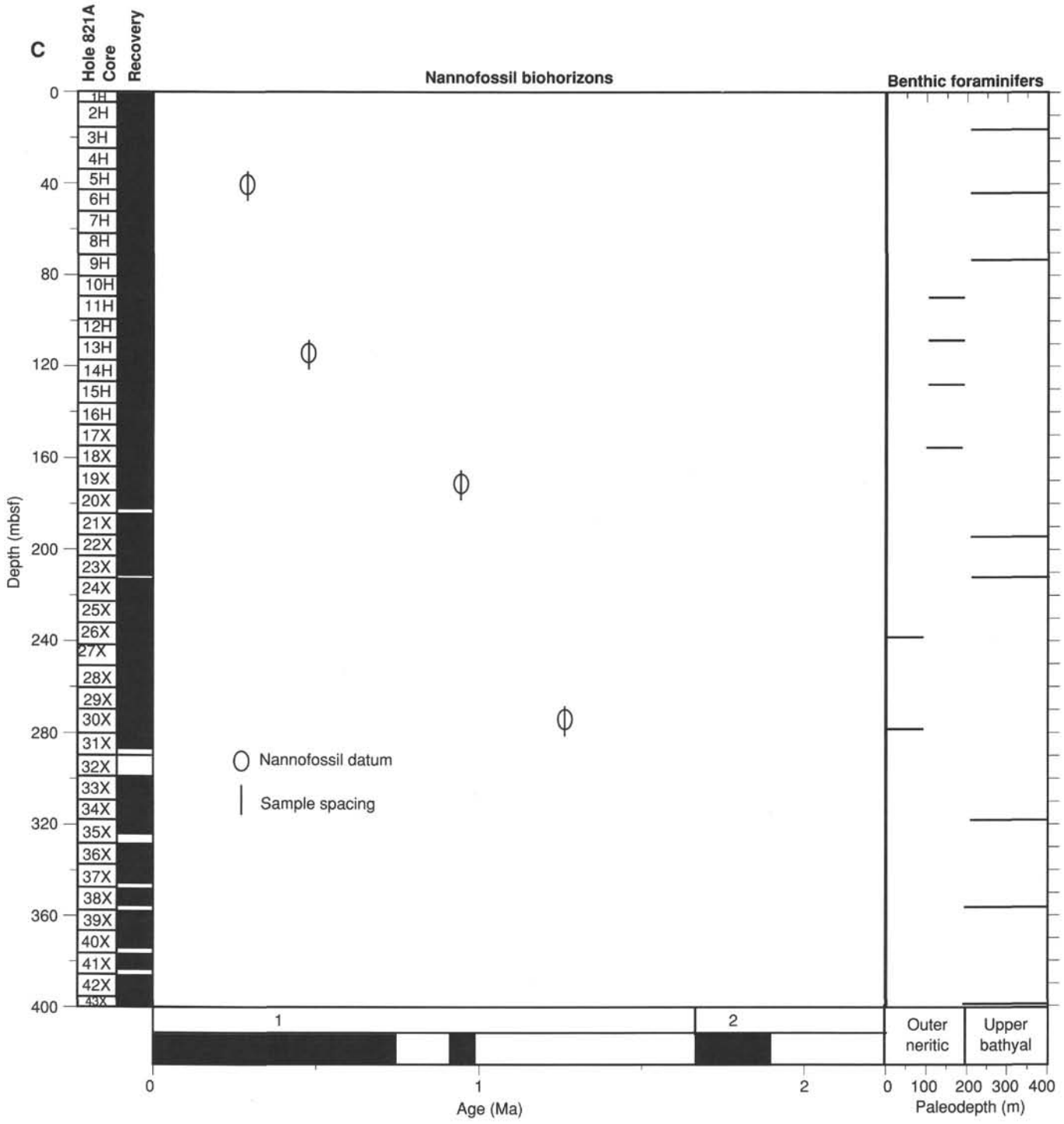

Figure 15 (continued).

two-component system of water and grains having a constant grain density.

Figure 30 suggests an inverse relationship between porosity and weight percent carbonate in some parts of the section at Site 819; this relationship is generally applicable to this site, as indicated by Figure 29B, which shows no correlation between weight percent carbonate and porosity.

The comparison of porosity at Site 819 with porosities from Sites 815 and 817 shows that Site 819 porosity is characterized by a sharp decrease in porosity in the uppermost 50 mbsf, with a leveling off, at least in the local mean, below 250 mbsf (Fig. 31).

Comparison of Site 819 data with published curves of porosity vs. depth shows that Site 819 has a precipitous

Table 3. Biostratigraphic datums from Sites 819, 820, and 821.

Datum	Age (Ma)	Core, section, interval (cm)	Depth (mbsf)	Mean depth (mbsf)	Thickness (m)	Time interval (m.y.)	Rate (cm/k.y.)
Site 819							
Emiliania huxleyi	0.275	3H-5, 150	26–35.5	30.7	30.7	0.275	11.2
Pseudoemiliania lacunosa	0.465	4H-5, 150	26–35.5	30.7	0	0.19	0
small *Gephyrocapsa* Acme	0.93	7H-5, 150	54.5–62.5	58.5	27.8	0.465	6.0
Helicosphaera sellii	1.27	23X-CC	198.1–207.4	202.7	144.2	0.34	42.4
Site 820							
Emiliania huxleyi	0.275	3H-CC	26.2–35.7	31	31	0.275	11.3
Pseudoemiliania lacunosa	0.465	11H-CC	92.7–102.2	97.5	66.5	0.19	35
small *Gephyrocapsa* Acme	0.93	15X-CC	130.7–140.2	135.5	38	0.465	8.2
Helicosphaera sellii	1.27	30X-CC	270.4–280.1	275.3	139.8	0.34	41.1
Site 821							
Emiliania huxleyi	0.275	4H-CC	23.4–32.9	28.2	28.2	0.275	10.3
Pseudoemiliania lacunosa	0.465	14H-CC	118.4–127.9	123.2	93.5	0.19	49.2
small *Gephyrocapsa* Acme	0.93	20X-CC	174.9–184.6	179.7	56.5	0.465	12.2
Helicosphaera sellii	1.27	30X-CC	270.8–280.4	275.6	95.9	0.34	28.2

decline in porosity in the uppermost 50 mbsf, compared to other regions. By 400 mbsf, however, Site 819 porosities approximate those of other regions.

Electrical-Resistivity Formation Factor

We measured the formation factor at three intervals in sections from Hole 819A (see Table 11 and Fig. 27G). The formation factor measured using split cores shows some correlation in fine structure as well as average amplitude to the formation factor, which was measured with the wireline log. The formation factor measured using split cores increases in the upper 200 mbsf of the section and then follows a decreasing trend to the bottom of the hole. The wireline log records the same gradual increase in the upper 200 mbsf. In contrast to the split core measurements, the wireline formation factor remains high to the bottom of the hole.

The formation factor is measured as a proxy for porosity and as such should be highly negatively correlated with porosity, (i.e., porosity and formation factor should be inversely proportional). Figure 27 indicates significant correlation between the different formation factor logs and the separate measures of porosity; however, some exceptions do exist.

Shear Strength

We measured shear strength in the upper section of this hole down to a depth at which the sediment became too friable and cracked, rather than sheared, while measuring vane shear (Table 12 and Fig. 30).

DOWNHOLE MEASUREMENTS

Reliability of Logs

Hole size is the most important control of accuracy of the logs from Hole 819A. Only one caliper log was obtained: an apparent caliper log (Fig. 33) that was calculated from the sonic log (see "Explanatory Notes" chapter, this volume). The lithodensity tool caliper normally is much more accurate than the sonic caliper, but this tool was not operational at this site. Based on correlation of the largest sonic caliper values with anomalously low density values (Fig. 33), we concluded that scattered portions of the lithodensity run were unreliable

Table 4. Interstitial water analyses for Site 819.

Core, section, interval (cm)	Depth (mbsf)	pH	Alkalinity (mM)	Salinity (g/kg)	Cl^- (mM)	Mg^{2+} (mM)	Ca^{2+} (mM)	SO_4^{2-} (mM)	NH_4^- (μM)	Si (μM)	K^+ (mM)	Sr^{2+} (μM)	Na^+ (mM)
Seawater		8.27	2.655	35.5	550.70	53.68	10.36	29.74	0	3	10.62	98	473.93
1H-5, 145–150	5.95	7.21	9.584	34.2	550.70	48.54	6.26	18.11	904	275	12.30	80	473.53
2H-5, 145–150	15.95	7.31	10.926	32.5	549.72	39.39	4.16	6.97	1434	336	10.08	95	475.80
3H-5, 145–150	25.45	7.43	11.059	31.8	547.76	30.63	3.32	0.00	1809	135	10.55	112	478.33
4H-5, 145–150	34.95	7.33	9.500	31.8	549.72	25.42	4.95	0.00	2161	236	9.33	179	486.62
5H-5, 145–150	44.45	7.53	8.388	31.6	545.80	23.32	4.60	0.00	2572	214	9.02	234	486.28
6H-5, 145–150	53.95	7.40	7.652	30.5	541.88	19.79	4.35	0.00	2845	230	8.22	273	489.65
7H-5, 140–150	63.45	7.81	6.811	30.5	547.76	18.43	3.11	0.00	3346	208	8.13	242	499.54
8H-5, 145–150	72.90	7.68	7.936	31.0	535.02	16.83	3.45	0.00	3304	155	7.18	221	491.47
9H-5, 140–150	82.40	7.53	8.341	31.0	540.90	16.05	3.41	0.00	3563	208	7.02	241	499.25
10H-5, 140–150	91.90	7.84	8.985	31.0	538.94	15.26	2.86	0.00	3762	149	6.79	231	500.68
13H-5, 140–150	118.40	7.88	9.988	30.2	547.76	13.89	2.97	0.00	3629	177	5.64	292	514.18
16H-6, 140–150	137.80	7.88	10.288	31.5	548.74	16.35	3.41	2.66	4021	200	6.21	344	513.91
19X-2, 140–150	168.80	7.58	11.879	30.5	538.94	17.68	3.86	2.47	4214	206	5.41	483	502.10
23X-5, 140–150	205.50	7.71	12.423	31.0	536.98	18.61	4.42	1.27	3769	210	4.82	260	496.77
25X-1, 140–150	224.40	7.51	11.559	31.0	543.84	19.27	4.81	1.95	4116	250	4.99	252	501.53
28X-1, 140–150	243.40	7.67	10.122	31.0	540.90	25.37	5.81	6.23	4152	212	5.15	171	491.48
31X-2, 140–150	272.30	7.58	9.691	31.0	535.02	18.31	4.35	1.06	4228	165	3.91	155	493.06
34X-2, 140–150	301.30			31.0	534.04	22.07	5.50	3.06	2743	250	3.62	277	478.12
37X-5, 140–150	330.30	7.72	9.745	31.0	543.84	17.69	4.63	0.34	3727	226	3.43	174	502.12
40X-6, 140–150	358.90	7.68	7.819	31.5	549.72	22.08	5.83	7.13	3731	232	3.34	176	508.57
43X-5, 140–150	387.80	7.80	7.528	31.0	540.90	16.51	4.95	0.39	3450	181	3.02	206	499.41

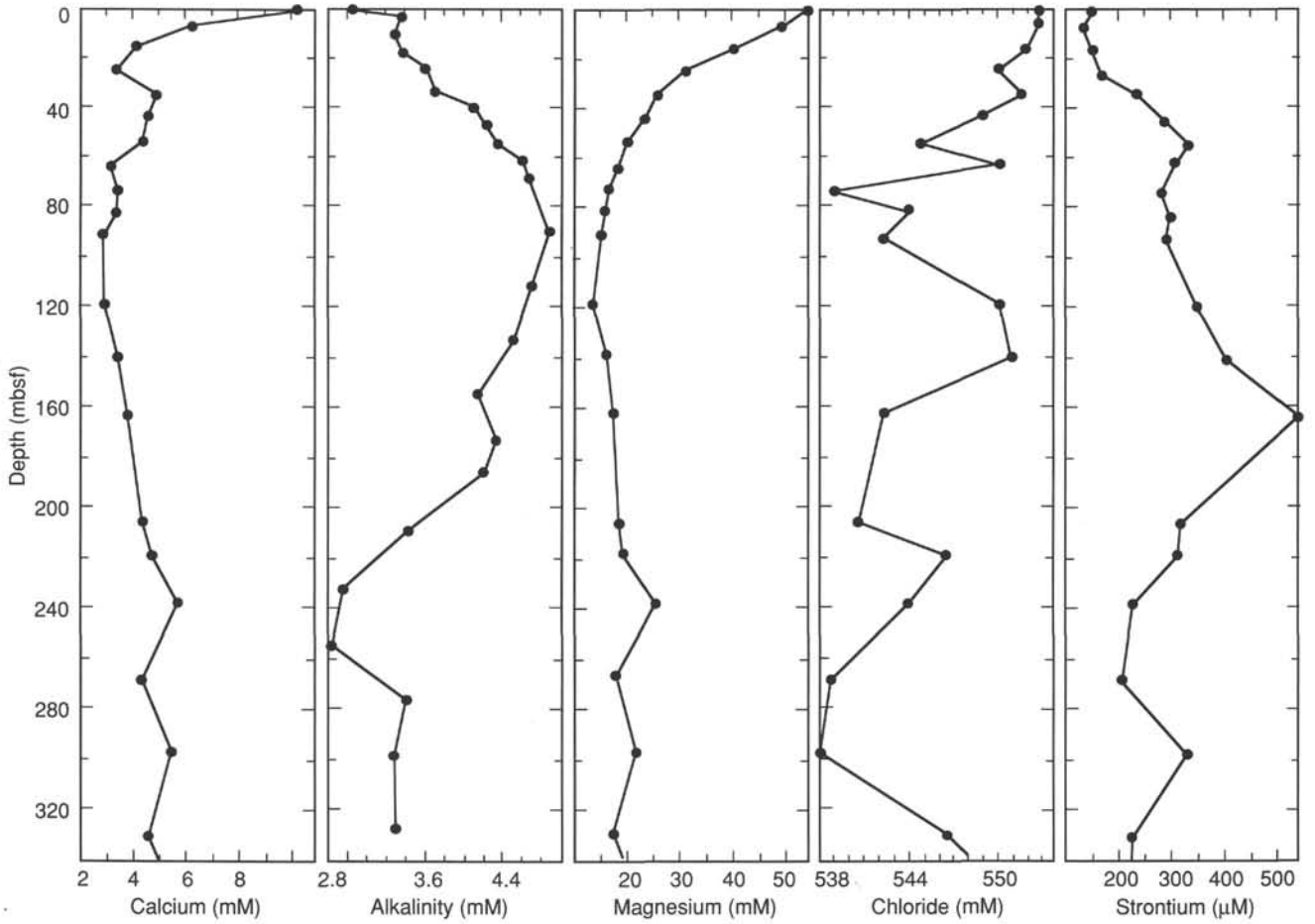

Figure 16. Concentrations of Ca^{2+}, alkalinity, Mg^{2+}, Cl^-, and Sr^{2+} for Site 819.

because of insufficient pad contact with the borehole wall; this conclusion implies that porosity and Archie component *m* (1942) calculations will be in error in these zones (Fig. 34). Post-cruise processing will use these petrophysical parameters and the velocity log to produce a "best estimate" of density in these zones having poor pad contact, which probably were caused by washout of less cohesive, weaker material. Most other logs do not require pad contact and thus were relatively insensitive to changes in borehole size. Two minor exceptions were the gamma-ray and resistivity logs, which probably will change slightly during post-cruise borehole correction.

As is often the case with ODP holes, the initial sonic logs from Hole 819A exhibited a few zones in which cycle-skipping caused unreliable swings in apparent velocity. Reprocessing (see "Explanatory Notes" chapter, this volume) appears to have removed all unreliable data, and we consider the reprocessed log in Figure 33 to be of very good quality. For the short interval of 366.7 to 382.4 mbsf at the bottom of the hole, resistivity logs (but not sonic logs) are available because the resistivity tool was much lower on the tool string. A pseudo-sonic log was generated and used in Figures 33 and 35 for this interval, based on regression of sonic transit time on a logarithm of shallow resistivity for the overlying interval of 292.2 to 366.6 mbsf ($R = -0.90$).

The spectral gamma-ray tool is the only tool in the seismic stratigraphic combination that can provide useful formation data even through pipe. At Hole 819A, through-pipe spectral gamma-ray logs were obtained for the interval of 0 to 69.6 mbsf. In this interval, the high clay content resulted in values for uranium and potassium that are well above the resolving power of the tool, and values for thorium that are near the resolving power of the tool. However, we have not yet corrected for pipe size in these logs.

Relationships Among Velocity, Resistivity, and Density

Velocity, resistivity, and density strongly correlate throughout almost all of the logged interval at Hole 819A (Fig. 33). Furthermore, these three logs are moderately well correlated with the gamma-ray log (SGR in Fig. 36), while gamma-ray maxima correspond to velocity, resistivity, and density minima. This pattern of clay-mineral variation is typical in ODP holes. Higher clay-mineral concentration is evident by higher gamma-ray counts, particularly when illite (3%–8% potassium; Serra, 1986) is a significant constituent of the clays, while clay minerals substantially increase the porosity of uncompacted (<2 km overburden) sediments. Spectral gamma-ray values are substantially higher than those at previous sites of Leg 133. Potassium values in particular increased by more than a factor of 10, to values ranging from 0.5% to 1.0%. Thorium increases by a factor of three, while the total SGR count is nearly double that at Site 817 (see "Site 817" chapter, this volume), with values ranging from 30 to 50 API units.

These changes in velocity and density with depth (Fig. 33) generally follow a gradual compaction profile, suggesting that mechanical compaction is dominant over diagenesis for controlling porosity at this site. Similar patterns were observed at Sites 814 and 817 (see "Site 814" and "Site 817" chapters, this volume). Velocity and density values within the open-hole

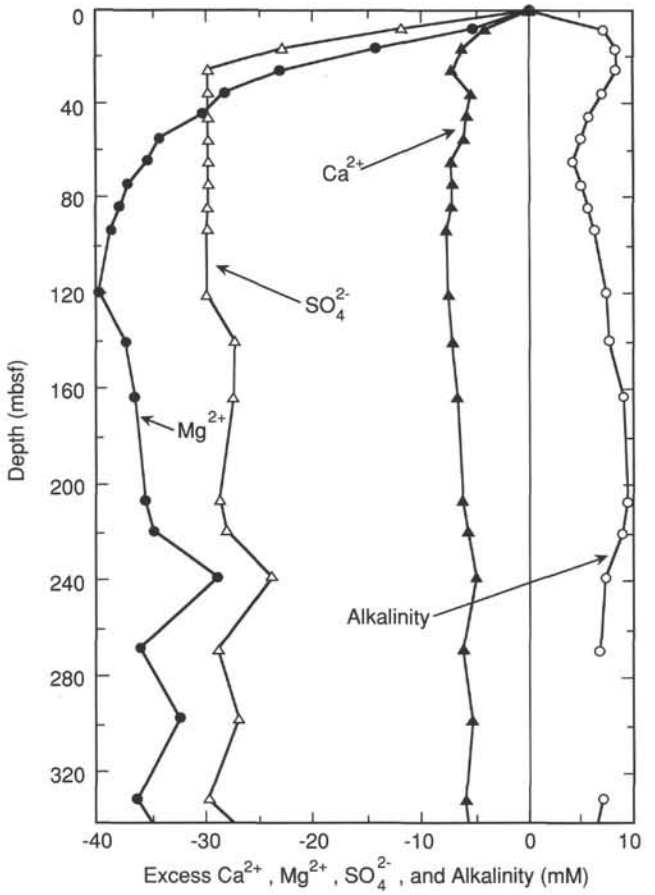

Figure 17. Changes in the concentration of SO_4^{2-}, alkalinity, Ca^{2+} and Mg^{2+} relative to seawater Ca^{2+}/Cl^- ratios as a function of depth, Site 819.

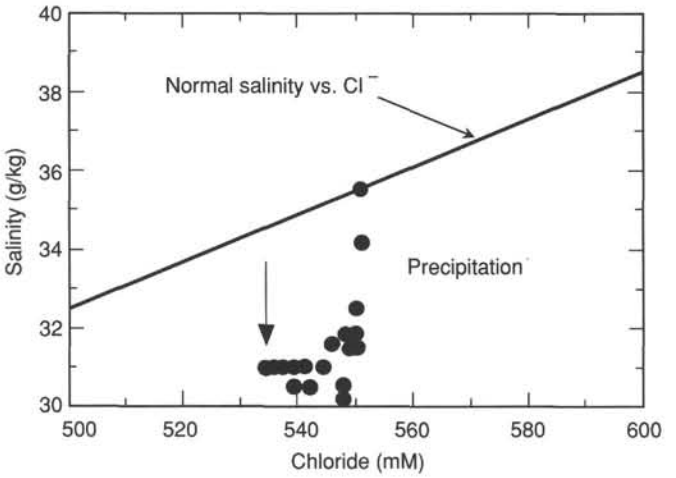

Figure 18. Relationship between Cl^- and salinity for Site 819. Note the deficit of Cl^- relative to the normal salinity vs. Cl^- trend.

logged interval are somewhat greater than those normally observed in terrigenous or calcareous sediments of comparable depths. Average velocity increases from 1.65 to 1.7 km/s at 80 mbsf, to 2.0 to 2.1 km/s at 380 mbsf, compared with typical values for these depths of 1.55 to 1.60 and 1.9 to 1.95 km/s (Hamilton, 1979). Similarly, density increases from 1.9 g/cm^3 at 80 mbsf to about 2.0 to 2.1 g/cm^3 at 380 mbsf, compared

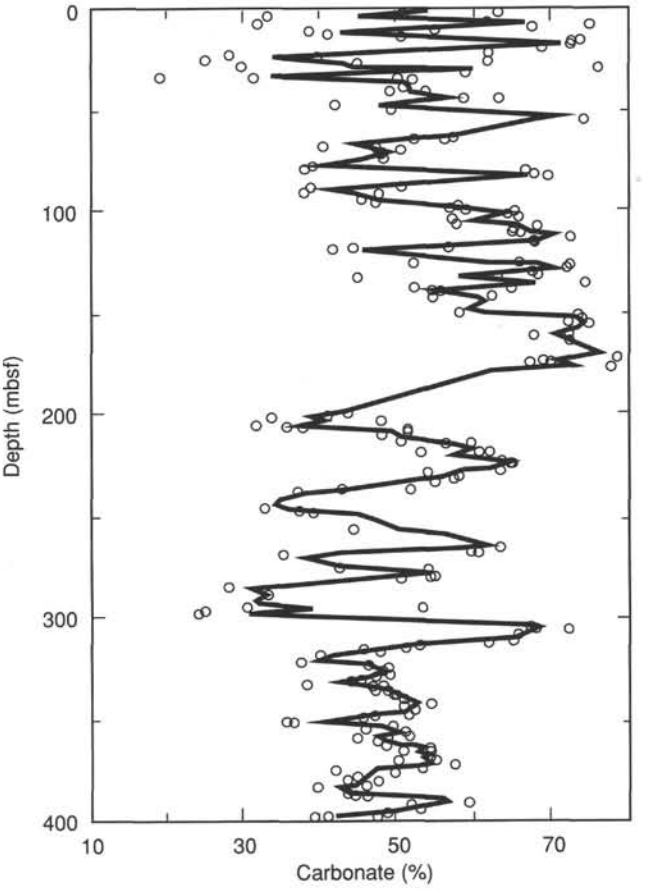

Figure 19. Changes in concentration of carbonate as a function of depth for Site 819. Data have been interpolated to a common sampling interval of 1 m and smoothed using a weighted five-point average.

with typical values for these depths of about 1.64 and 1.98 g/cm^3 (Hamilton, 1976).

The density log exhibits a half dozen intervals that may have been affected by poor pad contact. The loss of mechanical caliper data degrades the usefulness of these data still further. Consequently, petrophysically derived parameters, such as the "Archie *m* component" used to assess changes in pore morphology, are not reliable enough for interpreting lithology. For example, the interval between 282 and 300 mbsf has lower-than-average velocity and resistivity, but its densities may be too low because of poor pad contact. The Archie *m* component (Fig. 34) indicates increases that might indicate thin layers having different pore morphology, such as a change in grain shape that would accompany abundant clay minerals. The spectral gamma-ray logs (Fig. 36) do not confirm the presence of alternating layers of high and low clay contents. Thus, we think it unlikely that we will be able to use log-derived pore morphology indicators as aids for analyzing lithology, as was done at Site 817 (see "Site 817" chapter, this volume). The log "*A*/*B*," a normalized ratio of velocity to resistivity, is relatively insensitive to variations in hole size and exhibits little variation at this site (Fig. 37).

The abundance of thorium seen in Figure 36 is of a cyclic nature; this cyclicity will be analyzed post-cruise, as no immediately obvious correlations exist between these cycles and the other logs. The potassium log exhibits a variable style, with values in the range of 0.5% to 1% and with some peaks that

Table 5. Carbonate content data for Site 819.

Core, section, interval (cm)	Depth (mbsf)	Carbonate (%)
133-819A-		
1H-1, 102–104	1.02	63.20
1H-2, 102–104	2.52	51.60
1H-3, 102–104	4.02	33.00
1H-4, 102–104	5.52	61.80
1H-5, 102–104	7.02	75.30
1H-5, 145–146	7.45	31.80
1H-6, 62–64	8.12	67.30
2H-1, 102–104	9.52	54.80
2H-2, 102–104	11.02	38.30
2H-3, 102–104	12.52	41.00
2H-4, 102–104	14.02	50.50
2H-5, 102–104	15.52	73.90
2H-5, 145–146	15.95	72.80
2H-6, 102–104	17.02	72.70
3H-1, 102–104	19.02	68.80
3H-2, 102–104	20.52	61.80
3H-3, 102–104	22.02	40.20
3H-4, 102–104	23.52	28.10
3H-5, 81–84	24.81	24.90
3H-5, 145–146	25.45	61.70
3H-6, 102–104	26.52	44.60
4H-1, 101–104	28.51	29.80
4H-2, 70–73	29.70	76.20
4H-3, 101–104	31.51	58.70
4H-4, 101–104	33.01	19.10
4H-5, 101–104	34.51	31.20
4H-5, 145–146	34.95	50.00
4H-6, 101–104	36.01	51.80
5H-1, 102–105	38.02	50.90
5H-2, 106–109	39.56	53.70
5H-3, 76–79	40.76	49.00
5H-4, 105–108	42.55	53.70
5H-5, 103–106	44.03	58.90
5H-5, 145–146	44.45	63.20
5H-6, 110–113	45.60	52.90
6H-1, 101–103	47.51	41.90
6H-2, 101–103	49.01	49.10
6H-3, 97–100	50.47	64.70
6H-4, 89–92	51.89	67.60
6H-5, 145–146	53.95	74.30
6H-6, 52–53	54.52	67.60
7H-5, 66–69	62.66	57.10
7H-5, 145–146	63.45	56.00
7H-6, 102–105	64.52	52.00
8H-2, 102–105	67.14	40.20
8H-3, 74–77	68.36	47.40
8H-4, 82–85	69.94	50.50
8H-5, 6–9	70.68	47.80
8H-5, 145–146	72.07	47.60
8H-6, 101–104	73.13	48.20
8H-7, 101–104	74.63	43.80
9H-2, 80–83	76.15	42.70
9H-3, 80–83	77.65	38.90
9H-4, 80–83	79.15	38.00
9H-5, 83–86	80.68	66.80
9H-5, 145–146	81.30	67.60
9H-6, 83–86	82.18	69.70
9H-7, 83–86	83.68	66.60
10H-2, 100–103	85.90	56.80
10H-3, 100–103	87.40	50.40
10H-4, 100–103	88.90	38.50
10H-5, 100–103	90.40	37.80
10H-5, 145–146	90.85	44.70
10H-6, 100–103	91.90	47.60
10H-7, 100–103	93.40	45.30
11H-2, 60–62	94.92	47.20
11H-3, 60–62	96.42	57.60
11H-4, 60–62	97.92	56.90
11H-5, 60–62	99.42	58.70
11H-5, 145–146	100.27	65.40
11H-6, 60–62	100.92	64.60
11H-7, 60–62	102.42	66.00
12H-1, 24–26	103.74	57.10
12H-2, 24–26	105.24	57.50
12H-3, 3–7	106.53	68.10
12H-4, 24–26	108.24	65.30
12H-4, 149–150	109.49	65.90
12H-5, 24–26	109.74	65.00
13H-2, 57–60	112.15	72.60
13H-3, 57–60	113.65	67.50
13H-4, 61–63	115.19	67.60
13H-5, 41–43	116.49	56.40
13H-5, 145–146	117.53	44.40
13H-6, 41–43	117.99	41.70
14H-1, 97–100	121.47	51.10
15H-1, 21–24	123.21	58.80
15H-2, 20–23	124.70	66.00
14H-3, 140–141	124.90	52.00
15H-3, 7–10	126.07	72.40
15H-4, 26–29	127.76	72.00
15H-5, 17–20	129.17	67.40
16H-1, 10–13	130.50	68.00
16H-2, 11–14	131.10	63.00
16H-3, 12–15	132.61	44.90
16H-4, 25–28	134.24	74.50
16H-5, 140–143	136.89	64.80
16H-6, 51–54	137.50	52.20
16H-6, 149–150	138.48	55.60
16H-7, 73–76	139.22	54.60
17H-1, 149–150	141.59	54.70
17H-2, 17–20	141.77	62.40
18H-1, 40–43	150.10	58.10
18H-2, 40–43	151.60	73.60
18H-3, 40–43	153.10	73.80
18H-3, 149–150	154.19	72.20
18H-4, 40–43	154.60	75.10
19H-1, 40–43	159.80	72.10
19H-2, 40–43	161.30	67.60
19H-3, 40–43	162.80	72.20
20H-1, 100–103	170.10	76.10
20H-2, 100–103	171.60	78.50
20H-3, 100–103	173.10	69.10
20H-4, 0–2	173.60	70.00
20H-4, 100–103	174.60	67.20
20H-5, 100–103	176.10	77.90
20H-6, 100–103	177.60	67.30
21H-0, 2–	178.89	61.90
23H-1, 70–73	198.80	43.40
23H-2, 70–73	200.30	40.30
23H-3, 70–73	201.80	33.60
23H-4, 70–73	203.30	47.70
23H-5, 70–73	204.80	31.70
23H-5, 140–142	205.50	37.80
23H-6, 70–73	206.30	35.80
24H-1, 70–73	208.10	51.40
24H-2, 70–73	209.60	51.40
24H-3, 70–73	211.10	47.70
24H-4, 70–73	212.60	50.60
24H-4, 149–150	213.39	59.60
24H-5, 70–73	214.10	56.50
25H-1, 71–73	217.71	61.90
25H-1, 140–142	218.40	60.50
25H-2, 72–73	219.22	53.10
26H-1, 70–73	222.40	63.10
26H-2, 0–2	223.20	64.40
26H-2, 70–73	223.90	64.70
27H-1, 70–73	227.00	63.20
27H-2, 70–73	228.50	53.80
27H-3, 70–73	230.00	57.80
27H-3, 149–150	230.79	57.00
27H-4, 70–73	231.50	54.80
28H-1, 70–73	236.70	42.50
28H-1, 140–141	237.40	51.80
28H-2, 60–63	238.10	37.00
29H-1, 70–73	246.30	32.80
29H-1, 149–150	247.09	37.00
29H-2, 70–73	247.80	39.00
29H-3, 70–73	249.30	44.90
29H-4, 70–73	250.80	45.70
30H-1, 70–73	256.00	50.10
30H-2, 0–1	256.80	44.Z20
30H-2, 70–73	257.50	53.10
31H-1, 70–73	265.60	63.30
31H-2, 70–73	267.10	59.10
31H-2, 140–141	267.80	60.10
31H-3, 70–73	268.60	35.20
32H-1, 72–74	275.22	42.30
32H-2, 72–74	276.72	53.90
32H-3, 65–67	278.15	52.10
32H-3, 149–150	278.99	54.10
32H-4, 87–89	279.87	54.60
32H-5, 75–76	281.25	50.40
33H-1, 80–82	285.00	28.10
33H-2, 80–82	286.50	31.60
33H-3, 80–82	288.00	33.20
34H-1, 67–68	294.57	30.40
34H-2, 70–71	296.10	53.20
34H-2, 140–141	296.80	24.80
34H-3, 86–87	297.76	24.30
35H-1, 80–81	304.30	67.10
35H-2, 0–1	305.00	67.60
35H-2, 80–81	305.80	72.10
35H-3, 80–81	307.30	65.40
35H-4, 80–81	308.80	65.60
35H-5, 80–81	310.30	64.90
35H-6, 80–81	311.80	61.70
36H-1, 15–16	313.35	52.70
36H-2, 38–39	314.57	51.20
36H-3, 0–1	315.69	45.50
36H-3, 37–38	316.06	47.30
36H-4, 21–22	317.40	47.70
36H-5, 22–23	318.91	39.90
36H-6, 33–34	320.52	40.60
36H-7, 38–39	322.07	37.30
37H-1, 27–28	323.17	46.20
37H-2, 40–41	324.80	48.70
37H-3, 40–41	326.30	47.80
37H-4, 40–41	327.80	48.70
37H-5, 40–41	329.30	47.00
37H-5, 149–150	330.39	43.70
37H-6, 40–41	330.80	45.00
38H-1, 26–27	332.76	38.20
38H-2, 16–17	333.80	48.20
38H-3, 17–18	335.31	47.00
38H-4, 25–26	336.89	48.90
38H-5, 25–26	338.39	49.60
38H-6, 0–2	339.64	49.30
38H-6, 24–25	339.88	50.20
38H-7, 24–25	341.38	51.60
39H-1, 42–43	342.62	54.50
39H-2, 42–43	344.12	50.60
39H-3, 42–43	345.62	52.10
39H-4, 39–40	347.09	51.30
39H-5, 0–2	348.20	47.00
39H-5, 22–23	348.42	46.90
39H-6, 38–39	350.08	45.60
40H-1, 17–18	351.67	35.60
40H-2, 24–25	352.14	36.60
40H-3, 26–27	353.66	49.40
40H-4, 23–24	355.13	45.80
40H-5, 22–23	356.62	51.00
40H-6, 37–38	358.27	51.40
40H-6, 140–142	359.30	49.00
40H-7, 14–15	359.54	44.90
41H-1, 8–10	361.18	47.50
41H-2, 8–10	362.13	48.40
41H-3, 8–10	363.63	54.10
41H-4, 8–10	365.13	54.00
41H-4, 149–150	366.54	50.50
41H-5, 8–10	366.63	50.50
41H-6, 8–10	368.13	54.10
41H-7, 8–10	369.63	54.80
42H-1, 8–10	370.88	49.90
42H-2, 8–10	372.38	57.40
42H-3, 8–10	373.88	53.10
42H-4, 18–20	375.48	41.90
42H-5, 18–20	376.98	49.50
42H-5, 148–150	378.28	46.90
42H-6, 21–23	378.51	44.40
43H-1, 10–12	380.50	43.50
43H-2, 10–12	380.80	47.50
43H-3, 10–12	382.30	45.80
43H-4, 10–12	383.80	39.50
43H-5, 10–12	385.30	43.50
43H-5, 140–142	386.60	44.40
43H-6, 10–12	386.80	46.00
44H-2, 91–93	391.04	59.20
44H-3, 91–93	392.54	51.70
44H-4, 91–93	394.04	53.00
44H-5, 91–93	395.54	48.40
44H-6, 91–93	397.04	47.40
44H-7, 0–2	397.63	41.00
44H-7, 91–93	398.54	39.20

correlate with low resistivity and velocity anomalies, the most notable of which are at 162 and 272 mbsf and correlate with the start of the log-based subunits described below.

The velocity log was converted to an integrated traveltime log (Fig. 35) to facilitate depth-to-time conversion for comparison of Site 819 data with seismic facies. For the unlogged interval between the seafloor and 66.6 mbsf, we used a simple linear interpolation between water velocity at the seafloor and the first log value at 66.6 mbsf. We subjectively estimate an error of less than 4 ms is associated with uncertainties of velocities in the top 66.6 mbsf.

Log-Based Units

The lithology at Site 819 is dominated by variations in concentration of two principal components: calcite (either nannofossils or micrite) and clay minerals. As discussed in the previous section, variations in clay mineral control the velocity, resistivity, density, and gamma-ray logs. Thus, nearly all of the logs are highly correlative with each other (Figs. 33 and 36) and are semiquantitative indicators of relative abundance of calcite and clay minerals. Accordingly, calcite analyses of core samples are correlate well

Table 6. Percentage of calcite, aragonite, quartz, and dolomite for Site 819.

Core, section, interval (cm)	Depth (mbsf)	Calcite (%)	Aragonite (%)	Quartz (%)	Dolomite (%)
133-819A-					
1H-4, 145–150	5.95	31.4	31.8	36.8	0
2H-5, 145–150	15.95	35.6	56.6	7.7	0
3H-5, 145–150	25.45	43.1	38.6	18.4	0
4H-5, 145–150	34.95	25.9	38.0	22.1	14.0
5H-5, 145–150	44.45	37.3	47.9	11.7	3.1
6H-5, 145–150	53.95	30.9	46.1	11.7	11.3
7H-5, 145–150	63.45	33.8	48.4	16.0	1.8
8H-5, 140–150	72.90	54.3	17.2	28.5	0
9H-5, 140–150	82.40	37.6	49.9	10.1	2.4
10H-5, 140–150	91.90	34.7	48.3	17.0	0
13H-5, 140–150	118.4	27.7	51.1	21.1	0
16H-5, 140–150	137.8	39.6	49.9	10.5	0
19H-5, 140–150	166.8	38.5	53.0	7.9	0.6
23H-5, 140–150	205.5	34.7	36.8	28.5	0
25H-5, 140–150	224.4	47.6	38.2	14.3	0
28H-5, 140–150	243.4	37.3	36.5	26.3	0
31H-5, 140–150	272.3	43.5	42.7	13.8	0
34H-5, 140–150	301.3	34.5	24.3	39.4	1.9
37H-5, 140–150	330.3	44.7	39.9	15.4	0
40H-5, 140–150	358.9	50.5	33.3	16.2	0
43X-5, 140–150	387.8	44.9	36.3	18.9	0

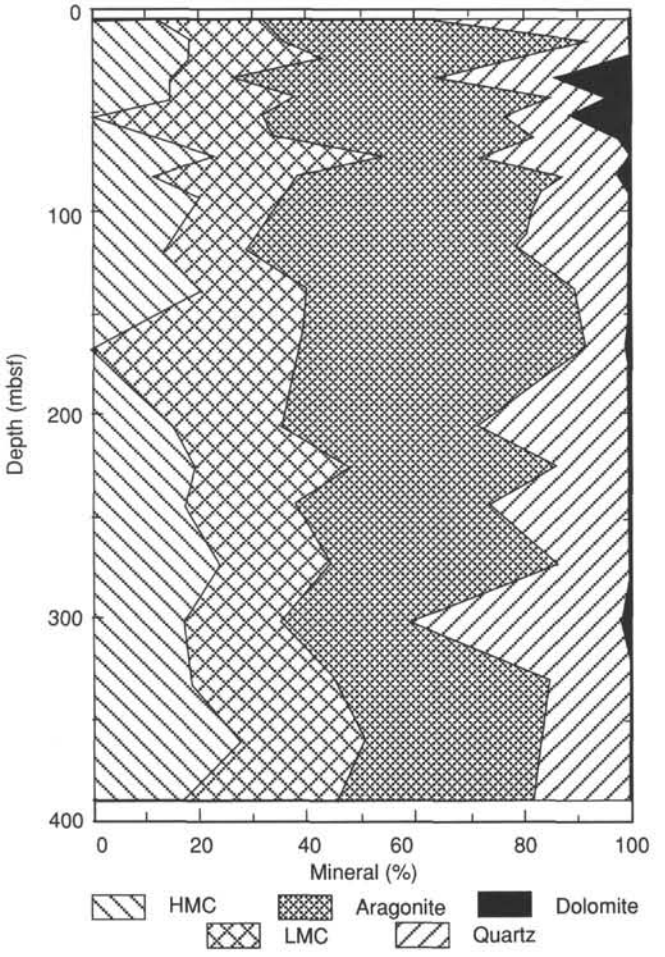

Figure 20. X-ray mineralogy data for Site 819.

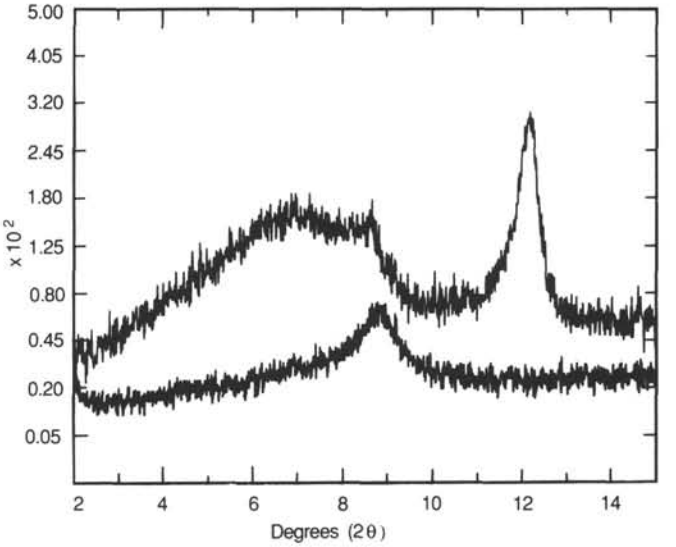

Figure 21. X-ray scan of clay fraction from Sample 133-819A-10H-5, 145–150 cm. These traces are of same sample before and after heating at 550°C for 60 min. Note the increase in intensity of the peak at 8.86° 2θ and loss of kaolinite peak at 12.29° 2θ.

with the logs (see "Lithostratigraphy" section, this chapter).

Based on log responses, the openhole logged interval of Site 819 is divisible into two units and several subunits: log Unit 1 from the base of the pipe (69 mbsf) to 162 mbsf and log Unit 2 from 162 mbsf to the bottom of the logged interval at 382 mbsf.

Log Unit 1 (<69–162 mbsf) has finer-scaled variations than log Unit 2. This unit is characterized by several upward-fining sequences 10 to 20 m thick, evident as trends of either increasing gamma rays or decreasing velocity. In contrast, only upward-coarsening sequences were identified in this interval (see "Lithostratigraphy" section, this chapter).

Log Unit 2 (162–382 mbsf) is composed of five sequences having different thicknesses but similar character. We arbitrarily defined these sequence boundaries at resistivity minima as (1) 162–214 mbsf, (2) 214–272 mbsf, (3) 272–298 mbsf, (4) 298–367 mbsf, and (5) 367 to greater than 382 mbsf.

The base of each sequence is a 1- to 5-m-thick bed having high porosity; often it is visibly clay-rich, based on gamma-ray responses. Overlying this bed is a relatively homogeneous interval at 18 to 56 m thick, presumably clayey nannofossil ooze on the basis of core descriptions (see "Lithostratigraphy" section, this volume). In the three longest sequences, this interval is gradually increasing in clay content (Fig. 36) and, consequently, increasing in porosity (decreasing velocity and resistivity in Fig. 33) throughout its lower half, then gradually decreasing in clay content throughout its upper half; in the sequence at 298 to 367 mbsf, the transition from increasing to decreasing clay occurs well above the halfway point. Each sequence is capped by a 10-m-thick "bed" with 5 m of rapidly decreasing porosity overlain by about 5 m of rapidly increasing porosity, ending at a porosity maximum substantially higher than that at the base of the bed. At its center, this bed is dense and low in clay content; thin horizons at 218, 221, and 372 mbsf are so well cemented that they probably are dolomite stringers. In the uppermost sequence, this bed is more blocky than in the other sequences, and it may not even belong to the same unit or sedimentary facies as the

Table 7. Volatile hydrocarbon data from headspace analysis at Site 819.

Core, section, interval (cm)	Depth (mbsf)	Sample	Volume (mL)	Gas chromato.	C_1 (ppm)	C_2 (ppm)	C_3 (ppm)	C_1/C_2	C_2/C_3	$C_1(C_2 + C_3)$	N-C_4 (ppm)	I-C_4 (ppm)
133-819A-												
1H-5, 145–146	7.45	HS	5	CAR132	3	0	0					
2H-5, 145–146	15.95	HS	5	CAR132	56	0	0					
3H-5, 145–146	25.45	HS	5	CAR132	8968	1	0	8968		8968		
4H-5, 145–146	34.95	HS	5	CAR132	56614	6	0	9435		9435		
5H-5, 145–146	44.45	HS	5	CAR132	58913	7	0	8416		8416		
6H-5, 145–146	53.95	HS	5	CAR132	75677	10	0	7568		7568		
7H-5, 145–146	63.45	HS	5	CAR132	28417	5	0	5683		5683		
8H-5, 145–146	72.07	HS	5	CAR132	9389	3	0	3130		3130		
9H-5, 145–146	81.3	HS	5	CAR132	9732	4	0	2433		2433		
10H-5, 145–146	90.85	HS	5	CAR132	1095	1	0	1095		1095		
11H-5, 145–146	100.27	HS	5	CAR132	7741	3	0	2580		2580		
12H-4, 149–150	109.49	HS	5	CAR132	13597	3	0	4532		4532		
13H-5, 145–146	117.53	HS	5	CAR132	1837	1	0	1837		1837		
14H-4, 149–150	124.99	HS	5	CAR132	8273	2	0	4137		4137		
16H-6, 149–150	138.48	HS	5	CAR132	8616	3	0	2872		2872		
17X-1, 149–150	141.59	HS	5	CAR132	4998	2	0	2499		2499		
18X-3, 149–150	154.19	HS	5	CAR132	23917	4	0	5979		5979		
20X-4, 0–2	173.6	HS	5	CAR132	9655	3	0	3218		3218		
21X-CC, 0–2	178.89	HS	5	CAR132	30447	4	0	7612		7612		
23X-5, 140–142	205.5	HS	5	CAR132	4230	1	0	4230		4230		
24X-4, 149–150	213.39	HS	5	CAR132	8726	3	0	2909		2909		
25X-1, 140–142	218.4	HS	5	CAR132	13690	3	0	4563		4563		
26X-2, 0–2	223.2	HS	5	CAR132	9566	4	3	2392	1.3	1367		
27X-3, 149–150	230.79	HS	5	CAR132	7549	2	0	3775		3775		
28X-1, 140–141	237.4	HS	5	CAR132	10055	3	2	3352	1.5	2011		
29X-1, 149–150	247.09	HS	5	CAR132	2593	2	2	1297	1.0	648		
30X-2, 0–1	256.8	HS	5	CAR132	6996	2	3	3498	0.7	1399		
31X-2, 140–141	267.8	HS	5	CAR132	9509	3	3	3170	1.0	1585		
32X-3, 149–150	278.99	HS	5	CAR132	5192	2	3	2596	0.7	1038		
34X-2, 140–141	296.8	HS	5	CAR132	755	2	4	378	0.5	126		
35X-2, 0–1	305	HS	5	CAR132	6719	3	6	2240	0.5	747		
36X-3, 0–1	315.69	HS	5	CAR132	8171	3	4	2724	0.8	1167		
37X-5, 149–150	330.39	HS	5	CAR132	11871	4	8	2968	0.5	989		
38X-6, 0–2	339.64	HS	5	CAR132	12870	6	10	2145	0.6	804		
39X-5, 0–2	348.2	HS	5	CAR132	9279	5	8	1856	0.6	714		
40X-6, 140–142	359.3	HS	5	CAR132	6693	3	7	2231	0.4	669		
41X-4, 149–150	366.54	HS	5	CAR132	9278	4	6	2320	0.7	928		
42X-5, 148–150	378.28	HS	5	CAR132	43863	10	18	4386	0.6	1567		
43X-5, 140–142	386.6	HS	5	CAR132	9084	4	10	2271	0.4	649		
44X-7, 0–2	397.63	HS	5	CAR132	29592	9	22	3288	0.4	955		
9H-4, 30–32	78.65	VAC	5	CAR132	496902	121	7	4107	17.0	3882		
11H-7, 33–34	102.15	VAC	5	CAR132	566435	145	11	3906	13.0	3631		
16H-5, 34–35	135.83	VAC	5	CAR132	245000	76	9	3224	8.0	2882		
17X-2, 15–16	141.75	VAC	5	CAR132	39337	3	17	13112	0.0	1967		
18X-3, 47–48	153.17	VAC	5	CAR132	116289	20	2	5814	10.0	5286		
20X-5, 148–150	176.58	VAC	5	CAR132	57445	4	0	14361		14361		
38X-5, 60–65	338.74	VAC	5	CAR132	35066	4	3	8767	1.3	5009		
39X-4, 140–150	348.1	VAC	5	CAR132	54839	6	5	9140	1.2	4985		
40X-6, 0–10	357.9	VAC	5	CAR132	125000	28	23	4464	1.2	2451		
41X-5, 15–20	366.7	VAC	5	CAR132	190000	57	44	3333	1.3	1881		
42X-5, 0–10	376.8	VAC	5	CAR132	485000	319	256	1520	1.2	843		
43X-6, 140–150	388.1	VAC	5	CAR132	190000	64	61	2969	1.0	1520		
44X-6, 20–25	396.33	VAC	5	CAR132	487649	182	174	2679	1.0	1370		
12H-4, 33–34	108.33	VAC	5	NGA	246891	11	4	22445	2.8	16459	0	0
13H-3, 25–26	113.33	VAC	5	NGA	213729	11	10	19430	1.1	9715	0	0
13H-4, 145–146	115.06	VAC	5	NGA	454676	28	9	16238	3.1	12289	0	0
42X-5, 148–150	378.28	HS	5	NGA	9408	0	13		0.0	724	0	0

four underlying sequences (see "Lithostratigraphy" section, this chapter). On the basis of log responses from the single tool string run at this site, we were unable to identify the sedimentary facies responsible for these log sequences.

Temperature

Heat flow was not measured at Site 819; thus, the thermal gradient at the site is unknown. The L-DGO temperature tool was run at the bottom of the seismic stratigraphic tool string. Because hole temperatures were reduced by circulation during coring and by hole conditioning immediately prior to logging, we were unable to infer an equilibrium thermal profile from a single temperature logging run. Our recorded temperature of 21.8°C at about 325 mbsf thus is a minimum estimate of equilibrium temperature.

The temperature tool was run not to estimate heat flow, but in case fluid flow was present. In Figure 38, a plot of measured temperature as a function of pressure was recorded simultaneously by the tool. Depths shown are approximate and may be revised by up to 5 m by post-cruise merging of Schlumberger time/depth data with temperature-tool time/pressure data.

The temperature pattern in Figure 38 exhibits evidence of thermal lags resulting from a mud-clogged end sub. Mud

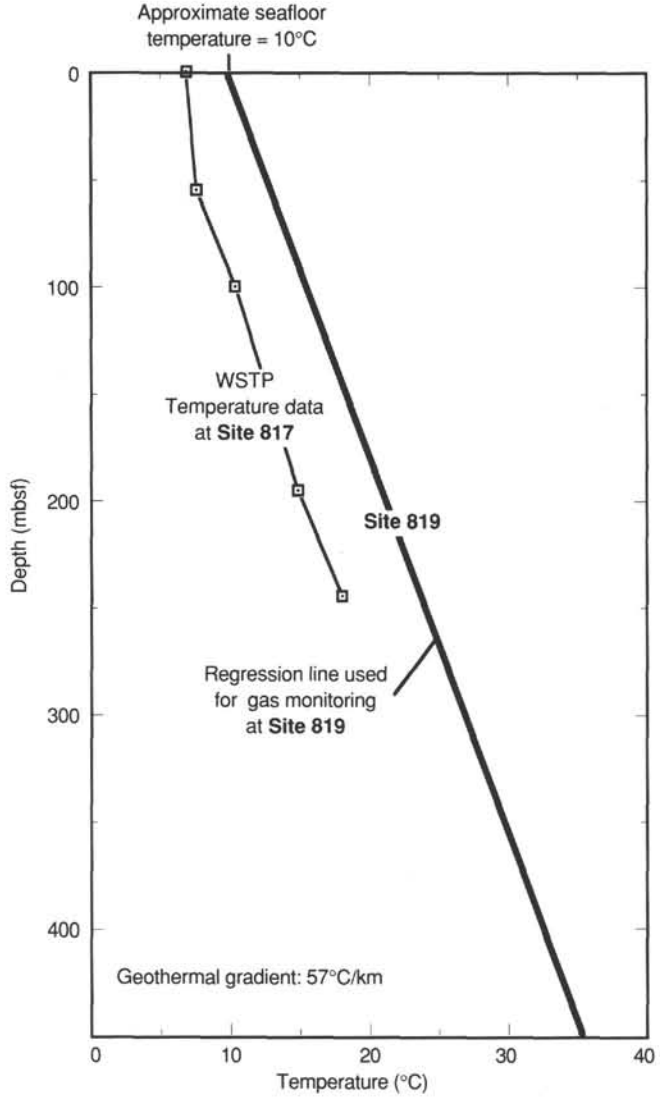

Figure 22. WSTP-temperature data from Site 817, geothermal gradient, and approximate seafloor temperature at Site 819.

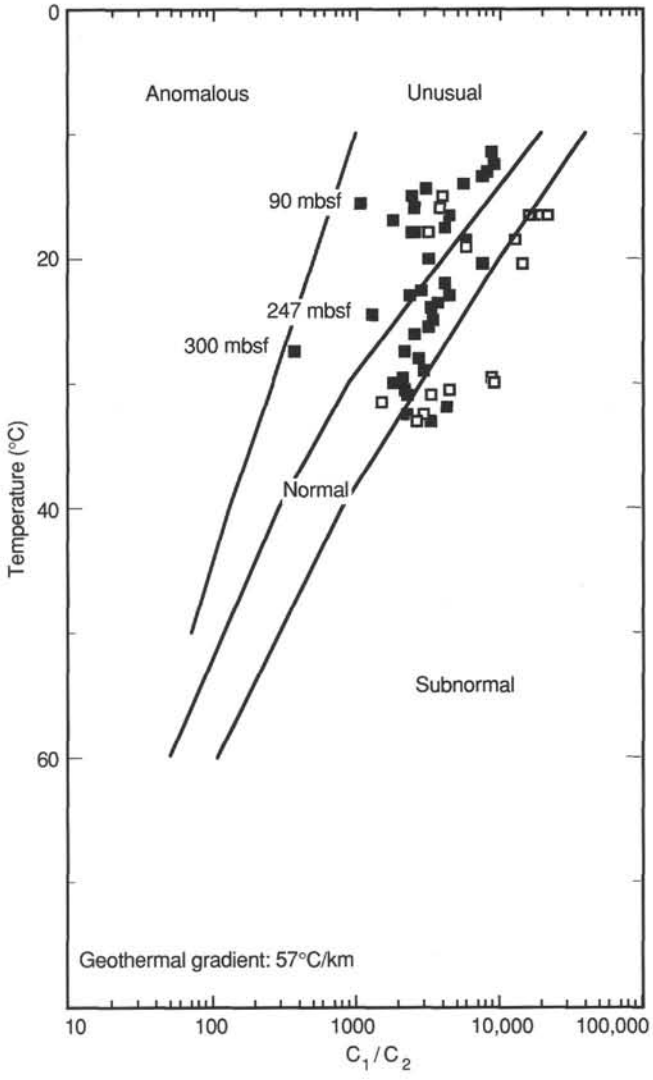

Figure 23. Distribution of C_1/C_2 ratio with temperature at Site 819 (black squares = headspace samples; white squares = vacutainer samples). This diagram was compiled for shipboard safety and pollution-prevention monitoring program.

clogging can occur when the temperature tool, which is the bottom tool of the tool string, hits the bottom of a hole that contains sticky clay. The effect on the log is a higher temperature for the upcoming log than for the downgoing log, and a maximum temperature recording not at the deepest point in the hole, but somewhat shallower than the deepest point on the upcoming log. When rigged down after logging, the temperature tool did have a mud-clogged end sub.

The downgoing log probably has been minimally affected by mud clogging. Its pattern is approximately linearly increasing temperature between the base of the pipe and 300 mbsf, then approximately constant temperature to the bottom of the hole. Both downgoing and upcoming logs indicate that through-pipe data are about 2°C cooler than the adjacent open hole; back flow was noted from the pipe onto the rig floor; the source of this presumably is a downward flow of bottom water into the hole and then up the pipe. The relatively constant temperature between 300 and 400 mbsf might have been caused by water flowing up out of the lowest penetrated portion of the formation. However, the evidence for mud clogging makes this interpretation ambiguous. Based on the thermal gradient between 100 and 300 mbsf, the extrapolated bottom-water temperature is substantially warmer than the observed bottom-water temperature. This discrepancy might have been caused by either upward flux of pore fluids out of the formation or by bottom waters that are currently cooler than average.

SEISMIC STRATIGRAPHY

We chose the locations of Sites 819, 820, and 821 on the basis of an extensive data set that includes seismic section 75/043, Part T. Our interpretation of this line, which crosses the continental edge east of Grafton Passage, is shown in Figure 39. Site 819 is the deepest site, whereas Site 821 is the shallowest site. In Figure 39, we show the interpreted seismic stratigraphy for all three sites and compare the seismic analysis with sedimentologic data. The time-depth velocity curve is shown in Figure 9.

Nine seismic sequences were identified in the section (Fig. 39). Sequences 1 through 5 represent aggrading units and can be seen only at Sites 820 and 821, whereas sequences 6 through 9 are progradational units and were seen at all three sites.

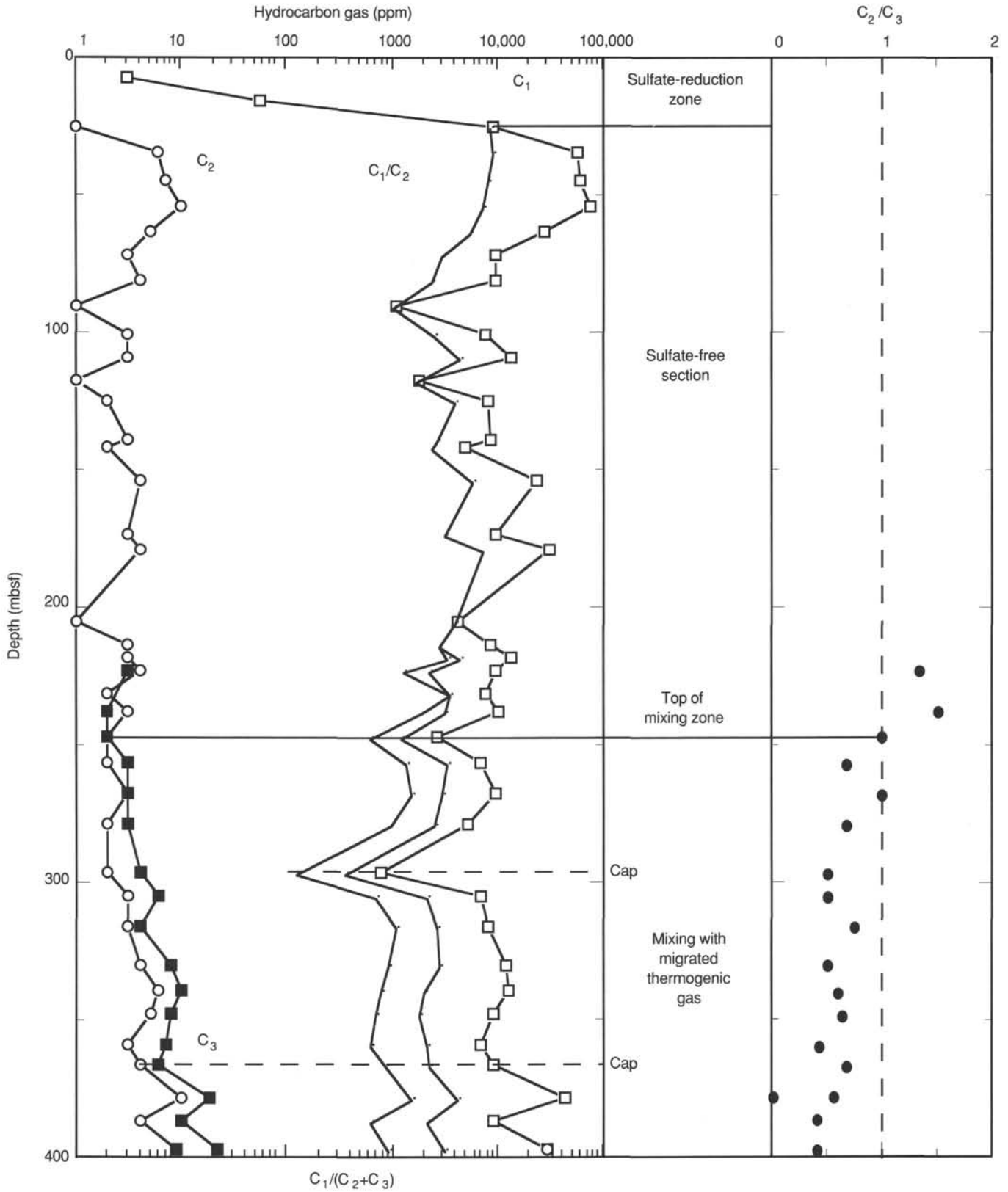

Figure 24. Distribution with depth of amounts of hydrocarbon gas in headspace samples at Site 819 and evolution of C_1/C_2 and $C_1/(C_2+C_3)$ ratios.

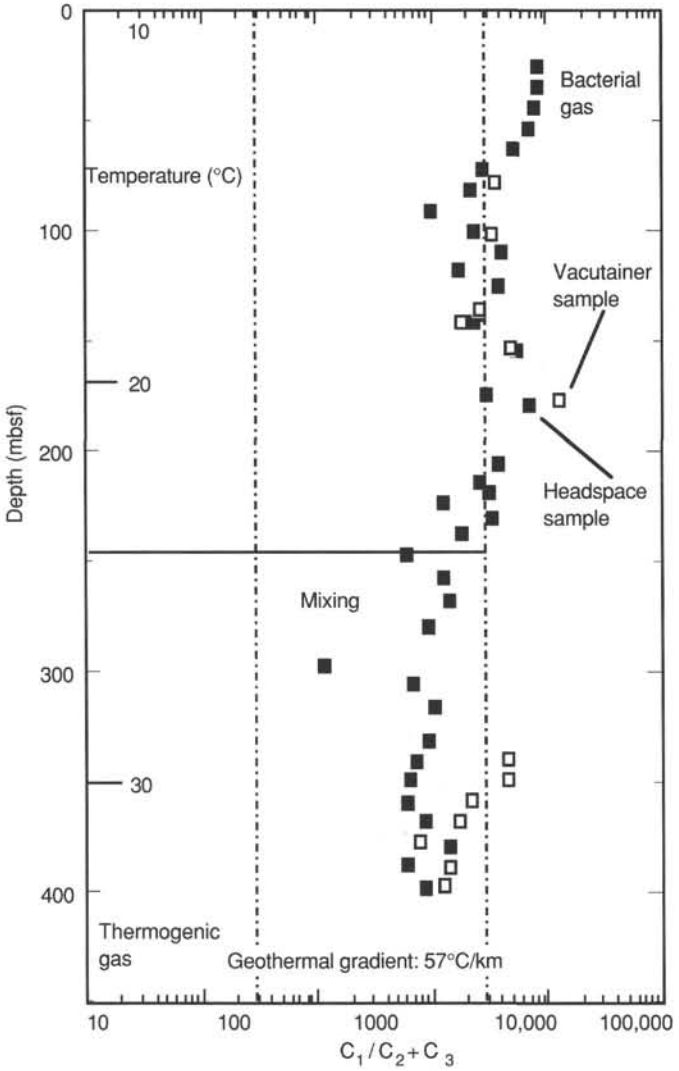

Figure 25. Evolution with depth and temperature of the $C_1/(C_2+C_3)$ ratio at Site 819. Vertical lines represent division into bacterial, mixed, and thermogenic gases.

Sequence 1 is 42 ms (TWT) thick at Site 821, 40 ms (TWT) thick at Site 820; is truncated eastward by the seafloor; and is composed of a series of strong continuous high-amplitude reflectors. To the west of Site 821, the sequence includes a downlapping unit, whereas to the east of Site 820, the lower sequence boundary is onlapped. Sequence 1 is essentially an onlapping sequence; however, it is also likely that some of the reflectors within sequence 1 are themselves unconformity surfaces.

Sequence 2 is 20 ms (TWT) thick at both Sites 820 and 821 and parallels the lower boundary of sequence 1. Sequence 2 likewise is composed of strong continuous high-amplitude reflectors that onlap onto its lower boundary and are truncated by the base of sequence 1 to the east of Site 820.

Sequence 3 is 15 ms (TWT) thick at Site 821 and 20 ms thick at Site 820 and is truncated eastward of Site 820 by both the base of sequence 2 and the seafloor.

Sequence 4 is composed of a series of strong continuous high-amplitude reflectors and is 40 ms (TWT) thick at Site 821 and 30 ms (TWT) thick at Site 820. This sequence is aggradational throughout its lower two-thirds, but the top section clearly is progradational between Sites 821 and 820. The sequence is truncated by the base of Sequence 3.

Sequence 5 is composed of strong continuous high-amplitude reflectors in the lower part, but passes upward into lower amplitude discontinuous reflectors at Site 821 and strongly discontinuous chattery high-amplitude reflectors at Site 820. This sequence thickens slightly to the west and is 60 ms (TWT) thick at Site 820 and 75 ms (TWT) thick at Site 821. A series of onlaps and downlaps were recognized within the sequence.

Sequences 1 through 5 are essentially aggradational, although erosional surfaces and onlapping and downlapping geometries can be recognized within the sequences.

Sequence 6 is the first sequence that was identified at all three sites. It is 65 ms (TWT) thick at Site 821, 70 ms (TWT) thick at Site 820, and 175 ms (TWT) thick at Site 819. Between Sites 821 and 820, the sequence is composed of a few continuous high-amplitude reflectors and also low-amplitude reflectors and transparent zones. All reflectors become high amplitude and continuous eastward and in addition, prograde in the same direction. West of Site 819, the upper part of sequence 6 is a slump with strong amplitude reflectors that form mounds. The slump plane appears to be continuous, while an increase in the slope of the margin occurs between Sites 819 and 820.

Sequence 7 is 40 ms (TWT) thick at both Sites 820 and 821, but thickens substantially to about 80 ms (TWT) east of Site 820 before thinning to less than 15 ms at Site 819. It is truncated by the base of Sequence 6. Between Sites 821 and 820, sequence 7 is composed of relatively low-amplitude reflectors that achieve a much higher amplitude as the sequence thickens eastward.

Sequence 8 is another wedge-shaped unit that thickens eastward from 45 ms (TWT) at Site 821 to 70 ms at Site 820 and achieves maximum thickness of greater than 100 ms (TWT) between Sites 820 and 819. However, the sequence is only 75 ms (TWT) thick at Site 819 because of truncation by the base of sequence 7. Internally, sequence 8 is composed of high-amplitude and discontinuous reflectors west of Site 820 and high-amplitude continuous prograding reflectors east of this site.

Sequence 9 is a major prograding unit that thickens eastward from 65 ms (TWT) at Site 821 to 115 ms (TWT) at Sites 820 and 819. However, the sequence thickens to 155 ms between the outer two sites. Throughout the section, the sequence is composed of continuous high-amplitude reflectors.

The general relationships between seismic sequences and lithologic units are shown in Figure 39. Although good correlation seems likely, we urge caution when correlating units until detailed laboratory studies have been conducted for these sediments and the facies have been mapped. However, in the context of understanding the evolution of these sequences with respect to changes in sea level, a remarkable correlation occurs among seismic reflectors, the percentage of calcium carbonate, and the magnetic intensity of the sediments. If low calcium carbonate and high magnetic intensity and susceptibility can be correlated with low sea levels, then every major reflector at Site 821 represents a possible unconformity or correlative horizon that is related to a shift in lowstands of sea level.

SUMMARY AND CONCLUSIONS

The Grafton Passage Transect (Sites 819, 820, and 821)

Our intention for drilling at Sites 819, 820 and 821 was to define the relationships between seismic geometries and depositional history during a period when the rates of sea level and changes in climate can be reasonably well understood. We did, and do, intend for the results obtained to be used to understand further the geometry and depositional history of similar sequences whose sea-level history has not been so well constrained. In our opinion, shipboard studies have demon-

Table 8. Concentrations of total organic carbon, inorganic carbon, total carbon, total nitrogen, and sulfur in headspace samples from Site 819.

Core, section, interval (cm)	Depth (mbsf)	Sample	Total organic carbon (%)	Total inorganic carbon (%)	Total carbon (%)	Nitrogen (%)	Sulfur (%)	TOC/Nitrogen
133-819A-								
1H-5, 145–146	7.45	HS	0.65	3.8	4.45	0.11	0	5.9
2H-5, 145–146	15.95	HS	0.5	8.7	9.2	0.13	0	3.8
3H-5, 145–146	25.45	HS	0.35	7.4	7.75	0.12	0	2.9
4H-5, 145–146	34.95	HS	0.35	6	6.35	0.09	0	3.9
5H-5, 145–146	44.45	HS	0.25	7.6	7.85	0.11	0	2.3
6H-5, 145–146	53.95	HS	0.35	8.95	9.3	0.11	0	3.2
7H-5, 145–146	63.45	HS	0.2	6.75	6.95	0.12	0	1.7
8H-5, 145–146	72.07	HS	0.4	5.75	6.15	0.13	0	3.1
9H-5, 145–146	81.3	HS	0.35	8.1	8.45	0.14	0	2.5
10H-5, 145–146	90.85	HS	0.35	5.35	5.7	0.12	0	2.9
12H-4, 149–150	109.49	HS	0.2	7.9	8.1	0.11	0	1.8
13H-5, 145–146	117.53	HS	0.35	5.35	5.7	0.12	0	2.9
14H-3, 140–141	124.9	HS	0.25	6.25	6.5	0.13	0	1.9
16X-6, 149–150	138.48	HS	0.3	6.65	6.95	0.14	0	2.1
17X-1, 149–150	141.59	HS	0.25	6.6	6.85	0.15	0	1.7
18X-3, 149–150	154.19	HS	0.4	8.65	9.05	0.14	0	2.9
20X-4, 0–2	173.6	HS	0.45	8.4	8.85	0.16	0	2.8
21X-CC, 0–2	178.89	HS	0.45	7.45	7.9	0.16	0	2.8
23X-5, 140–142	205.5	HS	0.45	4.55	5	0.15	0	3.0
24X-4, 149–150	213.39	HS	0.4	7.15	7.55	0.14	0	2.9
25X-1, 140–142	218.4	HS	0.35	7.25	7.6	0.14	0	2.5
26X-2, 0–2	223.2	HS	0.4	7.75	8.15	0.14	0	2.9
27X-3, 149–150	230.79	HS	0.4	6.85	7.25	0.19	0	2.1
28X-1, 140–141	237.4	HS	0.4	6.2	6.6	0.14	0	2.9
29X-1, 149–150	247.09	HS	0.55	4.45	5	0.15	0	3.7
30X-2, 0–1	256.8	HS	0.5	5.3	5.8	0.17	0	2.9
31X-2, 140–141	267.8	HS	0.4	7.2	7.6	0.16	0	2.5
32X-3, 149–150	278.99	HS	0.45	6.5	6.95	0.14	0	3.2
34X-2, 140–141	296.8	HS	0.5	3	3.5	0.18	0	2.8
35X-2, 0–1	305	HS	0.3	8.1	8.45	0.15	0	2.0
36X-3, 0–1	315.69	HS	0.4	5.45	5.85	0.14	0	2.9
37X-5, 149–150	330.39	HS	0.35	5.25	5.6	0.19	0	1.8
38X-6, 0–2	339.64	HS	0.4	5.95	6.35	0.15	0.14	2.7
39X-5, 0–2	348.2	HS	0.45	5.65	6.1	0.17	0	2.6
40X-6, 140–142	359.3	HS	0.5	5.9	6.4	0.16	0	3.1
41X-4, 149–150	366.54	HS	0.45	6.1	6.55	0.15	0	3.0
42X-5, 148–150	378.28	HS	0.5	5.6	6.1	0.17	0	2.9
43X-5, 140–142	386.6	HS	0.45	5.35	5.8	0.17	0	2.6
44X-7, 0–2	397.63	HS	0.6	4.9	5.5	0.19	0	3.2

HS = headspace sample.

strated a clear relationship between geometry and sea level; we intend for shore-based studies to refine this relationship in terms of magnitude and rate.

Sites 819, 820, and 821 define a depth transect across the upper-reef slope of the Great Barrier Reef that forms the upper continental slope of the Queensland continental margin. Drilling at all three sites to a depth of 400 m defined the essential lithologic characters of an upper-aggrading sedimentary sequence and the proximal-to-distal variation in a lower prograding sequence. We achieved excellent correlation between seismic and lithologic units as a consequence of the nearly 100% recovery from all three holes.

Stratigraphy and Sedimentation

The upper part of the Queensland continental margin is composed of middle Pleistocene to Holocene sediments that exhibit a profound change in sedimentary style from prograding to aggrading at about 930 k.y. The age of the Great Barrier Reef, as obtained from the age of seismic reflectors that pass beneath the reef sequence, is younger than 930 k.y. and possibly as young as 500 k.y. Age control at all three sites was defined through a well-preserved nannofossil and foraminifer stratigraphy. Even with paleomagnetic studies, we were unable to decipher a reversal stratigraphy.

The prograding units seen at all three sites (seismic sequences 6 to 9) exhibit a clear decrease in grain size in a distal direction (i.e., toward Site 819). This is seen in the dominance of upward-coarsening bioclastic packstone cycles at Site 821 and in a similar cyclicity in nannofossil oozes and chalks at Site 819.

The aggrading units were seen only at Sites 820 and 821 (seismic sequences 1 to 5), where they exhibited a well-developed cyclicity, which at Site 821 manifests itself as upward-fining rhythms.

Texturally, sediments of the upper slope of the Queensland margin comprise fine-grained nannofossil-clay oozes and coarser-grained wackestones and packstones that are composed of carbonates with kaolinite and illite. These clays in particular controlled measured variations in velocity, resistivity, gamma-ray, and density values. Sedimentation rates indicate that the highest rates occurred at all sites in the middle Pleistocene, but the main locus of sedimentation was at Site 819. Thereafter, during the late Pleistocene, the locus of sedimentation shifted progressively landward to the position of Site 821.

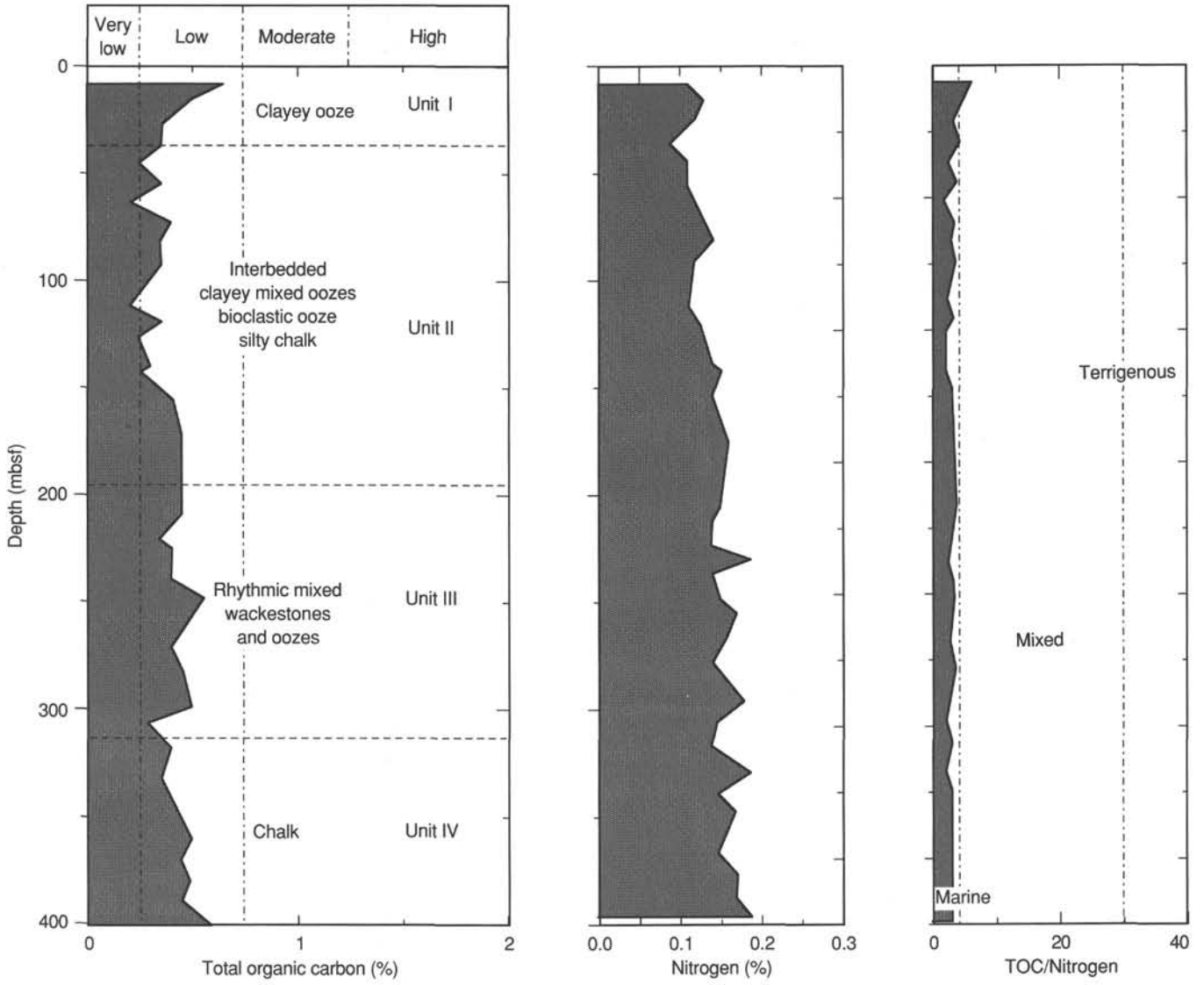

Figure 26. Distribution with depth of concentrations of total organic carbon and nitrogen, and of TOC/nitrogen ratio in headspace samples at Site 819.

Controls of Sedimentation

Sediments at all three sites exhibit a remarkable degree of cyclicity, which is seen in both seismic and drilling results. We think that cyclicity has been controlled by fluctuations in climate and sea level. Previous studies (Davies et al., 1989) indicated that sediments on the outer shelf and upper slope are dominated by either high-sea-level carbonate or low-sea-level terrigenous material. Seismic data indicate an upper-aggrading sequence, which we interpreted as alternating cyclical calcareous and terrigenous sediments representing successive high-frequency cycles of sea level, and a lower sequence of prograding and onlapping units, which we have interpreted as reflecting low-sea-level prodeltaic muds and high-sea-level carbonates that were deposited on the upper slope. Drilling confirms this general interpretation and shows both a vertical cyclicity and a depth-related, proximal-to-distal variation in deltaic sediments. The change from lower progradation to upper aggradation at about 930 k.y. is near the timing of the fluctuations in frequency of changes in Pleistocene sea level.

Drilling results at all three holes show a remarkable correlation between variations of relative percent of calcium carbonate (or conversely relative percent of noncarbonate components) and alternation of seismic reflectors (Fig. 40). Low calcium carbonate values correlate with reflectors previously interpreted as unconformities or sequence boundaries. Further, the significant correlation of low carbonate values with high magnetic intensity and susceptibility supports a conclusion that low-carbonate, high-magnetic susceptibility and seismic reflectors indicate events of low sea level, as previously inferred from seismic data. The source of this magnetization may be either fluviatile point-source influxes to the upper slope or dust related to periods of low sea level and increased aridity of the Australian continent. The corollary to this is that high calcium carbonate values correlate with high sea levels. Therefore, the percent calcium carbonate curve should approximate a relative curve in sea level. If this were true, the sequence shown in Figure 40

Table 9. Index properties data for Site 819.

Core, section, interval (cm)	Depth (mbsf)	Bulk density (g/cm^3)	Grain density (g/cm^3)	Porosity (%)	Water content (%)	Void ratio
133-819A-						
1H-1, 102–104	1.02	1.67	2.78	65.0	66.5	1.86
1H-2, 102–104	2.52	1.63	2.72	68.3	75.2	2.15
1H-3, 102–104	4.02	1.54	2.74	69.7	86.8	2.30
1H-4, 102–105	5.52	1.72	2.71	62.6	59.3	1.67
1H-5, 102–105	7.02	1.86	2.69	56.6	45.3	1.31
1H-6, 62–65	8.12	1.76	2.71	59.1	52.3	1.45
2H-1, 102–105	9.52	1.70	2.73	59.6	55.9	1.47
2H-2, 102–105	11.02	1.69	2.73	65.4	65.9	1.89
2H-3, 102–105	12.52	1.67	2.75	64.9	66.5	1.85
2H-4, 102–105	14.02	1.68	2.73	64.4	64.5	1.81
2H-5, 102–105	15.52	1.79	2.74	58.1	49.7	1.39
2H-6, 102–105	17.02	1.83	2.80	58.0	48.2	1.38
3H-1, 102–105	19.02	1.79	2.72	58.2	49.9	1.39
3H-2, 102–105	20.52	1.82	2.56	56.1	46.1	1.28
3H-3, 102–105	22.02	1.70	3.00	61.4	58.9	1.59
3H-5, 81–84	24.81	1.78	2.68	55.3	46.7	1.24
3H-6, 102–105	26.52	1.82	2.88	54.9	44.8	1.22
4H-1, 101–104	28.51	1.75	2.74	65.1	61.6	1.86
4H-2, 70–73	29.70	1.87	2.74	53.2	41.1	1.14
4H-3, 101–104	31.51	1.77	2.75	58.5	51.2	1.41
4H-4, 101–104	33.01	1.97	2.76	46.2	31.7	0.86
4H-5, 101–104	34.51	1.93	2.73	48.8	34.9	0.95
4H-6, 101–104	36.01	2.00	2.76	48.0	32.7	0.92
5H-1, 102–105	38.02	1.85	2.77	50.2	38.5	1.01
5H-2, 106–109	39.56	2.00	2.77	50.6	35.1	1.02
5H-3, 76–79	40.76	1.90	2.73	52.7	39.7	1.11
5H-4, 105–108	42.55	1.94	2.72	49.7	35.5	0.99
5H-5, 103–106	44.03	1.90	2.75	51.6	38.5	1.07
5H-6, 110–113	45.60	1.90	2.73	50.2	37.1	1.01
6H-1, 101–104	47.51	1.92	2.54	53.5	39.9	1.15
6H-2, 101–104	49.01	1.93	2.76	51.9	38.1	1.08
6H-3, 97–100	50.47	1.95	2.71	50.1	35.7	1.01
6H-4, 89–92	51.89	1.97	2.75	49.3	34.5	0.97
6H-6, 89–92	54.89	1.97	2.72	48.2	33.5	0.93
7H-5, 66–69	62.66	1.95	2.73	51.8	37.4	1.07
7H-6, 102–105	64.52	1.95	2.74	51.2	36.7	1.05
8H-2, 102–105	67.14	1.96	2.60	49.2	34.5	0.97
8H-3, 74–77	68.36	1.97	2.73	48.5	33.7	0.94
8H-4, 82–85	69.94	1.98	2.78	47.6	32.6	0.91
8H-5, 6–9	70.68	1.97	2.75	48.8	34.0	0.95
8H-6, 101–104	73.13	2.01	2.73	49.1	33.4	0.97
8H-7, 101–104	74.63	1.94	2.70	51.0	36.8	1.04
9H-2, 80–83	76.15	1.96	2.72	49.5	35.0	0.98
9H-3, 80–83	77.65	1.94	2.74	50.1	36.0	1.01
9H-4, 80–83	79.15	1.93	2.74	50.2	36.2	1.01
9H-5, 83–86	80.68	1.98	2.72	50.2	35.0	1.01
9H-6, 83–86	82.18	1.97	2.72	46.3	31.6	0.86
9H-7, 83–86	83.68	1.99	2.76	44.2	29.5	0.79
10H-3, 101–104	87.41	1.95	2.98	49.5	35.2	0.98
10H-4, 101–104	88.91	1.98	2.74	46.8	31.9	0.88
10H-5, 100–103	90.40	1.97	2.74	48.9	34.1	0.96
10H-6, 100–103	91.90	1.95	2.75	49.0	34.8	0.96
10H-7, 100–103	93.40	1.92	2.99	51.7	38.1	1.07
11H-2, 60–62	94.92	1.88	2.72	52.6	40.2	1.11
11H-3, 60–62	96.42	1.95	2.72	51.6	37.2	1.07
11H-4, 60–62	97.92	1.92	2.53	50.6	37.0	1.02
11H-5, 60–62	99.42	1.97	3.08	51.2	36.3	1.05
11H-6, 60–62	100.92	1.98	2.76	50.0	34.9	1.00
11H-7, 60–62	102.42	2.00	2.83	48.4	32.9	0.94
12H-1, 24–26	103.74	2.00	2.76	46.9	31.7	0.88
12H-2, 24–26	105.24	1.98	2.75	44.3	29.8	0.80
12H-3, 3–7	106.53	2.06	2.76	46.3	29.9	0.86
12H-4, 24–26	108.24	1.98	2.76	48.8	33.7	0.95
12H-5, 24–26	109.74	2.00	2.76	51.4	35.8	1.06
13H-2, 57–60	112.15	2.05	2.73	43.9	28.0	0.78
13H-3, 57–60	113.65	2.06	2.73	43.7	27.8	0.78
13H-4, 61–63	115.19	2.09	2.74	41.1	25.2	0.70
13H-5, 41–43	116.49	2.02	2.73	42.4	27.3	0.74
13H-6, 41–43	117.99	1.99	2.66	45.2	30.4	0.83
14H-1, 97–100	121.47	1.98	2.71	46.9	31.9	0.88
15X-1, 21–24	123.21	1.95	2.73	48.8	34.6	0.96
15X-2, 20–23	124.70	1.99	2.75	47.9	32.6	0.92
15X-3, 7–10	126.07	1.97	2.75	47.9	33.1	0.92
15X-4, 26–29	127.76	1.98	2.73	47.3	32.4	0.90
15X-5, 17–20	129.17	2.01	2.74	44.5	29.3	0.80

Table 9 (continued).

Core, section, interval (cm)	Depth (mbsf)	Bulk density (g/cm^3)	Grain density (g/cm^3)	Porosity (%)	Water content (%)	Void ratio
16H-1, 10–13	130.50	1.93	2.80	49.4	35.5	0.98
16H-2, 11–14	131.10	1.96	2.68	50.3	35.8	1.01
16H-3, 12–15	132.61	1.92	2.75	50.6	37.0	1.03
16H-4, 25–28	134.24	2.08	2.77	43.6	27.3	0.77
16H-5, 140–143	136.89	2.00	2.74	49.2	33.6	0.97
16H-6, 51–54	137.50	1.91	2.72	50.6	37.1	1.02
16H-7, 73–76	139.22	1.92	2.68	48.7	35.1	0.95
17X-2, 17–20	141.77	2.14	2.74	43.0	26.0	0.76
18X-1, 40–43	150.10	1.96	2.76	47.6	33.2	0.91
18X-2, 40–43	151.60	2.13	2.73	45.8	28.2	0.85
18X-3, 40–43	153.10	2.04	2.77	46.6	30.6	0.87
18X-4, 40–43	154.60	2.08	2.75	43.6	27.3	0.77
19X-1, 40–43	159.80	1.96	2.72	47.6	33.2	0.91
19X-2, 40–43	161.30	1.78	2.72	58.8	51.2	1.43
19X-3, 40–43	162.80	1.90	2.73	53.4	40.6	1.15
20X-1, 100–103	170.10	1.92	2.73	50.0	36.3	1.00
20X-2, 100–103	171.60	2.15	2.72	40.4	23.8	0.68
20X-3, 100–103	173.10	1.86	2.64	54.1	42.4	1.18
20X-4, 100–103	174.60	1.98	2.76	49.9	34.8	1.00
20X-5, 100–103	176.10	2.22	2.74	32.2	17.5	0.48
20X-6, 100–103	177.60	2.05	2.75	44.8	28.8	0.81
23X-1, 70–73	198.80	1.97	2.71	49.1	34.3	0.96
23X-2, 70–73	200.30	1.97	2.75	47.4	32.6	0.90
23X-3, 70–73	201.80	1.97	2.77	47.7	32.9	0.91
23X-4, 70–73	203.30	1.96	2.74	48.7	34.1	0.95
23X-5, 70–73	204.80	2.00	2.73	47.2	31.9	0.90
23X-6, 70–73	206.30	2.00	2.75	46.1	31.0	0.86
24X-1, 70–73	208.10	1.96	2.76	48.5	33.9	0.94
24X-2, 70–73	209.60	1.98	2.74	46.3	31.6	0.86
24X-3, 70–73	211.10	1.98	2.77	47.4	32.5	0.90
24X-4, 70–73	212.60	1.93	2.79	46.0	32.4	0.85
24X-5, 70–73	214.10	1.97	2.76	47.4	32.6	0.90
25X-1, 71–73	217.71	2.03	2.74	44.8	29.3	0.81
25X-2, 72–73	219.22	2.03	2.76	44.7	29.1	0.81
26X-1, 70–73	222.40	2.00	2.74	45.3	30.3	0.83
26X-2, 70–73	223.90	1.98	2.71	48.2	33.2	0.93
27X-1, 70–73	227.00	2.03	2.95	44.8	29.3	0.81
27X-2, 70–73	228.50	2.03	2.73	45.3	29.6	0.83
27X-3, 70–73	230.00	2.04	2.75	44.8	29.0	0.81
27X-4, 70–73	231.50	2.04	2.76	44.2	28.6	0.79
28X-1, 70–73	236.70	1.98	2.74	47.3	32.3	0.90
28X-2, 60–63	238.10	2.02	2.59	44.5	29.2	0.80
29X-2, 70–73	247.80	2.06	2.59	40.5	25.3	0.68
29X-3, 70–73	249.30	2.03	2.91	45.3	29.6	0.83
29X-4, 70–73	250.80	2.07	2.73	44.4	28.2	0.80
30X-1, 70–73	256.00	2.02	2.77	45.6	30.0	0.84
30X-2, 70–73	257.50	2.00	2.80	44.1	29.1	0.79
31X-1, 70–73	265.60	1.98	2.89	47.0	32.0	0.89
31X-2, 70–73	267.10	2.03	2.75	46.5	30.6	0.87
31X-3, 70–73	268.60	2.03	2.77	46.0	30.3	0.85
32X-1, 70–73	275.20	2.01	2.76	44.7	29.6	0.81
32X-2, 70–73	276.70	2.04	2.70	45.5	29.5	0.84
32X-3, 64–65	278.14	1.86	2.75	51.2	39.3	1.05
32X-4, 87–88	279.87	1.95	2.68	48.7	34.5	0.95
32X-5, 76–77	281.26	1.94	2.56	46.7	32.6	0.88
33X-1, 82–85	285.02	1.96	2.72	49.5	34.8	0.98
33X-2, 82–85	286.52	1.99	2.80	46.1	31.2	0.86
33X-3, 82–85	288.02	1.86	2.77	53.6	42.0	1.16
34X-1, 67–69	294.57	2.10	2.77	44.7	27.9	0.81
34X-2, 70–72	296.10	2.10	2.80	42.9	26.5	0.75
34X-3, 85–87	297.75	2.09	2.75	44.7	28.1	0.81
35X-1, 80–82	304.30	2.14	2.72	40.3	23.9	0.68
35X-3, 79–81	307.29	2.15	2.72	39.5	23.2	0.65
35X-4, 82–83	308.82	2.13	2.80	40.5	24.2	0.68
35X-5, 81–83	310.31	2.06	2.79	45.1	29.0	0.82
35X-6, 81–83	311.81	2.14	2.83	40.3	24.0	0.68
36X-1, 15–16	313.35	2.04	2.69	43.7	28.2	0.78
36X-2, 38–39	314.57	1.97	2.65	41.3	27.4	0.70
36X-3, 37–38	316.06	2.03	2.75	45.5	29.8	0.84
36X-4, 21–22	317.40	2.02	2.75	45.1	29.7	0.82
36X-5, 22–23	318.91	2.16	2.69	53.0	33.7	1.13
36X-6, 33–34	320.52	2.00	2.80	46.8	31.5	0.88
36X-7, 38–39	322.07	2.02	2.75	48.3	32.4	0.94
37X-1, 27–28	323.17	2.06	2.46	44.7	28.7	0.81
37X-2, 40–41	324.80	2.04	2.71	44.7	29.0	0.81
37X-3, 40–41	326.30	2.05	2.73	46.8	30.5	0.88

Table 9 (continued).

Core, section, interval (cm)	Depth (mbsf)	Bulk density (g/cm^3)	Grain density (g/cm^3)	Porosity (%)	Water content (%)	Void ratio
37X-4, 40–41	327.80	2.12	2.44	46.1	28.6	0.85
37X-5, 40–41	329.30	2.30	2.72	49.8	28.6	0.99
37X-6, 40–41	330.80	2.03	2.75	43.8	28.4	0.78
38X-1, 26–27	332.76	1.97	2.77	47.8	33.0	0.92
38X-2, 16–17	333.80	2.18	2.71	45.6	27.3	0.84
38X-3, 17–18	335.31	2.13	2.71	43.5	26.5	0.77
38X-4, 25–26	336.89	2.10	2.68	47.8	30.4	0.92
38X-5, 25–26	338.39	2.08	2.74	42.7	26.6	0.75
38X-6, 24–25	339.88	1.99	2.69	49.4	34.1	0.98
38X-7, 24–25	341.38	2.03	2.53	44.0	28.5	0.79
39X-1, 42–43	342.62	2.06	2.72	45.6	29.3	0.84
39X-2, 42–43	344.12	1.97	2.64	43.0	28.8	0.75
39X-3, 42–43	345.62	2.04	2.72	48.6	32.3	0.94
39X-4, 39–40	347.09	2.04	2.69	47.5	31.4	0.90
39X-5, 22–23	348.42	2.20	2.72	45.4	26.8	0.83
39X-6, 38–39	350.08	2.04	2.78	49.7	33.2	0.99
40X-1, 17–18	351.67	2.03	2.77	39.8	25.1	0.66
40X-2, 24–25	352.14	2.11	2.96	42.7	26.1	0.75
40X-3, 26–27	353.66	2.11	2.73	40.9	24.7	0.69
40X-4, 23–24	355.13	2.12	2.78	42.9	26.2	0.75
40X-5, 22–23	356.62	2.07	2.72	41.6	25.9	0.71
40X-6, 37–38	358.27	2.12	2.73	43.0	26.2	0.75
40X-7, 14–15	359.54	2.09	2.55	41.8	25.8	0.72
41X-1, 8–10	361.18	2.07	2.50	45.4	29.0	0.83
41X-2, 8–10	362.13	2.06	2.87	43.5	27.6	0.77
41X-3, 8–10	363.63	2.20	2.70	47.3	28.2	0.90
41X-4, 8–10	365.13	2.08	2.69	43.8	27.6	0.78
41X-5, 8–10	366.63	2.04	2.75	45.8	29.8	0.84
41X-6, 8–10	368.13	2.01	2.83	46.8	31.4	0.88
41X-7, 8–10	369.63	2.07	2.72	43.9	27.7	0.78
42X-1, 8–10	370.88	2.00	2.71	45.0	29.9	0.82
42X-2, 8–10	372.38	2.15	2.55	42.4	25.3	0.74
42X-3, 8–10	373.88	2.09	2.98	43.8	27.4	0.78
42X-4, 18–20	375.48	2.11	2.78	42.8	26.3	0.75
42X-5, 18–20	376.98	2.05	2.70	43.3	27.6	0.76
42X-6, 21–23	378.51	2.08	2.78	45.5	28.9	0.84
43X-1, 10–12	380.50	2.14	2.81	42.3	25.4	0.73
43X-2, 10–12	380.80	2.12	2.73	44.3	27.3	0.80
43X-3, 10–12	382.30	2.21	2.70	43.2	25.0	0.76
43X-4, 10–12	383.80	1.85	2.74	37.6	26.2	0.60
43X-5, 10–12	385.30	2.15	2.77	43.8	26.4	0.78
43X-6, 10–12	386.80	2.10	2.73	42.5	26.3	0.74
44X-2, 91–93	391.04	2.01	2.72	43.4	28.3	0.77
44X-3, 90–91	392.53	2.07	2.85	45.6	29.1	0.84
44X-4, 90–92	394.03	2.06	2.75	41.9	26.3	0.72
44X-5, 90–92	395.53	2.13	2.70	41.4	24.9	0.71
44X-6, 90–92	397.03	2.03	2.72	43.5	28.2	0.77
44X-7, 90–92	398.53	1.95	2.97	49.2	34.9	0.97

defines 24 cycles of rising and falling sea level. High-resolution seismic data reflect variations in sea level.

Dolomitization in the Province of the Great Barrier Reef

Dolomite occurs at all three sites, but clearly is most abundant at Site 821 (up to 40% and throughout the section between 40 and 400 m) and least abundant at Site 819 (less than 20% and only at about 60 m). This dolomite probably was promoted by the dissolution of high-Mg calcite and the degradation of albite and organic material. Some dolomitization may still be occurring, although most of the dolomitization probably occurred near the sediment/water interface, where rates of reduction in organic material are at a maximum.

Age of the Central Great Barrier Reef

A very young age for the central Great Barrier Reef (i.e., less than 1 Ma) is supported by two lines of evidence: (1) dated seismic reflectors traceable beneath the reef and (2) the presence of reef-derived sediments only in the upper part of the section at Site 821. The significance of this conclusion is substantial and transcends disciplinary boundaries. It appears that most of the world's largest carbonate province, having substantial biological diversity and complexity, has grown in less than 1 m.y. Can such diversity and complexity evolve *in situ* in such a short time, or are the biological origins of the Great Barrier Reef exogenous to the area? Where is the cradle of the Great Barrier Reef? Drilling at Sites 816 and 826 showed that the proto-Great Barrier Reef grew along the edge of the Marion Plateau during the middle Miocene and was drowned during the early Pliocene. No major barrier reef existed along the Queensland margin for nearly 2 m.y. until the initiation of the Great Barrier Reef. The factors that inhibited its growth in this time interval and the extent to which a step-back of a major reef system always implies a substantial unconformity are important and relevant geological problems. What catalyzed its growth and, once initiated, how did it survive the high–frequency oscillations of sea level during the late Pleistocene? We hope that some of these questions will be answered through planned post-cruise studies.

REFERENCES

Archie, G. E., 1942. The electrical resistivity log as an aid in determining some reservoir characteristics, *J. Pet. Tech.*, 5:1–8.

Berger, A. L., 1978. Long-term variations of caloric solar insolation resulting from earth's orbital variations. *Quat. Res.*, 9:139–167.

Boardman, M. R., Neumann, A. C., Baker, P. A., Dulin, L. A., Kenter, R. J., Hunter, G. E., and Keifer, K. B., 1986. Banktop response to Quaternary fluctuations in sea level recorded in periplatform sediments. *Geology*, 14:28–31.

Davies, P. J., 1983. Reef growth. *In* Barnes, D. J. (Ed.), *Perspectives on Coral Reefs:* Canberra (Aust. Inst. Mar. Sci., Brian Clouston), 69–106.

Davies, P. J., and Hopley, D., 1983. Growth fabrics and growth rates of Holocene reefs in the Great Barrier Reef. *BMR J. Aust. Geol. Geophys.*, 8:237–251.

Davies, P. J., Marshall, J. F., and Hopley, D., 1985. *Halimeda* bioherms—low energy reefs, northern Great Barrier Reef. *Proc. Fifth Internat. Coral Reef Symp., Tahiti:* 3:95–103.

Davies, P. J., Symonds, P. A., Feary, D. A., and Pigram, C. J., 1987. Horizontal plate motion: a key allocyclic factor in the evolution of the Great Barrier Reef. *Science*, 238:1697–1700.

_____, 1989. The evolution of the carbonate platforms of northeast Australia. *Spec. Publ. Soc. Econ. Paleontol. Mineral.*, 44:233–258.

Droxler, A. W., and Schlager, W., 1985. Glacial versus interglacial sedimentation rates and turbidite frequencies in the Bahamas. *Geology*, 13:799–802.

Falvey, D. A., and Taylor, L.W.H., 1974. Queensland Plateau and Coral Sea Basin: structural and time stratigraphic patterns. *Bull. Aust. Soc. Explor. Geophysicists*, 5:123–126.

Feary, D. A., Pigram, C. J., Davies, P. J., Symonds, P. A., Droxler, A. W., and Peerdeman, F., 1990. Ocean Drilling Program—Leg 133 safety package. *Bur. Miner. Res. Aust. Rec.*, 1990/6.

Hamilton, E. L., 1976. Variation of density and porosity with depth in deep-sea sediments. *J. Sediment. Petrol.*, 46:280–300.

_____, 1979. Sound velocity gradients in marine sediments. *J. Acoust. Soc. Am.*, 65:909–922.

Marshall, J. F., and Davies, P. J., 1982. Internal structure and Holocene evolution of One Tree Reef, southern Great Barrier Reef. *Coral Reefs*, 1:21–28.

_____, 1984. Last interglacial reef growth beneath modern reefs in the southern Great Barrier Reef. *Nature*, 307:44–46.

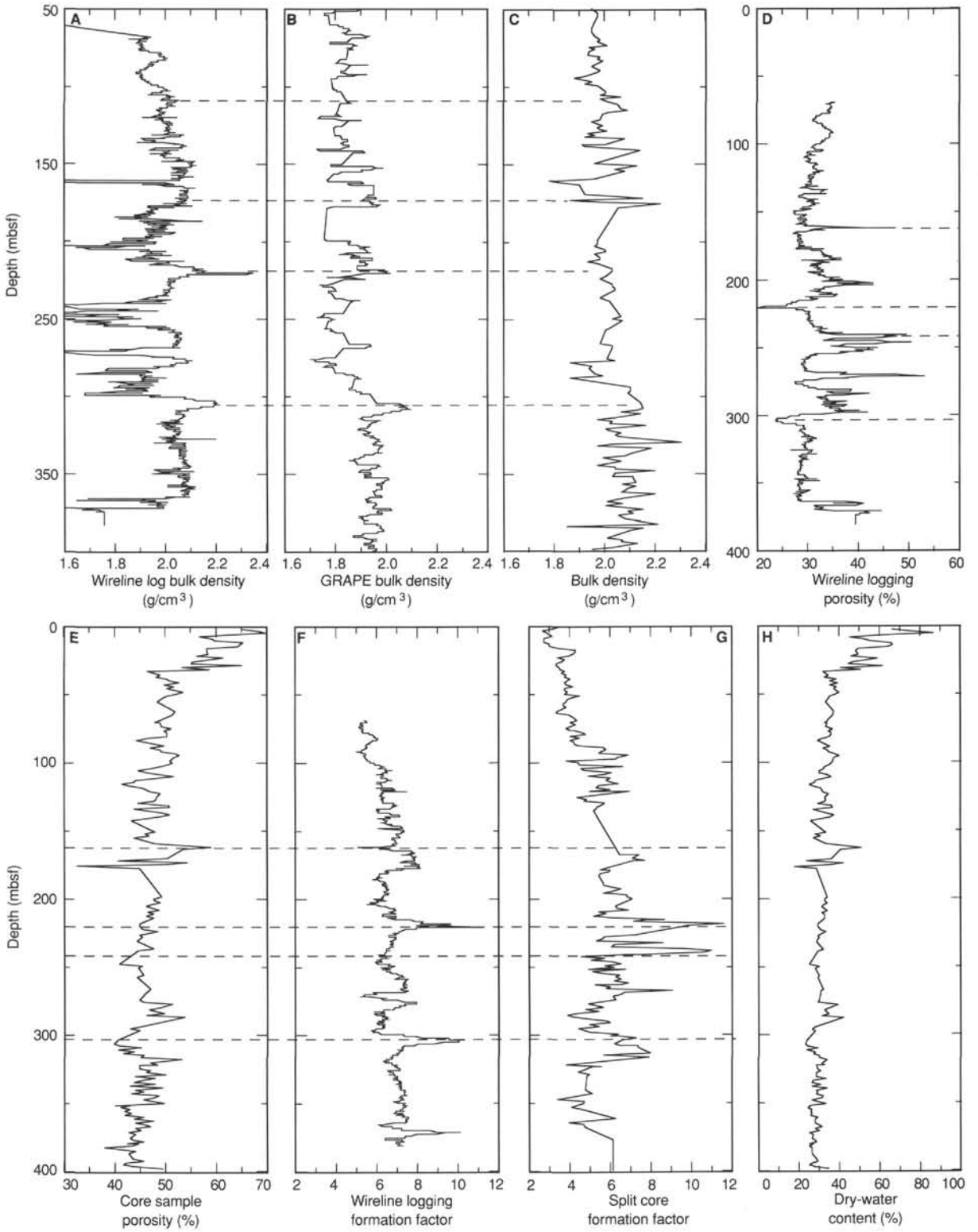

Figure 27. **A.–C.** Bulk density measurements at Site 819. Bulk densities in **C** were calculated from measurements of volume and weight of samples from split cores before and after drying. These values are listed in Table 9. Some correlations are indicated with dashed lines. Different depth series are not identical because of different sampling densities, varying hole conditions that affect the wireline logs, and gases that affect both split core samples and GRAPE data. **D.–G.** Comparison of porosity and formation factor measured using split cores with wireline logging at Site 819. Marked similarities are indicated with dashed lines. **H.** Dry water content vs. depth for Site 819. Dry water content = water mass/dry sediment mass. Data were derived from mass measurements of discrete samples from cores before and after drying.

Serra, O., 1986. *Fundamentals of Well Log Interpretation: The Interpretation of Logging Data:* Amsterdam (Elsevier).
Symonds, P. A., and Davies, P. J., 1988. Structure, stratigraphy, evolution and regional framework of the Townsville Trough and Marion Plateau region—research cruise proposal, project 9131.11. *Bur. Miner. Res. Aust. Rec.*, 1988/48.
Symonds, P. A., Davies, P. J., and Parisi, A., 1983. Structure and stratigraphy of the central Great Barrier Reef. *BMR J. Aust. Geol. Geophys.*, 8:277–291.
van Morkhoven, F.P.C.M., Berggren, W. A., Edwards, A. S., et al., 1986. Cenozoic cosmopolitan deep-water benthic foraminifera. *Bull. Cent. Rech. Explor.-Prod. Elf-Aquitaine*, Mem. 11.

Ms 133-112

NOTE: All core description forms ("barrel sheets") and core photographs have been printed on coated paper and bound separately as Part 2 of this volume, beginning on page 813.

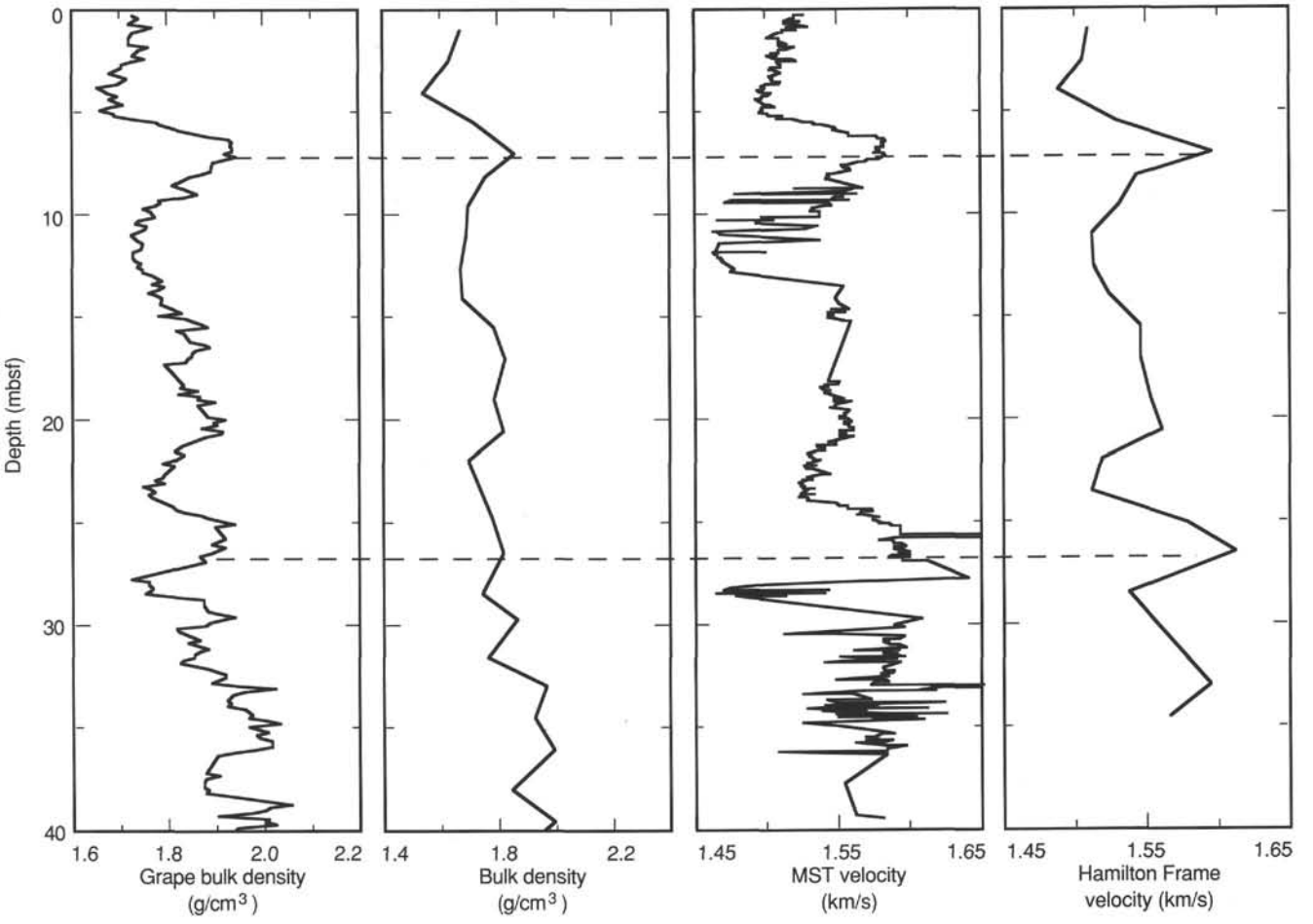

Figure 28. Comparison of density vs. velocity profiles in upper 40 m of Hole 819A. Major peaks that can be correlated across all depth series are indicated by dashed line. These profiles are characterized by a downhole decrease in velocity and density in the uppermost 6 mbsf of the section, followed by a sharp increase at 8 mbsf. Similar low-velocity wave guides have been observed elsewhere in world oceans and give rise to Stoneley waves. Presence of gas in section prevented measurement of velocity in cores or samples from split cores below 40 mbsf.

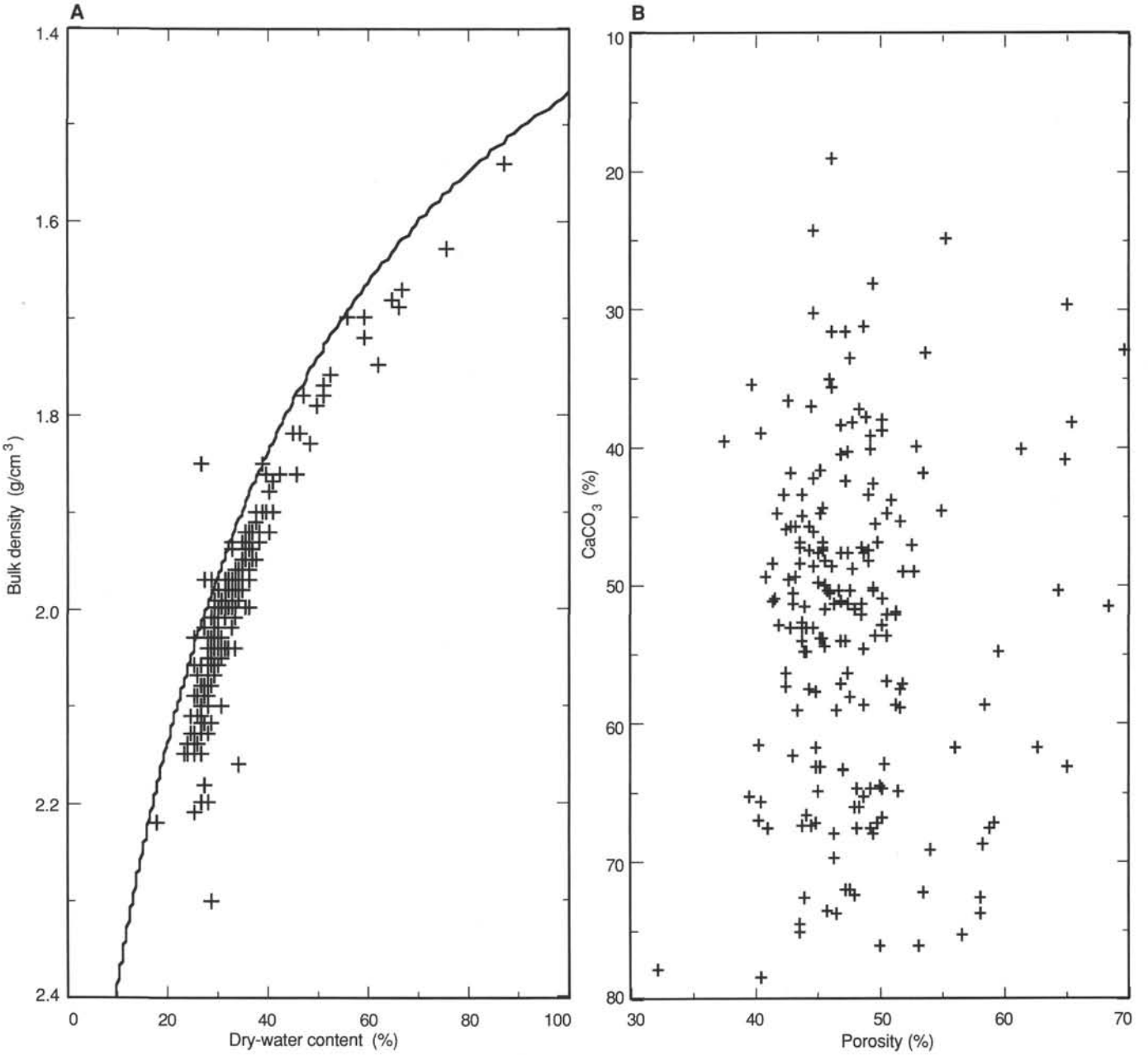

Figure 29. **A.** Dry water content vs. bulk density for Site 819. Observed data are plotted as (+). Curve is relationship between dry water content and bulk density for a material having a grain density of 2.76 g/cm^3 (the average for observed grain densities at Site 819) and a water density of 1.0. **B.** Porosity vs. weight percent of carbonate content at Site 819.

Table 10. Compressional wave velocity, Hole 819A.

Core, section, interval (cm)	Depth (mbsf)	Distance (mm)	Traveltime (μs)	Velocity (m/s)
133-819A-				
1H-1, 101–104	1.01	27.84	20.84	1510
1H-2, 101–104	2.51	28.15	21.09	1506
1H-3, 101–104	4.01	28.20	21.31	1490
1H-4, 101–104	5.51	27.85	20.62	1530
1H-5, 101–104	7.01	28.01	20.00	1597
1H-6, 61–64	8.11	28.15	20.66	1544
2H-1, 101–104	9.51	28.76	21.19	1532
2H-2, 101–104	11.01	28.46	21.21	1513
2H-3, 101–104	12.51	27.59	20.63	1514
2H-4, 101–104	14.01	28.03	20.79	1525
2H-5, 101–104	15.51	27.92	20.47	1547
2H-6, 101–104	17.01	28.28	20.71	1547
3H-1, 101–104	19.01	28.99	21.09	1554
3H-2, 101–104	20.51	28.20	20.50	1561
3H-3, 101–104	22.01	28.64	21.25	1520
3H-4, 101–104	23.51	28.41	21.18	1513
3H-5, 101–104	25.01	28.87	20.73	1579
3H-6, 101–104	26.51	26.84	19.10	1613
4H-1, 101–104	28.51	29.20	21.40	1539
4H-4, 101–104	33.01	28.37	20.24	1595
4H-5, 101–104	34.51	28.11	20.38	1567

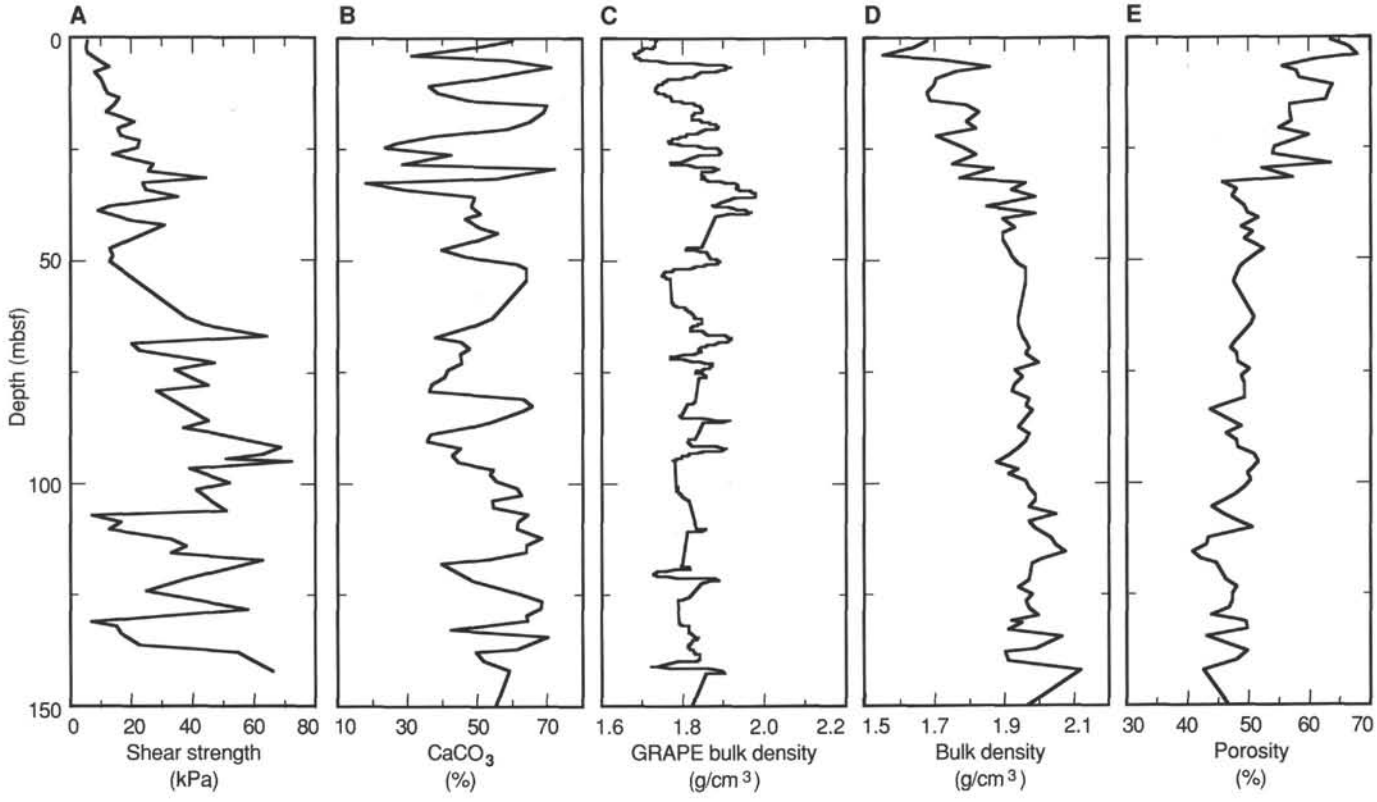

Figure 30. **A.** Physical properties vs. depth for upper 150 mbsf of Site 819. **B.** Weight percent carbonate content at Site 819. **C.** GRAPE bulk density. **D.** Bulk density from discrete samples. **E.** Porosity.

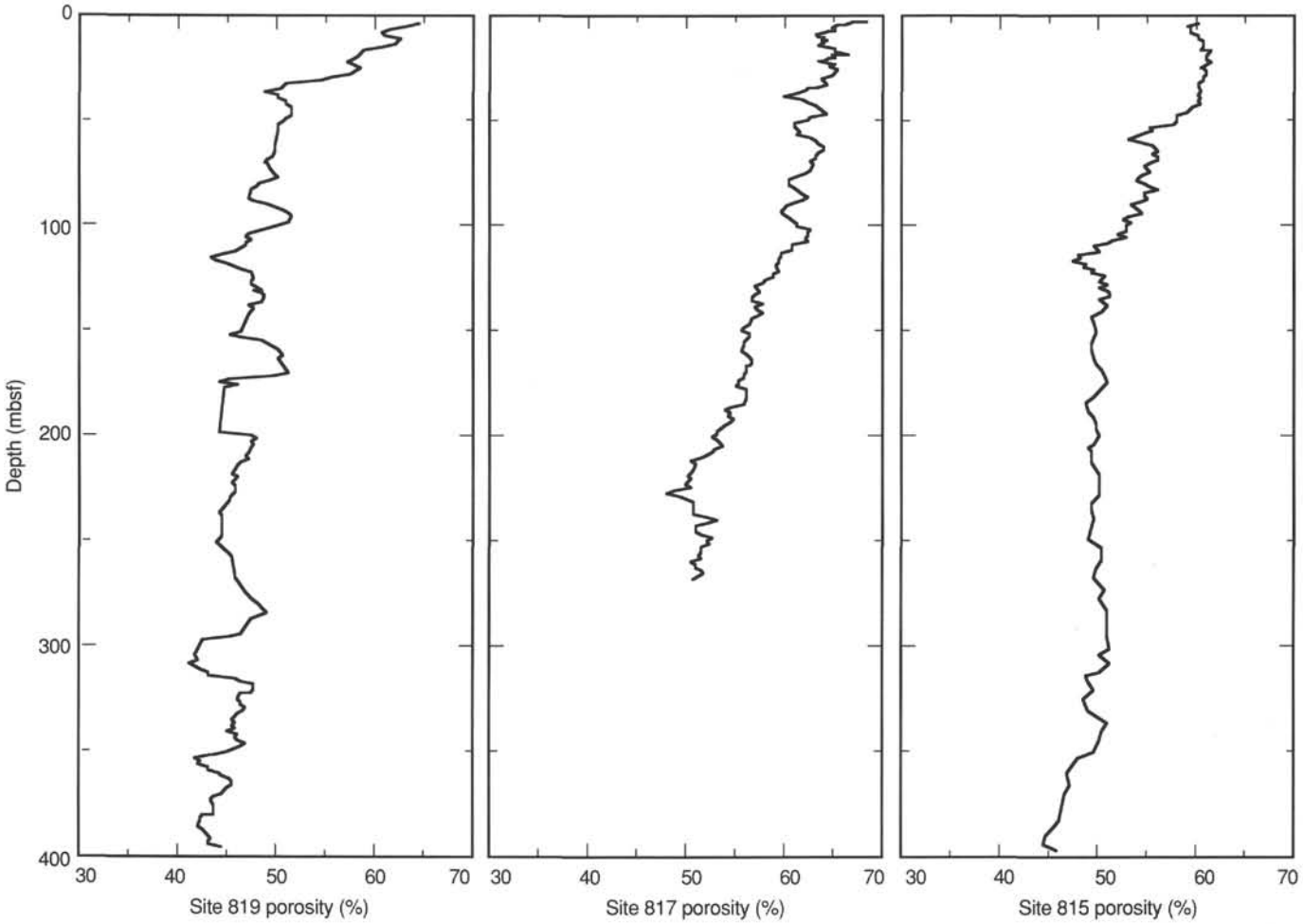

Figure 31. Plots of porosity vs. depth for Sites 819, 817, and 815. As of the drilling of Site 819 we have the most extensive data sets of porosity vs. depth at these sites.

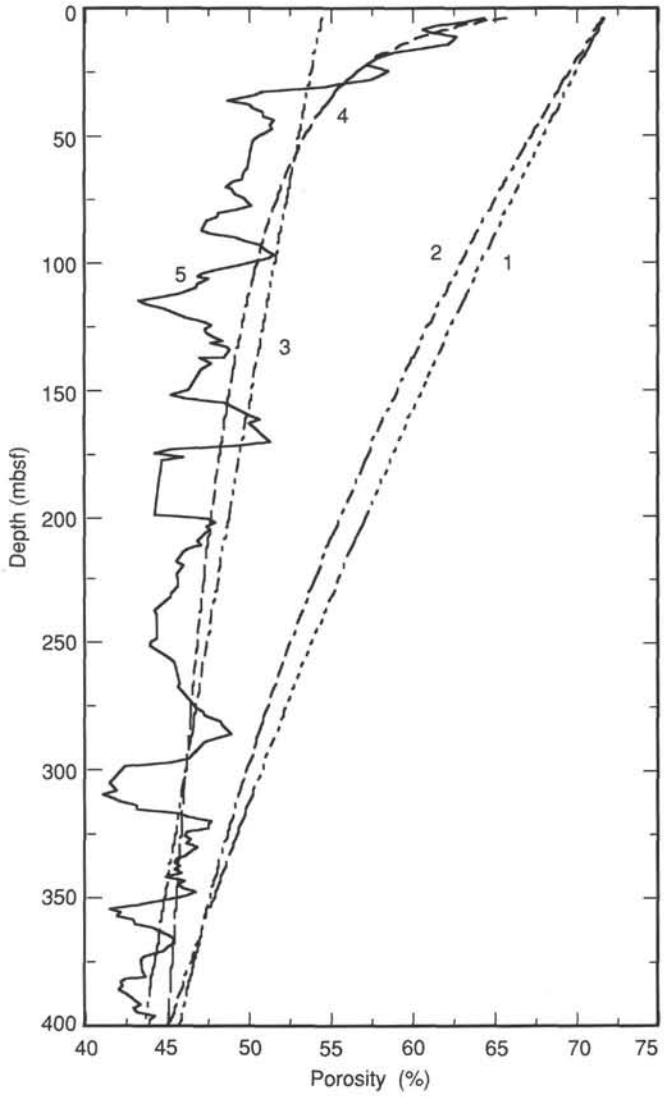

Figure 32. Comparison of porosity-depth function at Site 819 with published porosity–depth relationships. Curve 1 is Hamilton's curve (1976) for *in-situ* deep-sea terrigenous sediments. Curve 2 is Hamilton's curve for *in-situ* deep-sea calcareous sediments. Curve 3 has the form of Rubey and Hubbert's normal compaction curve (1959) for shale and was derived by least–squares fitting of a curve of the form porosity = $k \exp(-cz)$ to our data. Here, z= depth, and k and c = constants determined by least-squares fitting of the curve to our data. For Site 819, $k = 53.5$ and $c = 5.61 \times 10^{-4}$. An even better fit was obtained with a curve of the general form, porosity = kZ^{-c}, *where* k and c are determined by least-squares fitting a linear function to a plot of ln P vs. ln Z, where P = observed porosity at depth, Z (curve 4). For Site 819, $k = 74$ and $c = 0.082$. The regression coefficient $R = 0.9$ for the ln P – ln Z regression. Curve 5 is the observed porosity at Site 819.

Table 11. Electrical resistivity formation factor data for Hole 819A.

Core, section, interval (cm)	Depth (mbsf)	Seawater (ohms)	Sample (ohms)	Formation factor
133-819A-				
1H-1, 20–20	0.20	2.6	9.0	3.46
1H-1, 70–70	0.70	2.6	8.0	3.08
1H-1, 120–120	1.20	2.6	6.8	2.62
1H-2, 20–20	1.70	2.6	7.4	2.85
1H-2, 70–70	2.20	2.6	7.7	2.96
1H-2, 120–120	2.70	2.6	8.1	3.12
1H-3, 20–20	3.20	2.6	7.0	2.69
1H-3, 70–70	3.70	2.6	7.0	2.69
1H-3, 120–120	4.20	2.6	7.0	2.69
1H-4, 20–20	4.70	2.6	7.7	2.96
1H-4, 70–70	5.20	2.6	7.7	2.96
1H-4, 120–120	5.70	2.6	9.0	3.46
1H-5, 20–20	6.20	2.6	11.1	4.27
1H-5, 70–70	6.70	2.6	11.1	4.27
1H-5, 120–120	7.20	2.6	10.7	4.12
1H-6, 20–20	7.70	2.6	10.2	3.92
1H-6, 70–70	8.20	2.6	8.8	3.38
2H-1, 20–20	8.70	2.6	9.0	3.46
2H-1, 70–70	9.20	2.6	9.7	3.73
2H-1, 120–120	9.70	2.6	9.2	3.54
2H-2, 20–20	10.20	2.6	8.6	3.31
2H-2, 70–70	10.70	2.6	8.6	3.31
2H-2, 120–120	11.20	2.6	9.0	3.46
2H-3, 20–20	11.70	2.6	9.1	3.50
2H-3, 70–70	12.20	2.6	9.6	3.69
2H-3, 120–120	12.70	2.6	9.3	3.58
2H-4, 20–20	13.20	2.6	9.8	3.77
2H-4, 70–70	13.70	2.6	9.6	3.69
2H-4, 120–120	14.20	2.6	10.4	4.00
2H-5, 20–20	14.70	2.6	9.9	3.81
2H-5, 70–70	15.20	2.6	9.7	3.73
2H-5, 120–120	15.70	2.6	9.8	3.77
2H-6, 20–20	16.20	2.6	10.6	4.08
2H-6, 70–70	16.70	2.6	9.7	3.73
2H-6, 120–120	17.20	2.6	9.6	3.69
3H-1, 20–20	18.20	2.6	9.9	3.81
3H-1, 70–70	18.70	2.6	9.6	3.69
3H-1, 120–120	19.20	2.6	11.5	4.42
3H-2, 20–20	19.70	2.6	10.5	4.04
3H-2, 70–70	20.20	2.6	10.0	3.85
3H-2, 120–120	20.70	2.6	9.8	3.77
3H-3, 20–20	21.20	2.6	9.5	3.65
3H-3, 70–70	21.70	2.6	9.5	3.65
3H-3, 120–120	22.20	2.6	9.8	3.77
3H-4, 20–20	22.70	2.6	9.3	3.58
3H-4, 70–70	23.20	2.6	8.8	3.38
3H-4, 120–120	23.70	2.6	8.6	3.31
3H-5, 20–20	24.20	2.6	10.2	3.92
3H-5, 80–80	24.80	2.6	10.6	4.08
3H-6, 20–20	25.70	2.6	11.2	4.31
3H-6, 70–70	26.20	2.6	10.4	4.00
3H-6, 120–120	26.70	2.6	11.0	4.23
4H-1, 48–48	27.98	2.6	9.8	3.77
4H-1, 80–80	28.30	2.6	10.3	3.96
4H-1, 120–120	28.70	2.6	10.9	4.19
4H-2, 20–20	29.20	2.6	11.9	4.58
4H-2, 70–70	29.70	2.6	12.2	4.69
4H-2, 120–120	30.20	2.6	10.3	3.96
4H-3, 20–20	30.70	2.6	11.5	4.42
4H-3, 70–70	31.20	2.6	10.3	3.96
4H-3, 120–120	31.70	2.6	10.9	4.19
4H-4, 20–20	32.20	2.6	10.8	4.15
4H-4, 70–70	32.70	2.6	11.3	4.35
4H-4, 120–120	33.20	2.6	14.6	5.62
4H-5, 20–20	33.70	2.6	14.9	5.73
4H-5, 70–70	34.20	2.6	14.4	5.54
4H-5, 130–130	34.80	2.6	14.0	5.38
4H-6, 20–20	35.20	2.6	17.8	6.85
4H-6, 70–70	35.70	2.6	16.6	6.38
4H-6, 120–120	36.20	2.6	16.2	6.23
5H-1, 20–20	37.20	2.6	9.8	3.77
5H-1, 70–70	37.70	2.6	11.3	4.35
5H-1, 120–120	38.20	2.6	11.6	4.46
5H-2, 20–20	38.70	2.6	17.1	6.58
5H-2, 70–70	39.20	2.6	11.8	4.54

Table 11 (continued).

Core, section, interval (cm)	Depth (mbsf)	Seawater (ohms)	Sample (ohms)	Formation factor
5H-2, 120–120	39.70	2.6	12.0	4.62
5H-3, 30–30	40.30	2.6	15.6	6.00
5H-3, 70–70	40.70	2.6	14.7	5.65
5H-3, 120–120	41.20	2.6	12.6	4.85
5H-4, 37–37	41.87	2.6	15.4	5.92
5H-4, 89–89	42.39	2.6	15.0	5.77
5H-4, 132–132	42.82	2.6	15.5	5.96
5H-5, 15–15	43.15	2.6	16.6	6.38
5H-5, 73–73	43.73	2.6	14.1	5.42
5H-5, 120–120	44.20	2.6	13.7	5.27
5H-6, 18–18	44.68	2.6	15.5	5.96
5H-6, 70–70	45.20	2.6	12.8	4.92
5H-6, 117–117	45.67	2.6	17.9	6.88
6H-1, 40–40	46.90	2.6	11.2	4.31
6H-1, 80–80	47.30	2.6	12.2	4.69
6H-1, 120–120	47.70	2.6	12.5	4.81
6H-2, 20–20	48.20	2.6	12.1	4.65
6H-2, 70–70	48.70	2.6	14.7	5.65
6H-2, 120–120	49.20	2.6	14.4	5.54
6H-3, 20–20	49.70	2.6	13.8	5.31
6H-3, 70–70	50.20	2.6	13.7	5.27
6H-3, 120–120	50.70	2.6	13.4	5.15
7H-5, 70–70	62.70	2.6	16.7	6.42
7H-5, 100–100	63.00	2.6	19.1	7.35
7H-6, 20–20	63.70	2.6	18.3	7.04
7H-6, 70–70	64.20	2.6	19.8	7.62
7H-6, 120–120	64.70	2.6	18.5	7.12
8H-2, 30–30	66.42	2.6	14.9	5.73
8H-2, 70–70	66.82	2.6	14.3	5.50
8H-2, 120–120	67.32	2.6	15.4	5.92
8H-3, 20–20	67.82	2.6	15.2	5.85
8H-3, 70–70	68.32	2.6	14.3	5.50
8H-3, 120–120	68.82	2.6	14.1	5.42
8H-5, 17–17	70.79	2.6	14.5	5.58
8H-5, 70–70	71.32	2.6	14.5	5.58
8H-5, 120–120	71.82	2.6	15.6	6.00
8H-6, 20–20	72.32	2.6	16.9	6.50
8H-6, 70–70	72.82	2.6	15.8	6.08
8H-6, 120–120	73.32	2.6	14.5	5.58
8H-7, 20–20	73.82	2.6	17.5	6.73
8H-7, 70–70	74.32	2.6	17.6	6.77
8H-7, 120–120	74.82	2.6	18.3	7.04
9H-3, 30–30	77.15	2.6	16.2	6.23
9H-3, 70–70	77.55	2.6	16.3	6.27
9H-3, 120–120	78.05	2.6	17.7	6.81
9H-4, 20–20	78.55	2.6	14.1	5.42
9H-4, 70–70	79.05	2.6	15.0	5.77
9H-4, 120–120	79.55	2.6	13.4	5.15
9H-5, 20–20	80.05	2.6	15.7	6.04
9H-5, 70–70	80.55	2.6	22.3	8.58
9H-5, 120–120	81.05	2.6	20.0	7.69
9H-6, 24–24	81.59	2.6	18.4	7.08
9H-6, 70–70	82.05	2.6	30.0	11.54
9H-6, 120–120	82.55	2.6	25.5	9.81
10H-2, 20–20	85.10	2.6	18.7	7.19
10H-2, 70–70	85.60	2.6	14.8	5.69
10H-2, 120–120	86.10	2.7	15.0	5.56
10H-3, 20–20	86.60	2.7	14.2	5.26
10H-3, 70–70	87.10	2.7	23.0	8.52
10H-3, 120–120	87.60	2.7	16.6	6.15
10H-4, 20–20	88.10	2.7	16.3	6.04
10H-4, 70–70	88.60	2.7	25.6	9.48
10H-4, 120–120	89.10	2.7	29.5	10.93
10H-5, 20–20	89.60	2.8	29.5	10.54
10H-5, 70–70	90.10	2.8	20.6	7.36
10H-5, 110–110	90.50	2.8	19.0	6.79
10H-6, 20–20	91.10	2.8	12.6	4.50
10H-6, 70–70	91.60	2.8	15.8	5.64
10H-6, 110–110	92.00	2.8	13.9	4.96
10H-7, 20–20	92.60	2.8	17.0	6.07
10H-7, 70–70	93.10	2.8	18.2	6.50
10H-7, 120–120	93.60	2.8	15.9	5.68
10H-8, 20–20	94.10	2.8	17.3	6.18
11H-2, 20–20	94.52	2.8	13.6	4.86
10H-8, 70–70	94.60	2.8	18.7	6.68
11H-2, 70–70	95.02	2.8	14.1	5.04

Table 11 (continued).

Core, section, interval (cm)	Depth (mbsf)	Seawater (ohms)	Sample (ohms)	Formation factor
11H-2, 120–120	95.52	2.8	15.5	5.54
11H-3, 20–20	96.02	2.8	18.0	6.43
11H-3, 70–70	96.52	2.8	17.5	6.25
11H-3, 120–120	97.02	2.8	18.2	6.50
11H-4, 20–20	97.52	2.8	17.3	6.18
11H-4, 70–70	98.02	2.8	19.2	6.86
11H-4, 120–120	98.52	2.8	18.2	6.50
11H-5, 20–20	99.02	2.9	15.1	5.21
11H-5, 70–70	99.52	2.9	17.2	5.93
11H-5, 110–110	99.92	2.8	16.1	5.75
11H-6, 20–20	100.52	2.8	25.2	9.00
11H-6, 70–70	101.02	2.8	18.6	6.64
11H-6, 110–110	101.42	2.8	18.1	6.46
11H-7, 24–24	102.06	2.8	17.0	6.07
11H-7, 80–80	102.62	2.8	17.2	6.14
11H-7, 120–120	103.02	2.8	17.4	6.21
12H-1, 20–20	103.70	2.8	15.3	5.46
12H-1, 80–80	104.30	2.8	13.6	4.86
12H-2, 20–20	105.20	2.9	16.2	5.59
12H-2, 70–70	105.70	2.9	13.7	4.72
12H-2, 120–120	106.20	2.9	15.6	5.38
12H-3, 45–45	106.95	2.9	12.8	4.41
12H-3, 75–75	107.25	2.9	11.1	3.83
12H-3, 106–106	107.56	2.9	12.0	4.14
12H-4, 20–20	108.20	2.9	14.3	4.93
12H-4, 70–70	108.70	2.9	16.6	5.72
12H-4, 120–120	109.20	2.9	17.3	5.97
12H-5, 30–30	109.80	2.9	14.2	4.90
12H-5, 70–70	110.20	2.9	15.6	5.38
12H-5, 120–120	110.70	2.9	12.7	4.38
13H-2, 20–20	111.78	2.9	14.2	4.90
13H-2, 70–70	112.28	2.9	18.5	6.38
13H-2, 120–120	112.78	2.9	17.2	5.93
13H-3, 20–20	113.28	2.9	18.7	6.45
13H-3, 60–60	113.68	2.9	20.9	7.21
13H-3, 112–112	114.20	2.9	19.0	6.55
13H-4, 52–52	115.10	2.9	17.9	6.17
13H-4, 90–90	115.48	2.9	18.7	6.45
13H-4, 133–133	115.91	2.9	21.2	7.31
13H-5, 20–20	116.28	2.9	21.3	7.34
13H-5, 70–70	116.78	2.8	21.1	7.54
13H-6, 20–20	117.78	2.8	22.1	7.89
13H-6, 65–65	118.23	2.8	15.7	5.61
13H-6, 120–120	118.78	2.8	22.0	7.86
14H-1, 20–20	120.70	2.9	11.0	3.79
14H-1, 77–77	121.27	2.9	16.0	5.52

Table 11 (continued).

Core, section, interval (cm)	Depth (mbsf)	Seawater (ohms)	Sample (ohms)	Formation factor
14H-1, 120–120	121.70	2.9	14.6	5.03
15X-1, 20–20	123.20	2.9	12.8	4.41
15X-1, 70–70	123.70	2.9	14.2	4.90
15X-1, 120–120	124.20	2.9	13.9	4.79
15X-4, 22–22	127.72	2.9	13.7	4.72
15X-4, 70–70	128.20	2.9	14.0	4.83
15X-4, 120–120	128.70	2.9	14.6	5.03
16H-1, 20–20	130.60	2.9	9.7	3.34
16H-2, 20–20	131.19	2.9	13.5	4.66
16H-2, 70–70	131.69	2.9	13.4	4.62
16H-2, 124–124	132.23	2.9	12.5	4.31
16H-3, 20–20	132.69	2.9	11.7	4.03
16H-3, 40–40	132.89	2.9	13.1	4.52
16H-5, 50–50	135.99	2.9	18.0	6.21
16H-5, 120–120	136.69	2.9	11.4	3.93
16H-6, 25–25	137.24	2.9	13.4	4.62
16H-6, 60–60	137.59	2.9	13.4	4.62
16H-6, 127–127	138.26	2.9	13.9	4.79
17X-2, 20–20	141.80	2.9	17.6	6.07
32X-3, 9–9	277.59	2.6	15.9	6.12
32X-3, 20–20	277.70	2.6	15.3	5.88
32X-3, 72–72	278.22	2.6	15.7	6.04
32X-3, 100–100	278.50	2.6	15.3	5.88
32X-4, 13–13	279.13	2.6	20.0	7.69
32X-4, 57–57	279.57	2.6	17.8	6.85
33X-1, 21–21	284.41	2.6	19.7	7.58
33X-1, 70–70	284.90	2.6	22.0	8.46
33X-1, 120–120	285.40	2.6	20.6	7.92
33X-2, 20–20	285.90	2.6	21.5	8.27
33X-2, 70–70	286.40	2.6	20.0	7.69
33X-2, 120–120	286.90	2.6	18.9	7.27
33X-3, 20–20	287.40	2.6	17.0	6.54
33X-3, 70–70	287.90	2.6	19.4	7.46
33X-3, 117–117	288.37	2.6	20.6	7.92
34X-1, 20–20	294.10	2.6	20.3	7.81
34X-1, 70–70	294.60	2.6	21.1	8.12
34X-1, 120–120	295.10	2.6	19.1	7.35
34X-2, 20–20	295.60	2.6	24.3	9.35
34X-2, 70–70	296.10	2.6	22.3	8.58
34X-2, 120–120	296.60	2.6	19.2	7.38
34X-3, 30–30	297.20	2.6	20.5	7.88
34X-3, 70–70	297.60	2.6	20.9	8.04
34X-3, 120–120	298.10	2.6	20.0	7.69
35X-1, 20–20	303.70	2.6	17.9	6.88
35X-1, 70–70	304.20	2.6	20.2	7.77
35X-1, 120–120	304.70	2.6	26.2	10.08

Table 12. Vane shear strength data for Hole 819A.

Core, section, interval (cm)	Depth (mbsf)	Spring number	Torque (degrees)	Strain (degrees)	Shear strength (kPa)
133-819A-					
1H-1, 92–93	0.92	1	28	18	5.9
1H-2, 92–93	2.42	1	25	13	5.3
1H-3, 92–93	3.92	1	28	11	5.9
1H-4, 92–93	5.42	1	43	16	9.1
1H-5, 92–93	6.92	1	61	23	12.9
1H-6, 52–53	8.02	1	37	21	7.9
2H-1, 92–93	9.42	1	50	15	10.6
2H-2, 92–93	10.92	1	55	11	11.7
2H-3, 92–93	12.42	1	60	15	12.7
2H-4, 92–93	13.92	1	77	20	16.3
2H-5, 92–93	15.42	1	69	24	14.6
2H-6, 92–93	16.92	1	56	20	11.9
3H-1, 92–93	18.92	1	99	20	21.0
3H-2, 92–93	20.42	1	75	21	15.9
3H-3, 92–93	21.92	1	79	15	16.8
3H-4, 92–93	23.42	1	108	16	22.9
3H-5, 92–93	24.92	1	105	25	22.3
3H-6, 92–93	26.42	1	67	24	14.2
4H-1, 92–93	28.42	1	128	11	27.2
4H-2, 101–102	30.01	1	120	20	25.5
4H-3, 98–99	31.48	1	210	28	44.6
4H-4, 91–92	32.91	1	114	20	24.2
4H-5, 91–92	34.41	1	117	26	24.8
4H-6, 91–92	35.91	1	167	23	35.4
5H-1, 91–92	37.91	4	11	12	13.1
5H-2, 80–81	39.30	4	8	8	9.5
5H-3, 94–95	40.94	4	17	6	20.2
5H-4, 93–94	42.43	4	26	20	30.9
6H-1, 92–93	47.42	4	11	7	13.1
6H-2, 92–93	48.92	4	12	12	14.3
6H-3, 92–93	50.42	4	11	13	13.1
7H-5, 78–79	62.78	4	32	19	38.1
7H-6, 98–99	64.48	4	37	18	44.0
8H-2, 93–94	67.05	4	54	18	64.2
8H-3, 97–98	68.59	4	17	12	20.2
8H-4, 95–96	70.07	4	19	13	22.6
8H-6, 95–96	73.07	4	40	16	47.6
8H-7, 97–98	74.59	4	29	12	34.5
9H-2, 107–108	76.42	4	34	16	40.4
9H-3, 107–108	77.92	4	38	17	45.2
9H-4, 107–108	79.42	4	24	12	28.5
10H-2, 107–108	85.97	4	38	16	45.2
10H-3, 107–108	87.47	4	31	10	36.9
10H-4, 109–110	88.99	4	40	13	47.6
10H-5, 95–96	90.35	4	49	17	58.3
10H-6, 95–96	91.85	4	58	15	69.0
10H-7, 95–96	93.35	4	53	17	63.0
10H-8, 80–81	94.70	4	43	8	51.1
11H-2, 90–91	95.22	4	61	11	72.5
11H-3, 96–97	96.78	4	33	10	39.2
11H-5, 104–105	99.86	4	44	15	52.3
11H-6, 97–98	101.29	4	35	11	41.6
12H-1, 69–70	104.19	4	39	16	46.4
12H-2, 91–9392	105.91	4	43	13	51.1
12H-3, 71–72	107.21	4	6	12	7.1
12H-4, 81–82	108.81	4	14	11	16.7
12H-5, 93–94	110.43	4	11	10	13.1
13H-2, 78–79	112.36	4	28	11	33.3
13H-3, 106–107	114.14	4	32	13	38.1
13H-4, 119–120	115.77	4	28	13	33.3
13H-5, 119–120	117.27	4	53	18	63.0
14H-1, 89–90	121.39	4	32	15	38.1
15X-1, 99–100	123.99	4	21	14	25.0
15X-4, 89–90	128.39	4	49	12	58.3
16H-1, 47–48	130.87	4	6	2	7.1
16H-2, 103–104	132.02	4	13	8	15.5
16H-3, 88–89	133.37	4	14	20	16.7
16H-5, 101–102	136.50	4	19	26	22.6
16H-6, 81–82	137.80	4	46	11	54.7
17X-2, 31–32	141.91	4	56	12	66.6

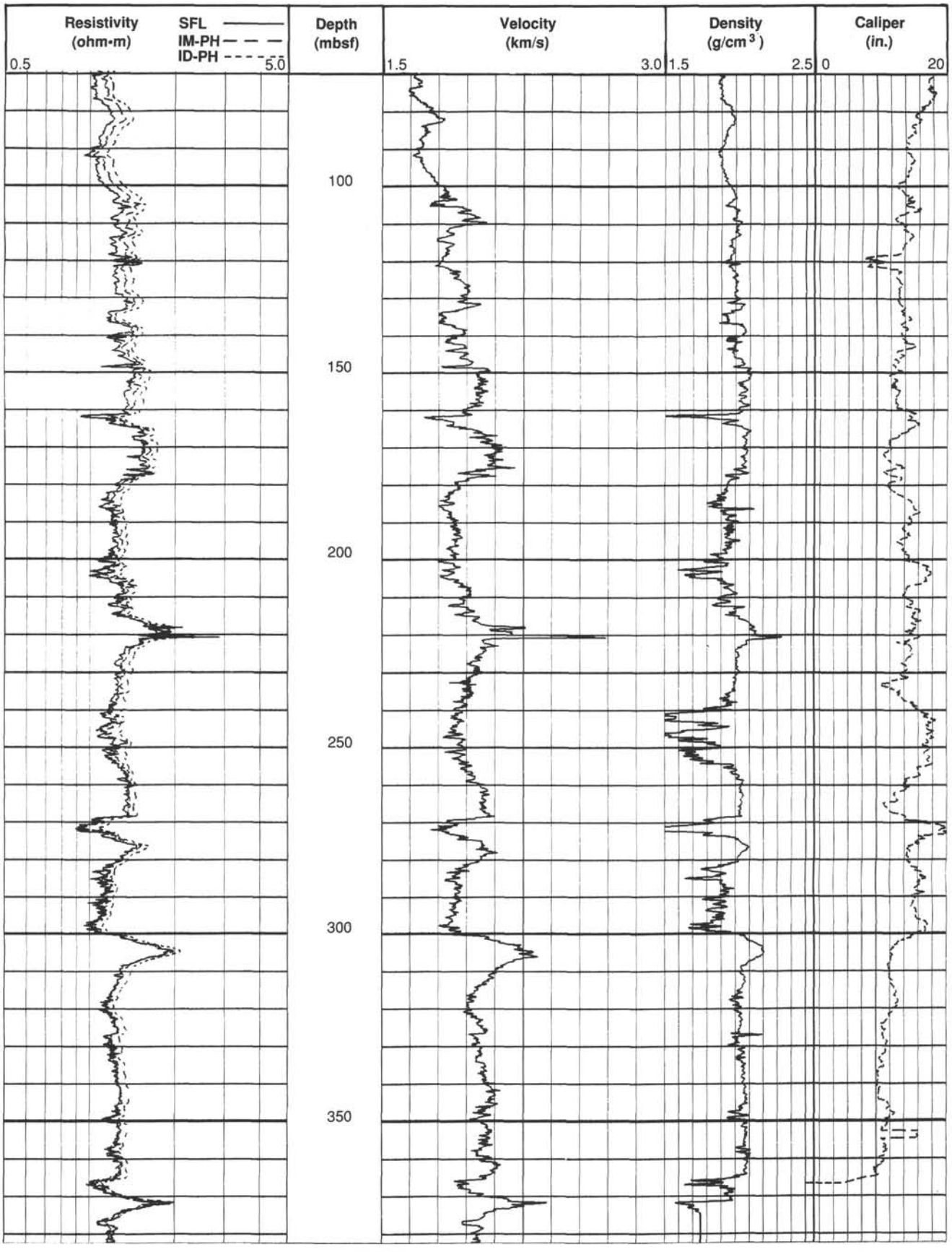

Figure 33. Primary porosity logs obtained using seismic stratigraphic tool string at Hole 819A.

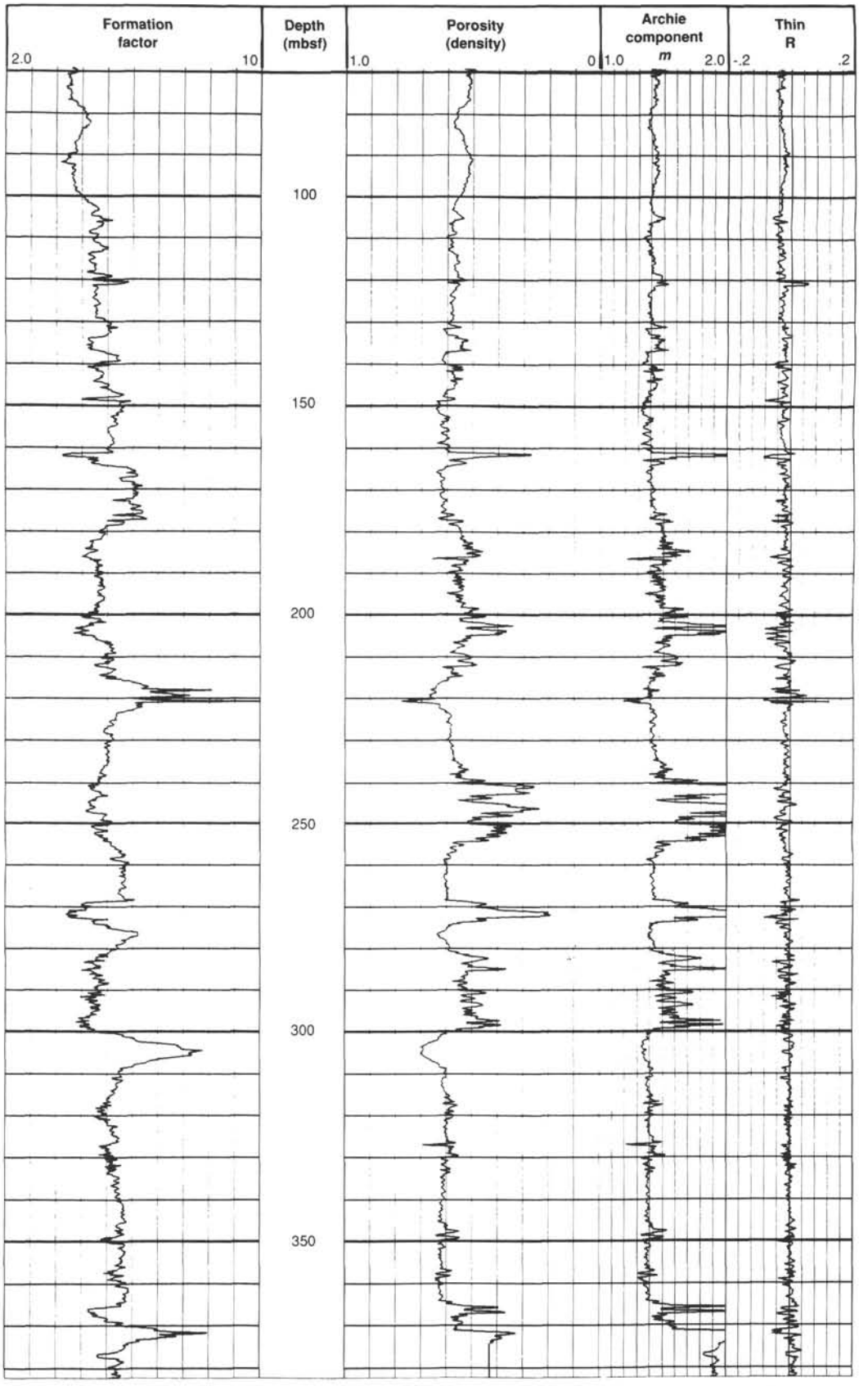

Figure 34. Site 819 logs of electrical resistivity formation factor (from ratio of formation resistivity to fluid resistivity), porosity (from density), Archie's component, m, (1942) relating formation factor to porosity, and the parameter, "Thin R," which responds to thin-bed effects.

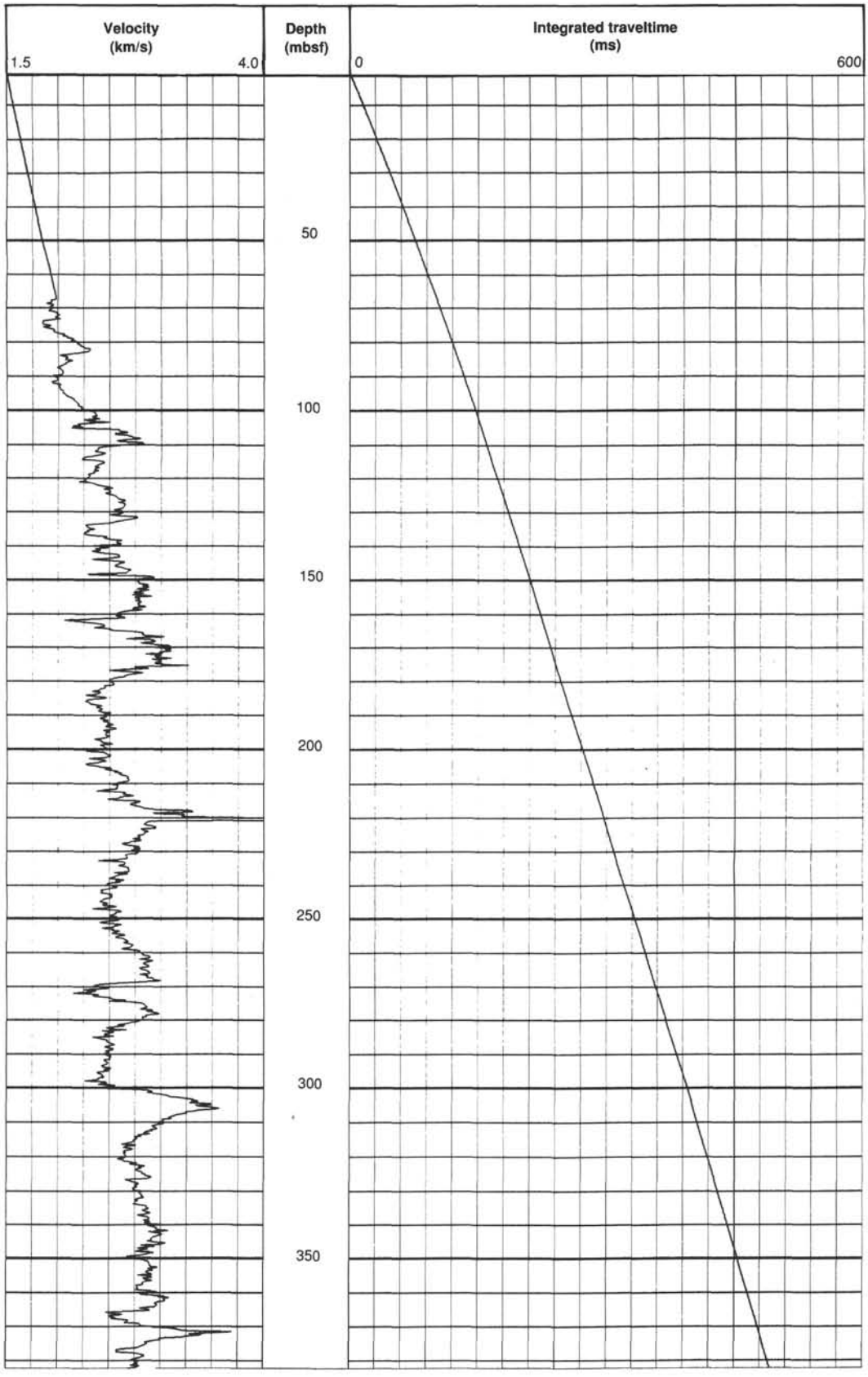

Figure 35. Velocity log, and integrated TWT function that it implies, for matching core-based information from Site 819 to seismic sections across the site.

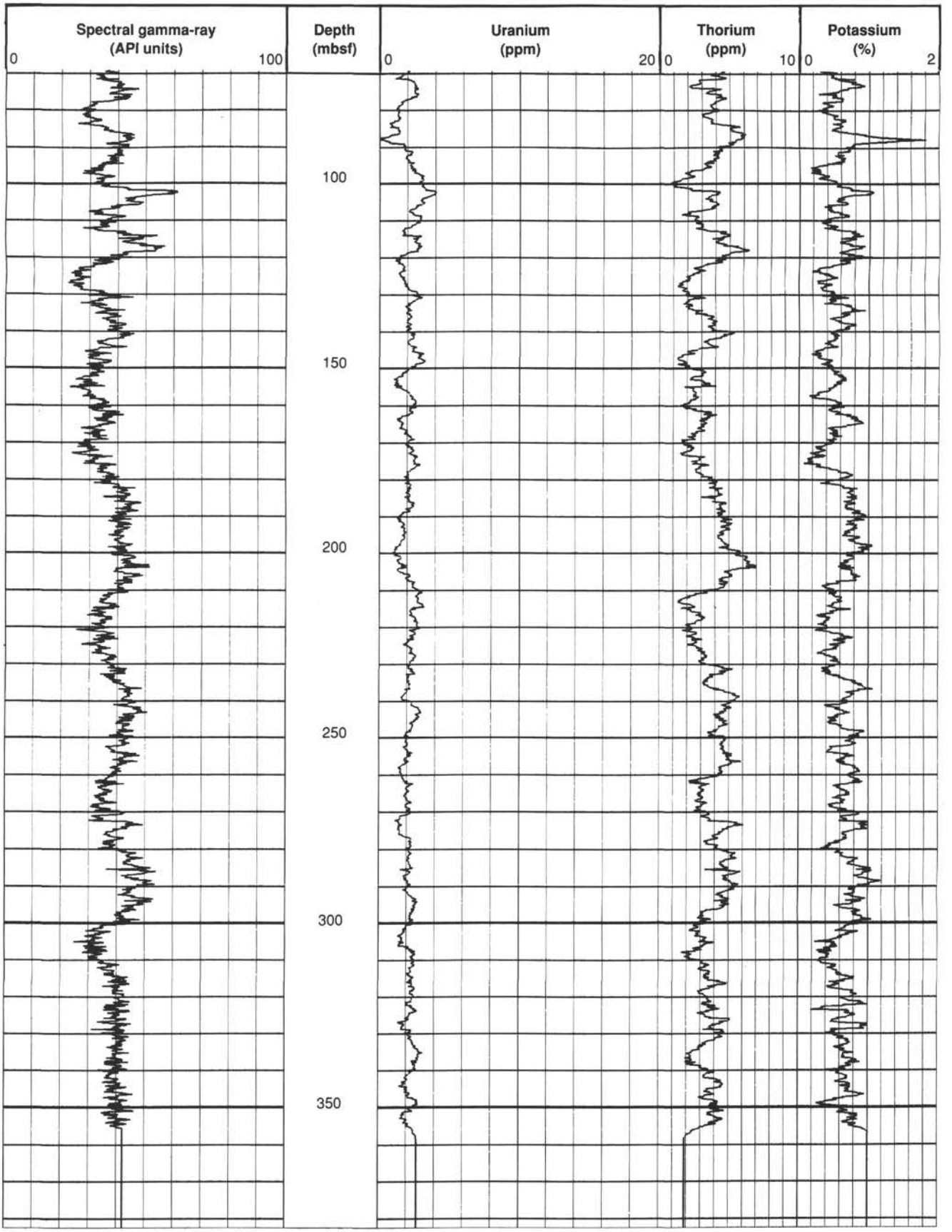

Figure 36. Spectral gamma-ray logs for Site 819.

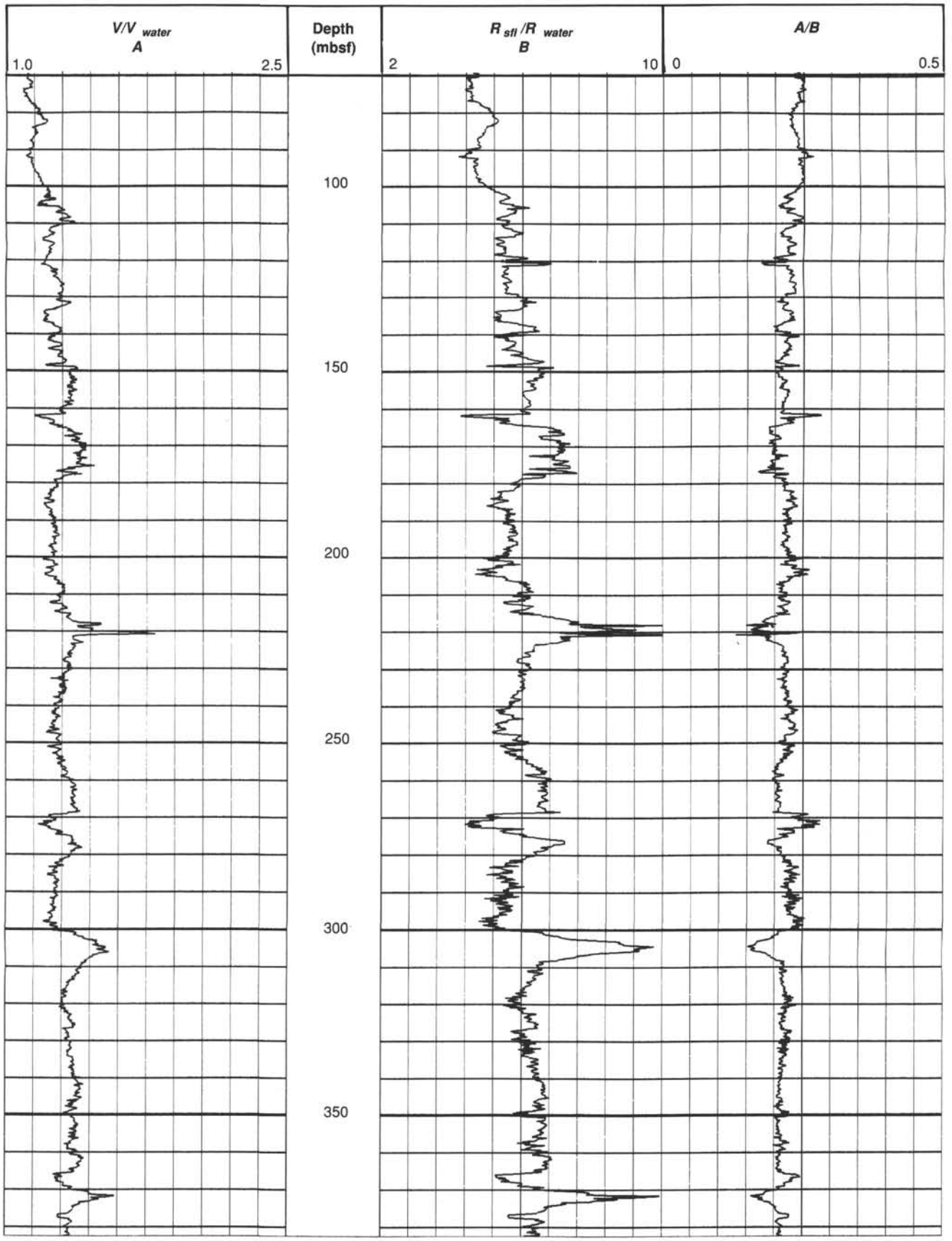

Figure 37. Velocity and resistivity logs for Site 819, plotted as ratios to each other and to water to highlight changes in pore geometry.

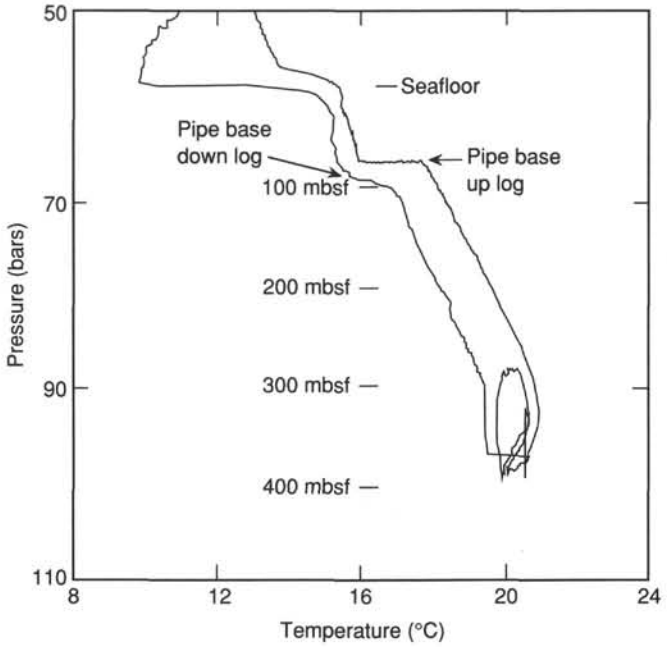

Figure 38. Temperature log as a function of pressure (or depth) for Site 819.

A

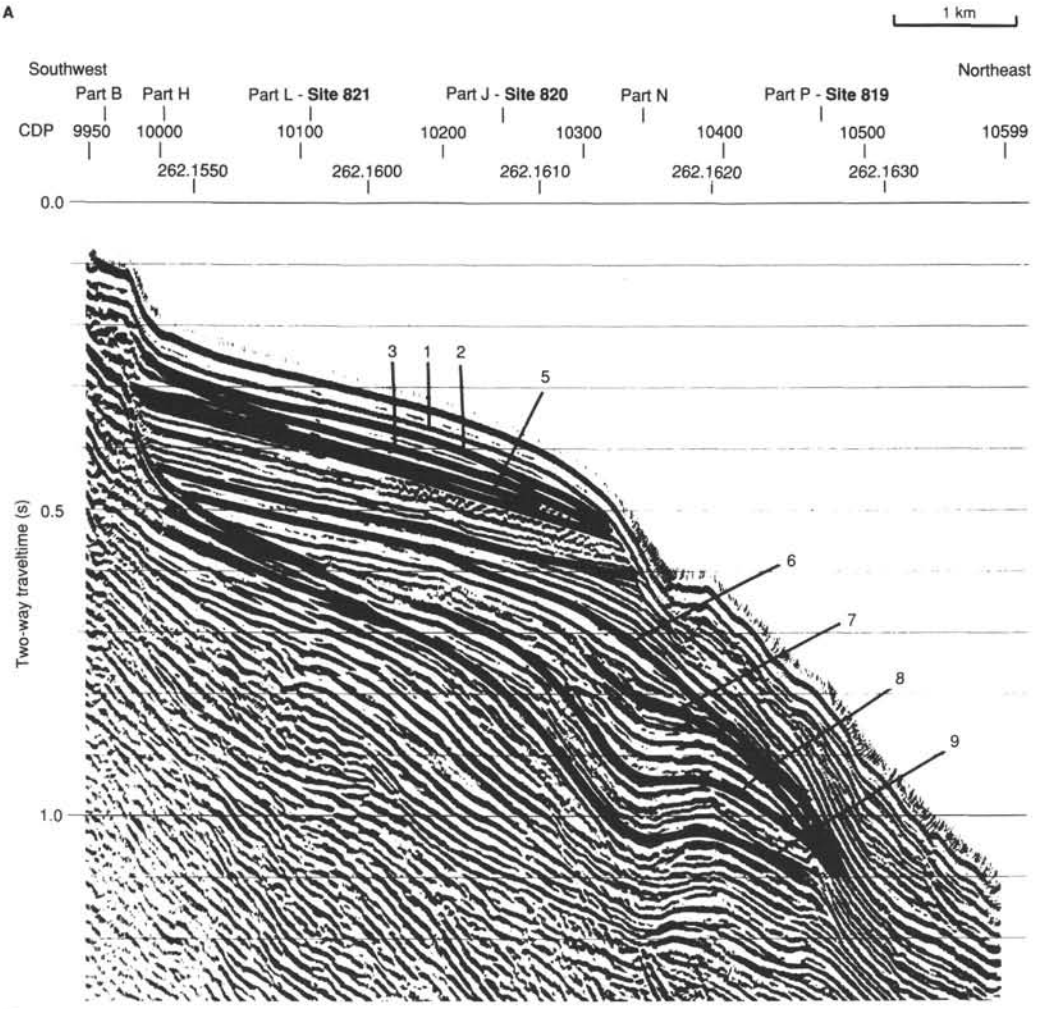

B

Seismic sequence	Age Site 820 Site 821	Time (ms)	Site 821 Lithology	Time (ms)	Site 820 Lithology	Time (ms)	Site 819 Lithology	Age Site 819
1		42		40	Unit IA Cyclical alterations of clays and sandy packstones. More clay rich.			
2	2.65 k.y.	20	Unit I Fining upward cycles of sand to silt to clay. Reef derived sediments seen only in upper part of section.	20				
3	65 k.y.	15		20	Unit IB Cyclical alterations of clays and calcareous sandy packstones. More carbonate rich.		Not present at Site 819	
4		40		30				
5		75		60				2.65 k.y.
6	93 k.y.	65	Units II and III Upward fining cycles.	70	Unit II-Cyclical coarsening upwards muds to bioclastic packstones.	175	Units I, II, and III coarser at base. Clayey ooze predominate.	4.65 k.y.
7	27 k.y.	40	Unit IV Coarsening upward cycles of bioclastic packstones and wackestones.	40	Unit III Coarsening upward cycles of muds to bioclastic packstones.	80	Unit IV Cycles of nannofossil oozes, terrigenous quartz and bioclasts.	1.27 k.y.
8		45		70		100		
9	1.48 k.y.	65	Unit V Cycles of clays and sandy mixed sediments.	115		115	Unit V Nannofossil chalks.	1.48 k.y.

Figure 39. **A.** Interpretation of seismic Line 75/043 to the east of Grafton Passage, showing major seismic sequences. **B.** Lithologic units defined for three sites (819, 820, and 821).

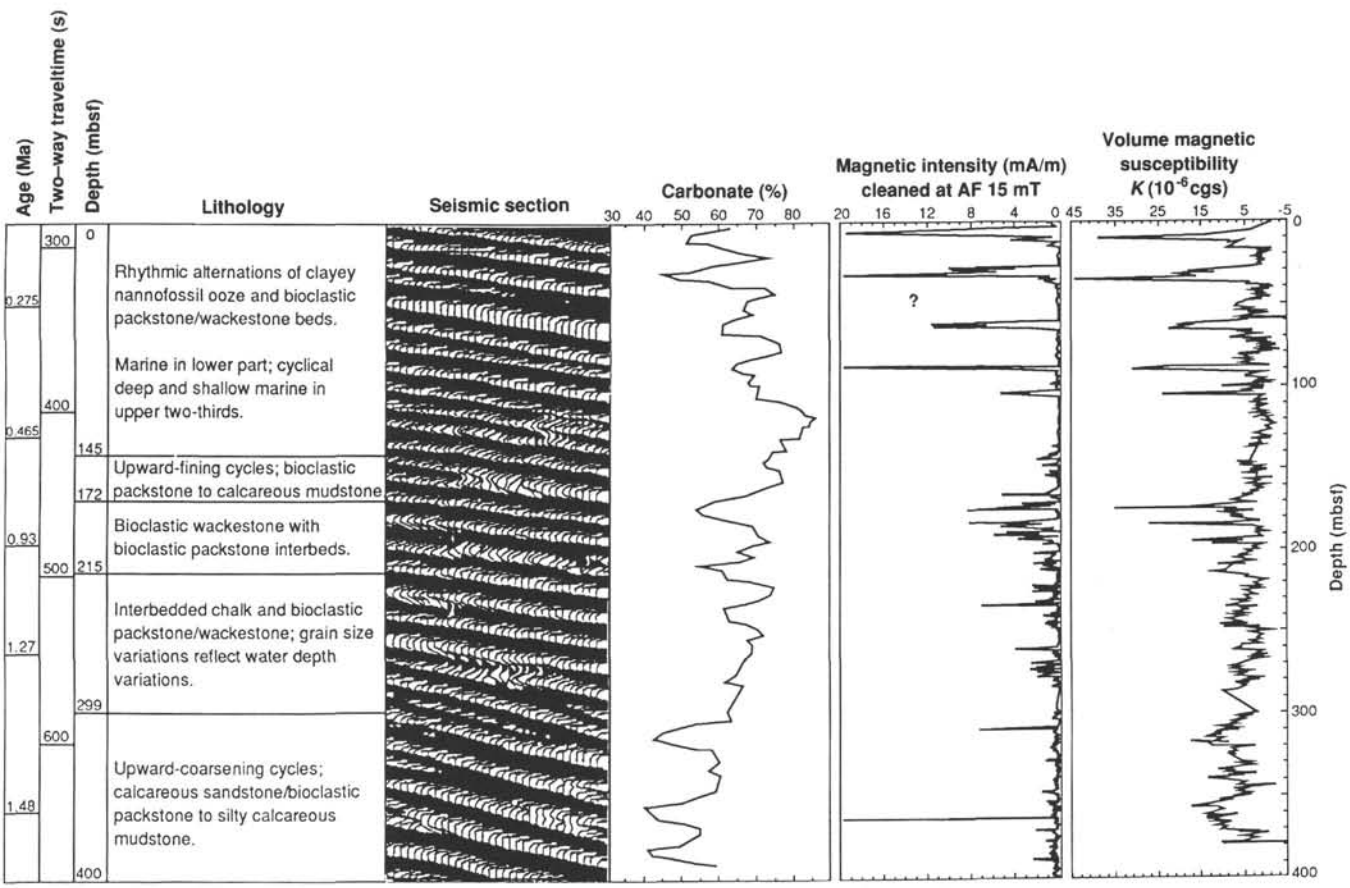

Figure 40. Data from Site 821, located on slope of Great Barrier Reef in 212 m of water.

Hole 819A: Resistivity-Sonic-Natural Gamma Ray Log Summary

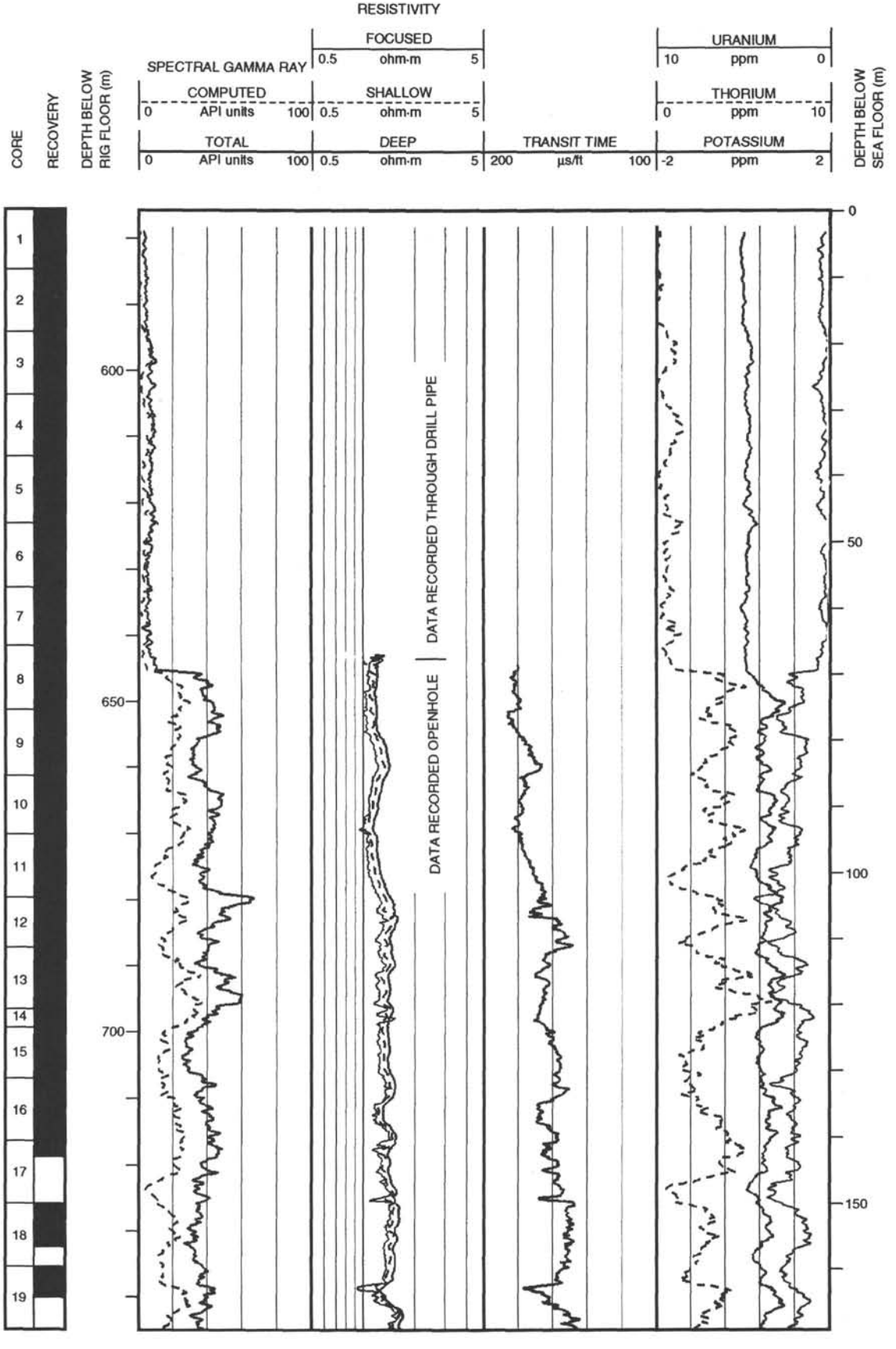

Hole 819A: Resistivity-Sonic-Natural Gamma Ray Log Summary (continued)

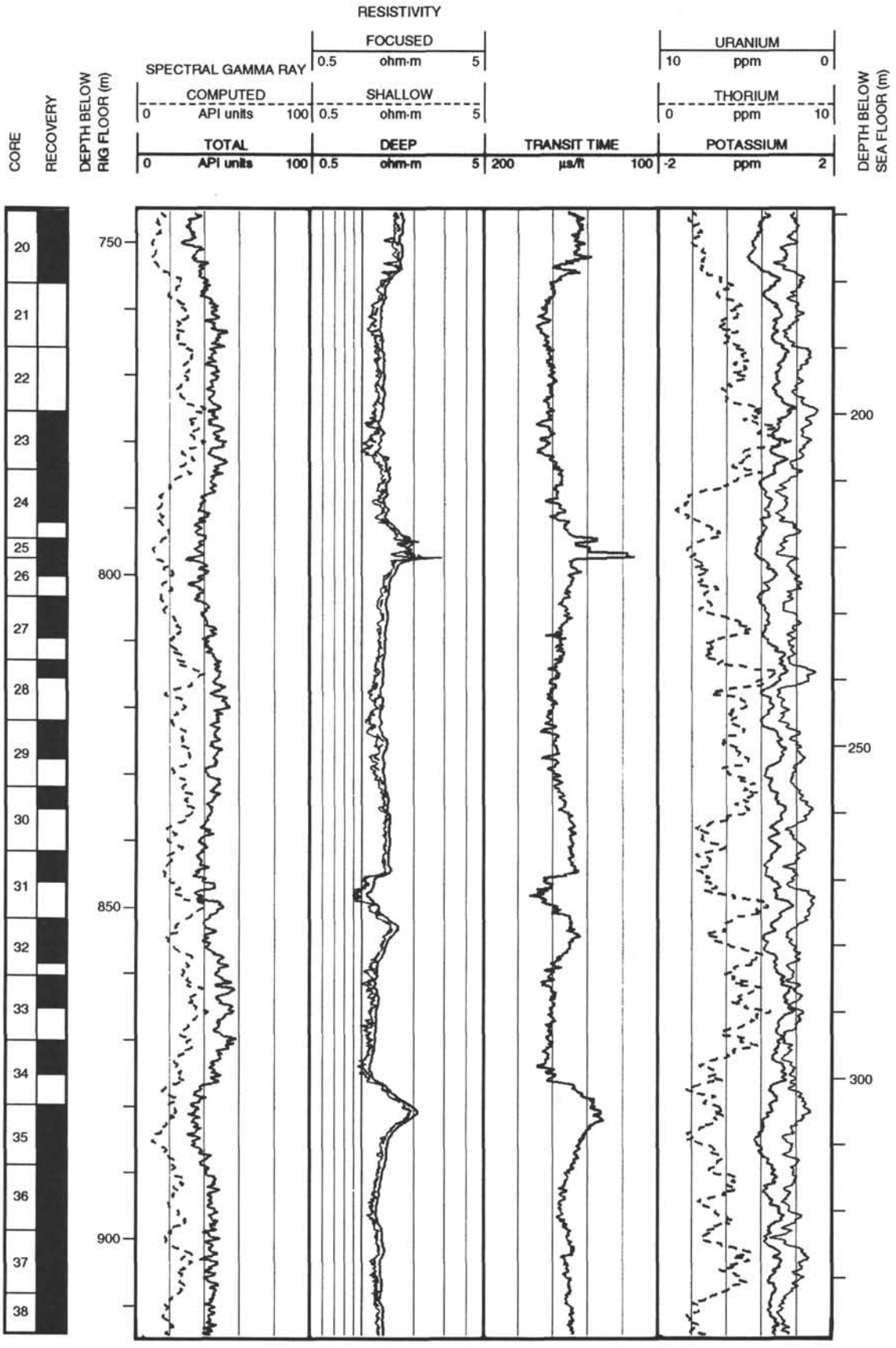

Hole 819A: Resistivity-Sonic-Natural Gamma Ray Log Summary (continued)

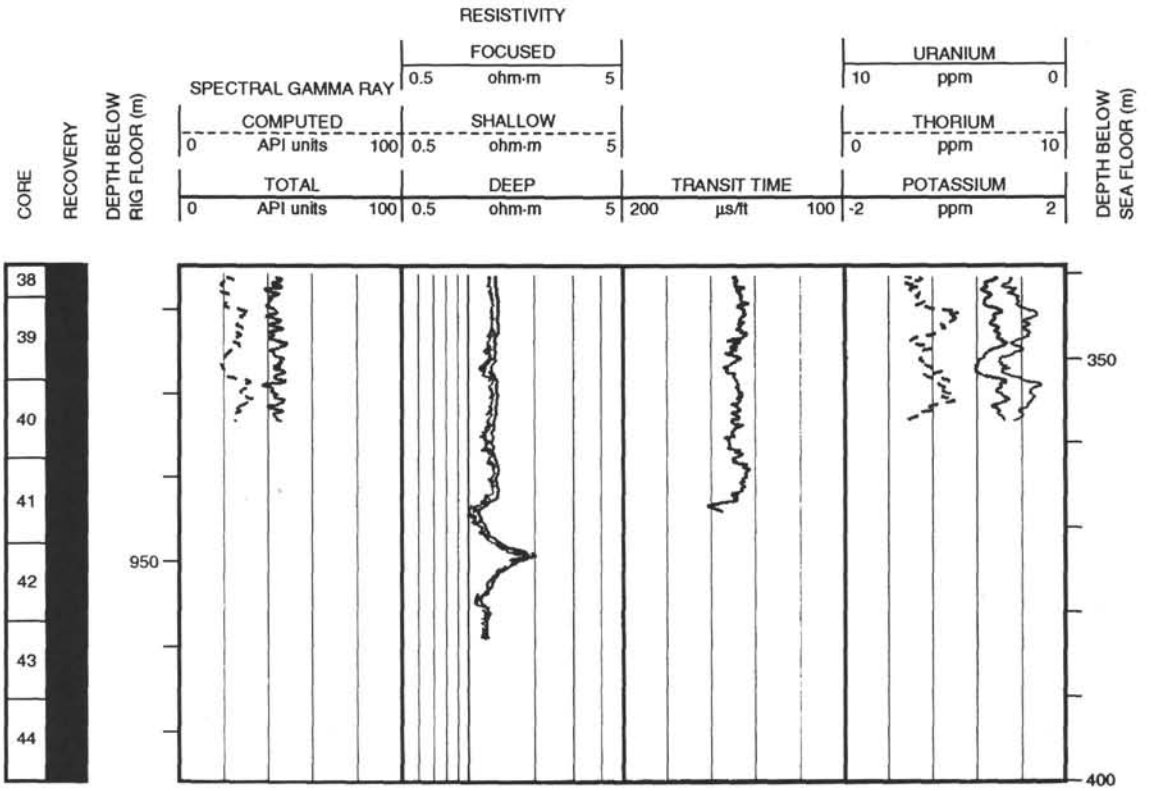

Hole 819A: Density-Natural Gamma Ray Log Summary

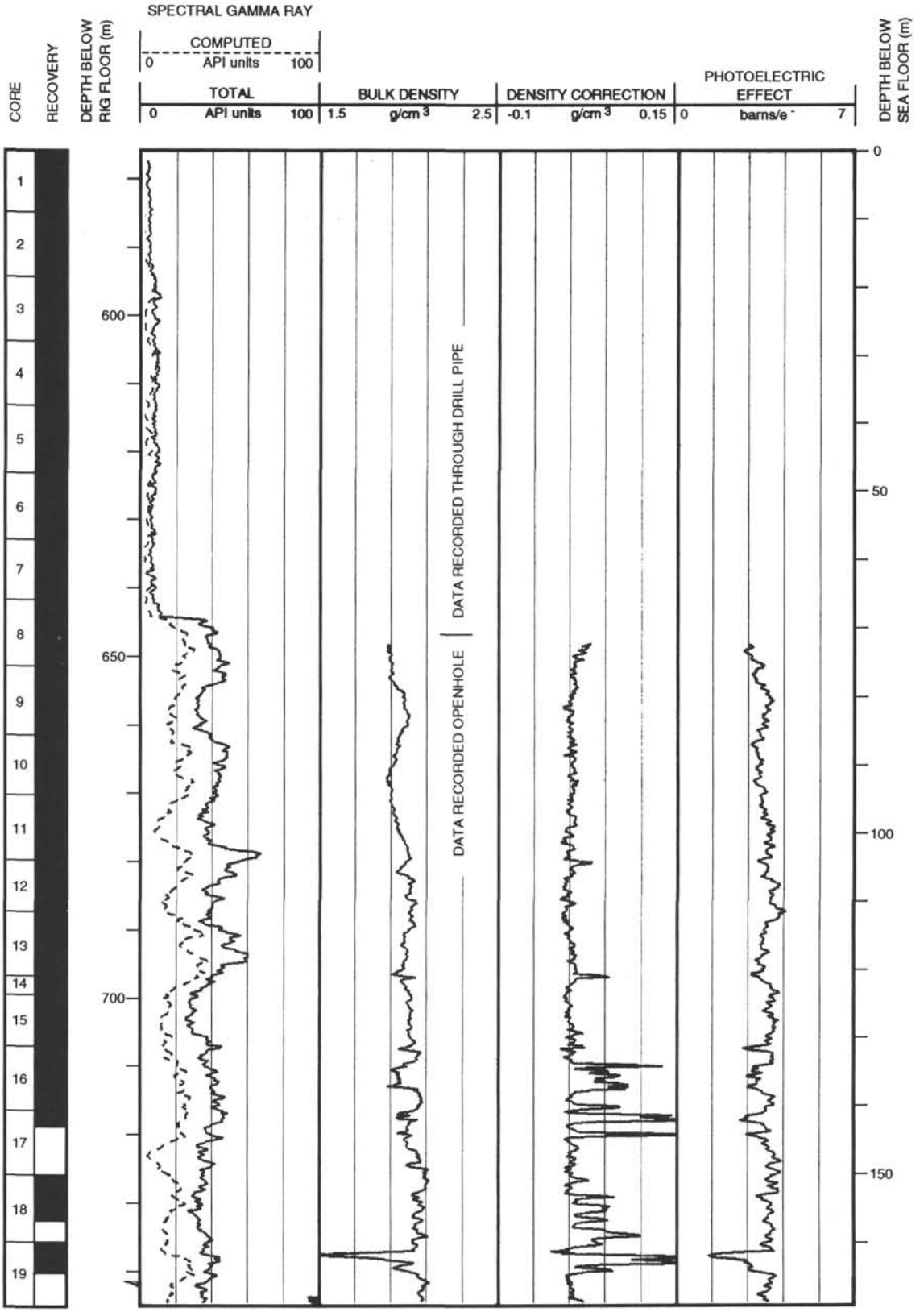

Hole 819A: Density-Natural Gamma Ray Log Summary (continued)

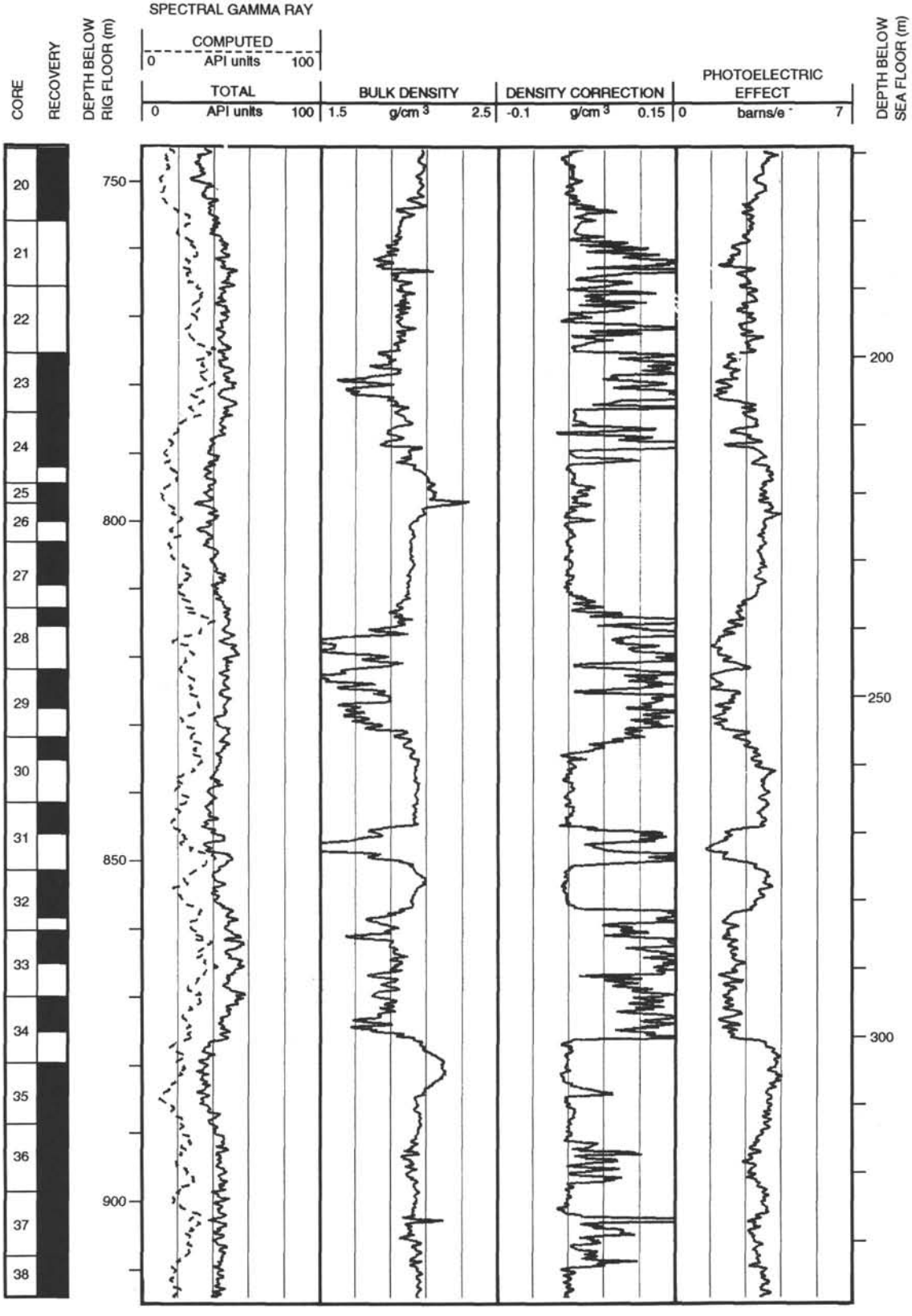

Hole 819A: Density-Natural Gamma Ray Log Summary (continued)